REAL-TIME IMAGE ACQUISITION SYSTEM AT W BAND WITH FREQUENCY SCANNING ARRAY ANTENNA

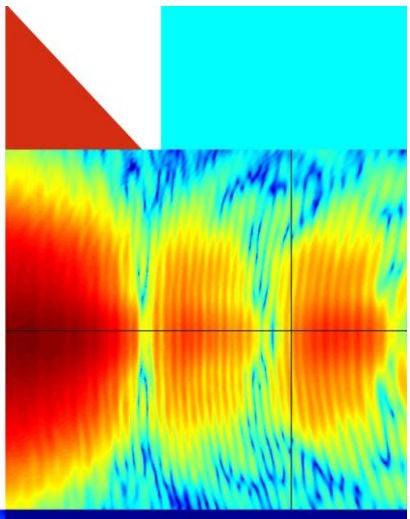

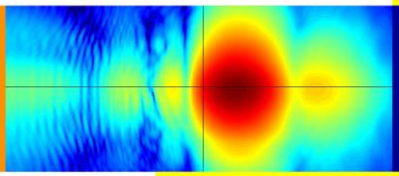

upna
Universidad Pública de Navarra
Nafarroako Unibertsitate Publikoa

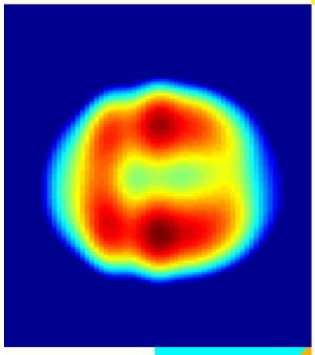

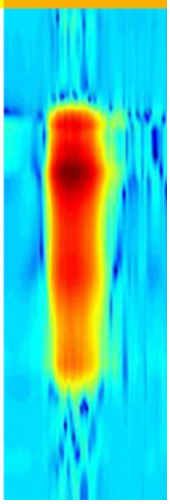

Memoria de la Tesis Doctoral realizada por:

BELÉN LARUMBE GONZALO

Y dirigida por:

DR. JORGE TENIENTE VALLINAS

PARA OPTAR AL GRADO DE DOCTORA EN INGENIERÍA DE TELECOMUNICACIÓN

Universidad Pública de Navarra

DEPARTAMENTO DE INGENIERÍA ELÉCTRICA Y ELECTRÓNICA

Pamplona, Junio 2016

Real-Time Image Acquisition System at W Band with Frequency Scanning Array Antenna

Memoria de la Tesis Doctoral realizada por

Belén Larumbe Gonzalo

Y dirigida por

Dr. Jorge Teniente Vallinas

Para optar al grado de

Doctora en Ingeniería de Telecomunicación

upna Universidad Pública de Navarra
Nafarroako Unibertsitate Publikoa

Universidad Pública de Navarra

Departamento de Ingeniería Eléctrica y Electrónica

Pamplona, Junio 2016

upna Universidad Pública de Navarra Nafarroako Unibertsitate Publikoa

A mi familia

A mis amig@s

A Leia y Asier

AGRADECIMIENTOS

Parece un tópico y la mayoría de personas a las que nos toca escribir unos agradecimientos en una tesis doctoral, decimos que nos ha costado más escribir estos pocos párrafos que lo que es la tesis en sí. Claro que el trabajo de estos cuatro años con su consiguiente escritura para dejar plasmado todo el trabajo realizado no es comparable pero cuando nos dejamos guiar por ecuaciones y leyes físicas, como que la cosa fluye más fácilmente…

Para empezar quisiera agradecer a Jorge mi director de tesis. Has sido un apoyo fundamental durante estos años, un guía, siempre tenías una idea cuando se trataba de arreglar cosas en "plan MacGyver" y siempre has estado disponible para mí. Hemos pasado nervios, deadlines y un montón de anécdotas y en parte gracias a ti esto ha sido posible. Quiero que sepas que no podría haber elegido mejor!

También quisiera agradecer a Ramón. Gracias a ti me inicié en este mundo de las Telecomunicaciones. Esa primera visita a un laboratorio allá por mayo de 2003 cuando andaba un poco perdida sobre que ingeniería estudiar y tu supiste transmitirme esa pasión por lo que haces. Siempre que te he necesitado has sabido sacar un rato de tu apretada agenda para ayudarme.

Que decir de mi querido grupo de antenas. Ha sido como una segunda familia durante este tiempo. Por un lado los "Senior" Iñigo, Juan Carlos, Carlos y Miguel que con vuestras ideas, consejos y distintos puntos de vista tanto me han ayudo. Y los Junior, Ainara,

Itziar, Amagoia, Iñigo, Gonzalo, Inés, Asier y Aitor y las últimas incorporaciones Unai, Torres, Baha, Pacheco, Pablo, Jaime, Carlos, Cebrian, Alicia y Jose. Con esos descansos en los que arreglabamos el mundo, las barbacoas, los congresos y cursos.. y todo el tiempo que hemos pasado juntos contándonos nuestras penas y por supuesto nuestros logros. Muchas gracias chicos por haber estado ahí.

Quisiera agradecer a mis padres y mi hermano el apoyo tan grande que han sido durante todo este tiempo. Sin entender mucho las cosas que les contaba cuando con todo su interés me preguntaban en que estaba trabajando siempre habéis confiado en mí y sois un gran apoyo para mí.

Y por último gracias a Leia y a ti Asier. Mi princesa haces que los días tengan más sentido y me das fuerza para conseguir todo lo que me proponga. Y Asier tú has estado ahí dia a dia soportando mis alegrías y mis penas, me has ayudado a desconectar y a centrarme cuando lo he necesitado. Gracias por quererme tanto y sin ti no sé si lo hubiera logrado.

ABSTRACT

This thesis main objective has been the development of a low cost image acquisition system in terahertz frequencies, focused in food industry applications. In order to do that, first a state-of-the-art analysis of the current technology was made, and the possible approaches to obtain a cost reduction were explored. Frequencial scanning in one of the axis arose as an option to reduce the number of pixels required to obtain the image, avoiding the use of mobile mirror systems which increase the complexity and the cost of the system. Once that this approach was chosen, the basic fundamentals of Leaky-Wave and Phased Array antennas were studied to learn about their properties and the principles necessaries to produce the frequency scanning. Finally, a phased array based on a feeding network with incremental electrical path length differences was chosen to obtain frequency scanning. These electrical path length differences generate different phase values on the elements of the output array, depending on the frequency of operation. Reflectors have been used to manipulate the beam and enhance the resolution of the system, but always using commercially available components to avoid major cost increments. A first prototype working in F band and using a commercial offset TV reflector was capable of acquiring the first images were simple geometries could be recognized. A second prototype was developed, including the enhancement of several aspects that were limiting the image acquisition capabilities of the first prototype, like sidelobe level reduction using windowing techniques and post processing techniques to improve the image

recognition. Finally, the developed prototype antenna was integrated, together with a commercially available mirror, into a conveyor belt simulating a food industry production chain, obtaining real-time image acquisition.

As a proof of concept to analyze the feasibility of using this approach at higher frequencies, a feeding network prototype at 450 GHz has also been designed and simulated, to be fabricated by silicon micromachining using a DRIE (Deep Reactive Ion Etching) process followed by metallization, as a possible high frequency future research line.

RESUMEN

El objetivo principal de esta tesis ha sido el desarrollo de un sistema de adquisición de imagen en terahercios, de bajo coste, y enfocado a aplicaciones para la industria alimentaria. Para ello primero se llevó a cabo un estudio previo de la tecnología existente y de las posibles formas de obtener un abaratamiento del coste. Se pensó que utilizando escaneo frecuencial en uno de los ejes se podría conseguir reducir el número de pixeles necesarios para la toma de la imagen, y evitar el uso de sistemas de espejos móviles que incrementan la complejidad y encarecen el sistema. Una vez que partíamos ya con esta idea, estudiamos los fundamentos básicos de las antenas "Leaky-Wave" y Phased Array para conocer sus propiedades y los principios que producen el escaneo con la frecuencia. Finalmente decidimos conseguir el escaneo con la frecuencia mediante un phased array que utiliza una red de alimentación con caminos de propagación de diferente longitud eléctrica con los que conseguimos que nuestra agrupación de antenas se alimente con fases diferentes en cada elemento unitario, en función de la frecuencia. Se han utilizado espejos para conseguir conformar el haz y mejorar la resolución, pero siempre empleando elementos comerciales, de forma que el coste no se viera incrementado en exceso. Se desarrolló un primer prototipo que trabajaba en la banda F y con la ayuda de un reflector parabólico offset de los usados para captar TV por satélite conseguimos obtener las primeras imágenes con las que éramos capaces de reconocer algunas formas sencillas. También se desarrolló un

segundo prototipo en el que se mejoraron varios aspectos como los lóbulos laterales que en el primer sistema nos degradaban la imagen, por medio de técnicas de enventanado y técnicas de post-procesado para mejorar la calidad de las imágenes registradas. Finalmente, se ha integrado la antena prototipo desarrollada, en una simulación de una cadena de alimentación utilizando un espejo comercial, consiguiendo la adquisición de imagen en tiempo real.

Como prueba de concepto para analizar la viabilidad de utilizar esta técnica a frecuencias más altas, también se ha diseñado y simulado un prototipo de red de alimentación a 450 GHz para su fabricación mediante micromecanizado en silicio por DRIE (Deep Reactive Ion Etching) y posterior metalización, con la idea de futuros desarrollos a alta frecuencia.

CONTENTS

CHAPTER 1

INTRODUCTION

1.1 What are THz?

The Terahertz waves, or just THz, are the electromagnetic waves that lie in the portion of the spectrum between 100 GHz (mm-waves/submm-waves) and 3 THz (far-infrared). Until recent years, this part of the electromagnetic spectrum has remained unexplored because of the technological difficulties related to reach frequencies too high for radio wave technology, and at the same time, too low for photonics.

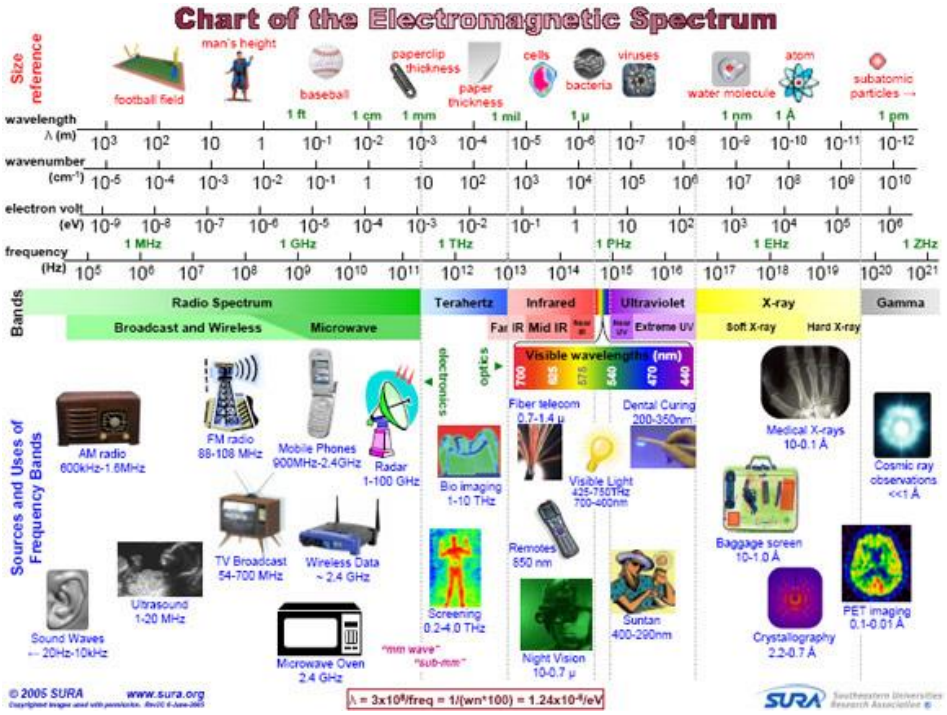

Figure 1.1 – Electromagnetic spectrum with THz region at the middle.

The electromagnetic waves located at that portion of the spectrum have very singular properties that make them very interesting for multiple applications. Because of that, THz technologies have become very popular in the recent years, once that both technologies, radio and photonics, have started narrowing the so called “Terahertz Gap” from both sides. The following are the most interesting properties of the THz waves:

- *THz emissivity of objects*: Due to black body radiation, all the objects radiate some THz power. This allows passive operation in certain applications, not being necessary to illuminate the objects with THz waves.

- *Low attenuation in low visibility conditions*: THz suffer much less attenuation than visible light when propagating through fog, clouds, smoke or sandstorms. This allows the development of THz imaging systems that can offer vision in low visibility conditions.
- *Penetration of light materials*: THz can penetrate light materials like textiles and clothing. This property facilitates the detection of concealed weapons or other threats, hidden under the clothes. It also allows non destructive inspection of the interior of objects.
- *High sensitivity to water presence*: THz suffer from great attenuation in water. However, what could be initially considered as a disadvantage, can be used to detect the presence of water and measure the humidity and water content, with high sensitivity.

The above exposed properties make very interesting the development of THz cameras that, working standalone or combined with visible range or infrared cameras, can have an extremely wide range of applications in sectors like medicine [Jos10, Mue14, Pet13 and Pic06], security and surveillance [Bou14, Coo11 and She11], viticulture [Hor08], aerospace industry [Hwu13, Sho95 and Sue15], pharmacy [Kin13, Sas12 and Wag09], industrial [Bac12, Oka08 and Per14], and food industry [Eta11, Kim12 and Par09].

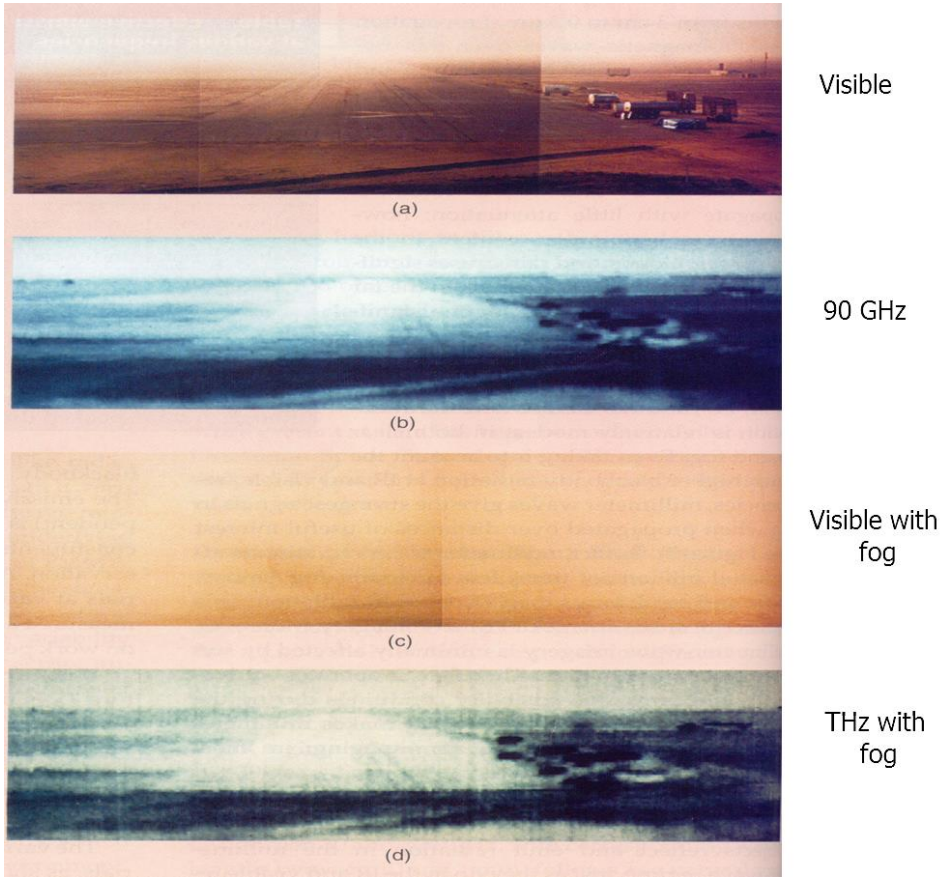

Figure 1.2 – Landing strip images in visible (a) and THz (b) under normal conditions, and under thick fog conditions (c and d).

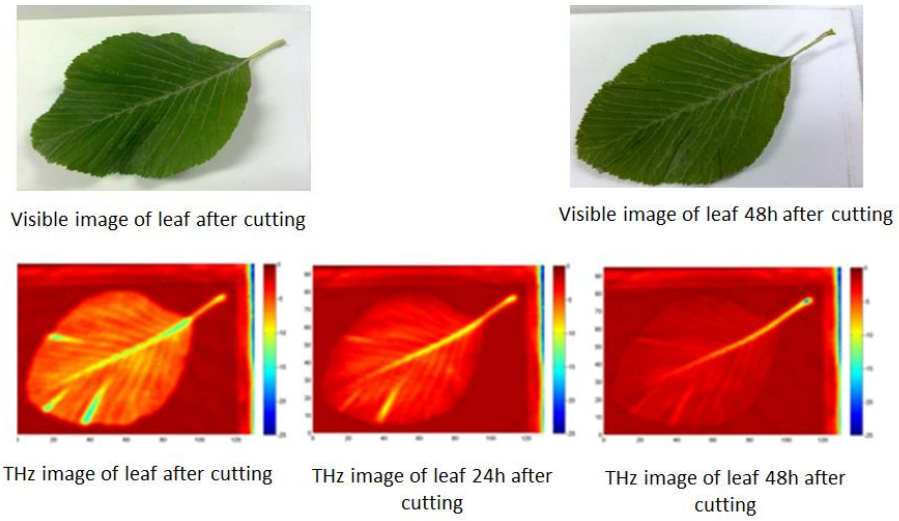

Figure 1.3 – Example of water content analysis of a leaf using THz transmission.

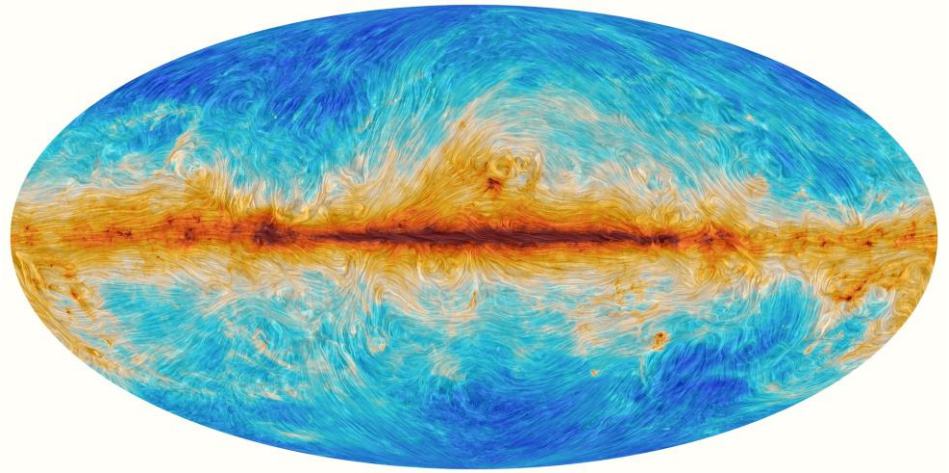

Figure 1.4 – THz image with polarization of the cosmic background radiation of the universe, measured by the Planck mission of the European Space Agency

These THz cameras can have several modes of operation, depending on the particular way of emitting and receiving the THz waves. Depending on the necessity or not of illuminating the targets with THz waves, the cameras can be classified as active or passive. A

passive camera will work receiving the THz emissions of the objects, without illuminating them. On the other hand, an active camera will illuminate the objects with THz waves, and then capture the power reflected by the object, or the power transmitted through the object. Conceptually, these modes of operation would be very similar to the approach used by standard visible light photography. A photography taken with a flash could be interpreted as an active imaging, while another one taken without using the flash would be analogous to passive imaging.

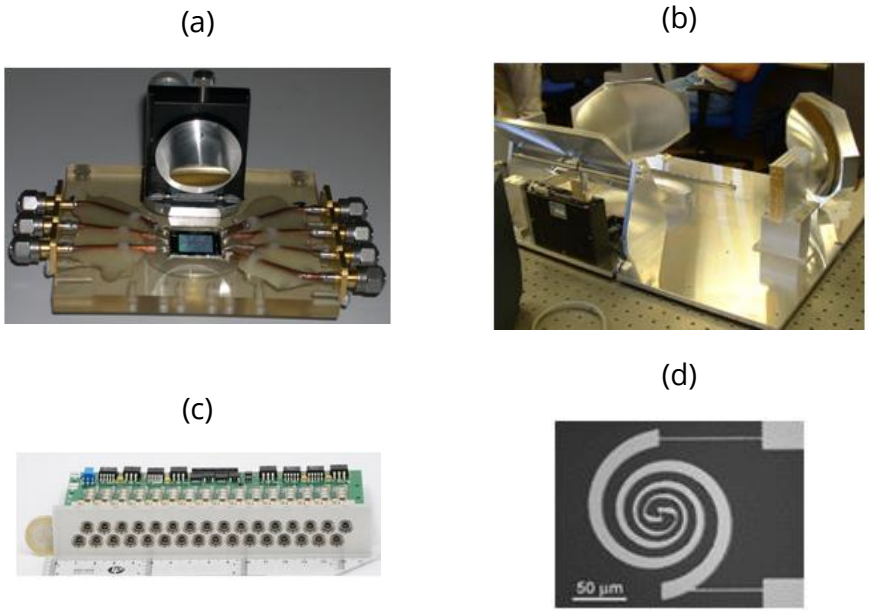

Figure 1.5 –Examples of THz components: (a) 7-pixel camera with focusing mirror, (b) mirror system with mechanical scanning, (c) 32-pixel linear camera, and (d) THz pixel antenna.

It is important also to comment on the safety aspects related to THz technology. Due to their low energy, THz are non-ionizing radiations. It is very straightforward to compare the energy levels of different frequency ranges by using the Planck equation that relates energy with frequency, where h is the Planck constant ($4.13566733 \times 10^{-15}$), and ν is the frequency.

$$E = h * v \quad (1.1)$$

With that equation, it can be easily calculated that X-rays (30 PHz) have an energy of 124 eV (electron volts), red light (400 THz) has an energy of 1.65 eV, and THz (1 THz) have an energy of 0.00414 eV. With a widely accepted ionization limit around 10 eV (13.6 eV is the energy required to ionize and hydrogen atom), it can be seen that frequencies below the ultraviolet range, are not ionizing.

On the other hand, ionization is not the only safety concern. Any electromagnetic wave generates some degree of thermal effects due to the losses introduced by all kinds of matter (as any microwave oven user can corroborate). However, if we take into account that the power levels achievable by active THz systems are in the best scenarios between 0.1% and 1% of the power levels radiated by the typical cellphone, we can conclude that the thermal effects generated by THz waves can be neglected from a safety point of view.

This safety aspects, specially the non-ionization properties, are of great interest in application areas like food safety or non-destructive inspection, where x-ray equipments are the only alternative to THz technologies.

1.2 Motivation of this work.

In the previous section, we have explained the main characteristics of the THz frequency range, and how interesting they are for a very wide range of applications. Unfortunately, THz frequencies lie in the middle of a technological gap that has not started to be covered until recently. In the past years, THz frequencies have been too high for the traditional microwave and

mm-wave electromagnetic technology approach, and at the same time, too low for the optics and photonic technology approach.

Today, this gap is being covered with technological efforts coming from both fields, and, to a great degree, thanks to the very interesting possibilities it brings when applied in security applications. In our current world, where security threats are increasing in a daily basis, both governments and private companies are willing to invest great sums of money and resources in the development of new technologies that can neutralize the aforementioned menaces.

THz related technologies have benefited from that security driven push of the last years, and now, devices that were previously restricted to sci-fi books and movies, like scanners capable of detecting concealed weapons of all kinds under the clothing, are quite real, and commercially available. However, the costs of THz technology are still considerably high, and although that is a factor that arguably is not of the uttermost importance for the security market, it is a key factor in preventing the widespread application of this technology in other sectors and markets.

In the long term future, the technological advances will probably allow cheap mass fabrication of THz components, and applications like THz cameras integrated in cell phones will probably be a reality. However, in the meantime, other cost effective approaches have to be explored in order to increase the level of implantation of THz related technologies. In the particular case of imaging applications, where an array sensor of THz pixels is used to acquire and image, the most straightforward approach to reduce the cost would be to reduce the number of pixels of the sensor. Since a sensor is a 2D array of pixels, increasing or decreasing the size of it, has a quadratic

effect on the number of pixels, and consequently a dramatic effect on the associated cost. If we assume that we cannot reduce the field of view of the camera, then a reduction on the size or number of pixels of the sensor would produce a reduction on the resolution of the resulting image. We can make the assumption of the resolution being already adjusted to the application requirements, so reducing it would not be an option. In that case, the remaining alternative would be to reduce one of the dimensions of the array, and compensate the reduction of the field of view of the camera in that dimension, with some kind of mechanical or electronic sweeping of the sensor. The extreme case of this approach, and at the same time the most usual, would be turning the 2D array sensor into a 1D array sensor, and use mechanical or electronic aiming of the sensor antenna to sweep the field of view in the dimension we have eliminated from the array.

Using a mechanical approach for the sweep movement is usually advantageous in terms of cost, but it also imposes several limitations on the resulting system. These limitations are usually in terms of acquisition time (making this approach unfeasible for certain real-time applications), reduced reliability (not only in the mechanical parts, but also in the electronic components subject to vibrations and accelerations and decelerations), and reduced resolution (due to vibrations and other uncertainties of the sensor antenna aiming).

The electronic sweep seems to be the ideal alternative, not suffering the mechanical sweep limitations. However, if a phased array strategy is used to obtain electronically controlled sweeping, electronic phase shifter components have to be used, increasing the cost and complexity of the system. And that applies only for the lowest frequencies of the THz range, where electronic phase shifter

components are available, since the current state of the art technology of phase shifters is limited to around 200 GHz, with severe insertion losses [Ali13].

A very interesting alternative, and the one this dissertation is focused on, is using frequency scanning antennas to aim the antenna electronically, keeping all the advantages of using electronic sweeping. Moreover, this kind of antenna arrays are usually passive, without the need of active components, eliminating the increased cost and complexity of phased array solutions. In this kind of antenna arrays, the direction of maximum radiation changes with the frequency of the input signal, so it is possible to sweep a certain angular portion of space by feeding the array with a frequency sweep signal. A frequency tuneable signal source is required in this case, but it is a single component independently of the size of the 1D array sensor, so it would still be a scalable solution in terms of cost.

Additionally, it is worth mentioning that there is a particular application case of special interest which is that of THz cameras working on conveyor belt lines. There are multiple widespread applications like quality control, inspection, etc, in multiple industries, where THz technologies could be very useful. In a lot of these cases, the THz camera would have to work on a production line based on a conveyor belt transporting the objects to be imaged. In this particular case, instead of a 2D camera sensor, a 1D camera sensor could be used, since the movement of the conveyor belt can be used to sweep the sensor in the other dimension, without any additional implication or disadvantage compared to a 2D sensor (we would not be adding mechanical complexity to the system, just taking advantage of a mechanical movement already existing). In this particular case, that will be also the object of this dissertation, the 1D

array sensor would be substituted by a single-pixel sensor with frequency sweeping capabilities. A single pixel would be acquiring a 2D image, sweeping one dimension electronically, and the other mechanically.

For all the aforementioned reasons, the main motivation of this work is the development of a single-pixel frequency scanning image acquisition system, capable of acquiring a 2D image at THz frequencies. This will be done with a special focus on reduced cost and complexity, with the goal of obtaining approaches that can help the introduction of THz technologies in widespread industrial applications.

1.3 Technical goals

In the previous section, the main motivation and objectives for the present work have been exposed. As a result of those, the following technical goals have been identified:

- *Successfully design a frequency scanning antenna array*: The main technical goal of the present work is to design an antenna array whose main beam is steerable electronically. The electronic steering has to be controlled by the frequency of the signal that enters the array feeding network, without the need of active components like phase shifters. The amount of angular shift the antenna array can sweep, has to be enough to cover, with the help of a reflector, a substantial portion of a typical conveyor belt width.
- *Obtain an approach valid for a wide range of frequency bands*: We have already shown that there is a very wide range of applications that could potentially benefit from THz

technology. Each application will have its own set of requirements, and because of that, the THz sensor will have to work in the optimal frequency band for each case. For that reason, it is very important that the results of the current work can be applied to a range of frequency ranges as wide as possible, so it can be used by a large number of applications.

- *Prove the feasibility of the selected approach*: The designed frequency scanning antenna array has to prove that is feasible to fabricate, and that it performs as expected, and has no major drawbacks or unexpected disadvantages that could prevent its applicability in a real environment.
- *Design, fabricate and test a proof-of-concept validation prototype*: In order to prove that the developed approach can be used in a real application, a proof-of-concept prototype is necessary. In this work, the prototype will try to replicate a conveyor belt production line with a 1D THz imaging sensor made with a single pixel and a frequency scanning system.
- *Keep the focus on low cost and low complexity solutions*: This goal has to be very present at all the levels and stages of the current work. Each time a design or fabrication choice has to be made, its influence in the cost and complexity of the system must be one of the most important criteria to be taken into account. This goal is key in the present work, since cost and complexity are the main limitation factors of the diffusion of THz technologies in industrial applications.

1.4 Dissertation structure

The current dissertation is structured according to the following chapter structure. This structure doesn't always follow the exact chronological order in which the different parts of the work were developed, but it has been considered that the current order brings more clarity and understanding of the performed work, to the reader.

- *Chapter 1 – Introduction*: In the present chapter, a brief introduction of THz technologies, and the main motivations and objectives of the current work, are presented to the reader. The dissertation structure and a description of potential applications of the work are also explained in this chapter.
- *Chapter 2 – Initial Work*: The first technologies and ideas that were selected and analyzed, and a summary of all the previous research work that was performed before deciding on the definitive approach, are presented in this chapter.
- *Chapter 3 – Frequency Scanning Antenna Array at F-Band, Design and Results*: All the work related to the first frequency scanning array that was developed at F-Band, is presented in this chapter. This includes all the design process, the fabrication and assembly of the first array prototype, and the measurement results obtained, as well as the results of a simple proof of concept experimental setup, using a commercial TV parabolic dish.
- *Chapter 4 – Frequency Scanning Antenna Array at W-Band, Design and Results*: After analyzing the results obtained from the first

FSA array prototype, a second prototype was developed at W-Band. This chapter includes the justification and differences of this second prototype with regards to the first one, and the design, fabrication and measurement processes, together with the obtained results. A complete proof of concept prototype of a real time THz imaging system in a conveyor belt application was developed. The raw results obtained, and the post processing techniques applied to them are presented in this chapter.

- *Chapter 5 – DRIE FSA Array at WR2.2 Band, Design and Fabrication Considerations*: In order to demonstrate the feasibility of applying the FSA array approach in applications requiring working at higher frequencies, an array working at 440 GHz was designed. DRIE fabrication techniques that would allow cheap mass fabrication of such array were considered. All the related data and results are presented in this chapter.
- *Chapter 6 – Conclusions and Guidelines for Future Research*: The conclusions that have been obtained from the current work, are presented in this chapter. Additionally, future lines of research that could derive from this work, aspects that could be analyzed more deeply and other matters of interest for future works, are explained too.
- *Chapter 7 – List of Publications*: The complete list of publications derived directly or indirectly from the work presented in this dissertation, are listed in this final chapter.

1.5 Potential applications

As it was briefly explained at the beginning of this chapter, there is a great amount of applications that could benefit from the particular characteristics of THz frequencies. In particular, the present work aims to be useful for applications in the field of THz image acquisition systems.

Traditionally, this kind of imaging systems have limited their implantation mainly to threat detection scanners used for security applications like border control, in environments like airports or other critical infrastructures. However, there are multiple other sectors that could benefit from THz imaging systems, like industrial production lines, should the costs of such systems were substantially lower. In particular, we have chosen foreign object detection through THz imaging for food safety improvement, in the context of food industry, as the target application for a low cost THz image acquisition system.

It is important to highlight the importance of the food industry weight in the global economy. The food industry sector reports huge revenues, with an exponential increase related to the global population growth, especially in regions like Asia, Africa, and Middle East.

Traditionally, the level of high technology implantation is relatively low in the food industry sector. This, in practice, means a low level of competence when introducing new technologies like THz sensors. Moreover, this low level of technological implantation is often not caused by lack of interest from the industry on incorporating new technologies. Currently, there is a high demand in the sector for technological improvements capable of solving the challenges the

food industry faces nowadays, and an internal perception of this demand not being adequately covered.

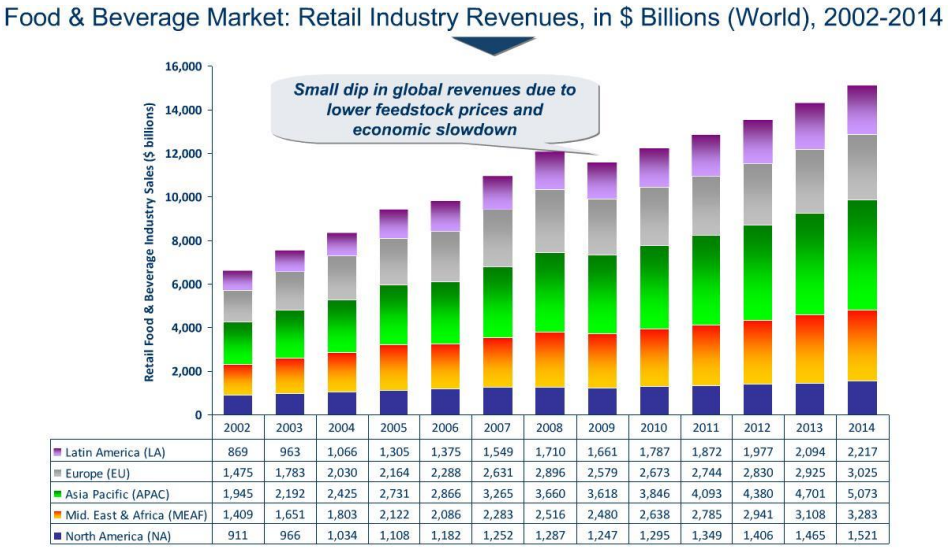

	2002	2003	2004	2005	2006	2007	2008	2009	2010	2011	2012	2013	2014
Latin America (LA)	869	963	1,066	1,305	1,375	1,549	1,710	1,661	1,787	1,872	1,977	2,094	2,217
Europe (EU)	1,475	1,783	2,030	2,164	2,288	2,631	2,896	2,579	2,673	2,744	2,830	2,925	3,025
Asia Pacific (APAC)	1,945	2,192	2,425	2,731	2,866	3,265	3,660	3,618	3,846	4,093	4,380	4,701	5,073
Mid. East & Africa (MEAF)	1,409	1,651	1,803	2,122	2,086	2,283	2,516	2,480	2,638	2,785	2,941	3,108	3,283
North America (NA)	911	966	1,034	1,108	1,182	1,252	1,287	1,247	1,295	1,349	1,406	1,465	1,521

Figure 1.6 – Evolution of food industry sector global revenues

One of the main challenges the food industry faces is the control and detection of foreign bodies in the production line. Detection of foreign bodies capable of harming the consumer or causing a noticeable effect on the product quality is of special importance, since related incidents can cause severe harm to a brand reputation, even in the cases where the consumer health is not at risk.

The foreign bodies can have multiple sources, as they can be originated by the machinery, the human operators, the packing, or even by pests. Because of this, it's hard to find a common detection strategy, and currently foreign bodies are usually classified by whether they can be detected by a metal detector or not. At the present time, there are no reliable methods of detecting non-metallic foreign bodies in food products, and for that reason, the main efforts of the industry are towards preventive measures like using non

easily breakable specific tools, inventorying and controlling all the glass surfaces and components, and adding metallic components to all non-metallic objects (like for example band-aids), in order to make them easily detectable by a magnetic trap, should they accidentally end up in the finished product. Depending on the specifics of each productive process, this preventive strategy can be very costly to the companies, especially if a high rate of false positives is obtained, generating non necessary product rejections.

From the detection approach, two main options are commercially available at this time. On one side, the metallic foreign bodies can be detected by metallic detectors. Current metal detection technology is able to detect even non-magnetic materials like stainless steel, and non-ferrous materials like aluminum. However, there are some limitations on the smallest detectable size, and objects measuring less than 2 mm, are usually undetectable.

On the other side, non-metallic objects can be detected by X-Ray imaging systems. They are especially effective when the density of the foreign body is higher than that of the surrounding product, but are limited for detecting certain metals like aluminum, or lower density materials like plastic, paper or insects. Additionally, since X-Rays are an ionizing radiation, the sensitivity of X-Ray imaging systems for food industry applications is very limited by the power restrictions imposed by the strong regulations in place.

Because of the above explained limitations, there is currently a high demand for effective and reliable foreign body detection systems, capable of offering the ever increasing safety levels demanded by the customers and the regulatory authorities. A detection system working at THz frequencies could be the answer to this demand, if the cost and complexity of these systems can be

reduced, to meet the requirements of the food industry in that aspect. We hope that the results of this work will serve towards achieving that objective.

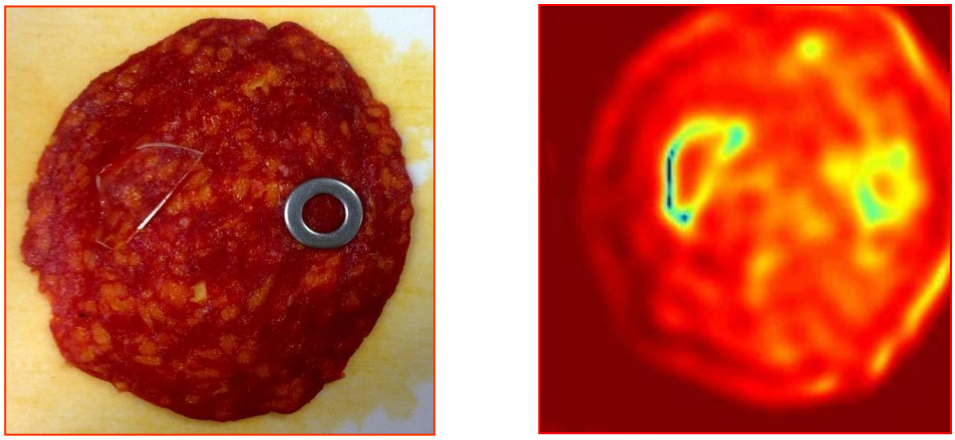

Figure 1.7 – Food product with piece of glass and metallic washer in visible and THz images.

1.6 References

[Ali13] N. Alijabbari, R. M. Weikle II and C. L. Brown, "*A 200 GHz GaAs Schottky-Diode Phase Shifter Integrated on a Silicon-on-Insulator Substrate*", IEEE MTT-S International Microwave Symposium Digest, June 2013.

[Bac12] E.Baccaglini, M.Gavelli, N.Raimondo, R.Scopigno, F.Palma, "*Terafly: A THz image-processing-based architecture for semi-automatic industrial inspection and measurement*", 37th International Conference on Infrared, Millimeter, and Terahertz Waves (IRMMW-THz), September 2012.

[Bou14] J. Bou Sleiman, J. El Haddad, J. B. Perraud, L. Bassel, B. Bousquet, N. Palka and P. Mounaix, *"Qualitative and quantitative analysis of explosives by terahertz timedomain spectroscopy: application*

to imaging", 39th International Conference onInfrared, Millimeter and Terahertz Waves (IRMMW-THz), September 2014.

[Coo11] K. B. Cooper, R. J. Dengler, N. Llombart, B. Thomas, G. Chattopadhyay and P. H. Siegel, *"THz Imaging Radar for Standoff Personnel Screening"*, IEEE Transactions on Terahertz Science and Technology, Vol. 1, No. 1, September 2011.

[Eta11] D. Etayo, J. C. Iriarte, I. Palacios, I. Maestrojuán J. Teniente, I. Ederra, R. Gonzalo , *"THz Imaging System for Industrial Quality Control"*, IEEE MTT-S International Microwave Workshop Series on Millimeter Wave Integration Technologies, 2011.

[Hor08] Y. L. Hor, J. F. Federici and R. L. Wample, *"Non-destructive evaluation of cork enclosures using terahertz/ millimeter wave spectroscopy and imaging"*, Appl. Optics 47, 72-78, January 2008

[Hwul13] S. U. Hwu1, K. B. deSilva and C. T. Jih, *"Terahertz (THz) wireless systems for space applications"*, IEEE Sensors Applications Symposium (SAS), 2013.

[Jos10] C. S. Joseph, A. N. Yaroslavsky, L. Lagraves, T. M. Goyette and R. H. Giles, *"Dual Frequency Continuous Wave Terahertz Transmission Imaging of Nonmelanoma Skin Cancer"*, Proc SPIE 7601, Terahertz Technology and Applications III, 760104, March 2010.

[Kim12] [9] G. Kim, S. D. Lee, J. H. Moon, K. B. Kim and D. K. Lee, *"Terahertz Technology for the Detection of Food Contaminants"*, 37th Conference on IRMMW-THz, September 2012.

[Kin13] E. E. Kinga, M. Sullivana, E. Katoa and D. Heapsa, *"Pharmaceutical, Biological and Industrial Applications ofTerahert Spectroscopy and Imaging for IRMMW -THz 2013",* 38th International Conference on Infrared, Millimeter, and Terahertz Waves (IRMMW-THz), Sept. 2013.

[Mue14] M. Mueller-Holtz, H. Seker and G. Smith, *"Wavelet denoising and reconstruction of a microneedle embedded in human skin ex-vivo using terahertz pulsed reflectance"*, Engineering in Medicine and Biology Society (EMBC), 36th Annual International Conference of the IEEE, August 2014.

[Oka08] S. Oka, H. Togo, N. Kukutsu and T. Nagatsuma, *"Latest Trends in Millimeter-wave Imaging Technology"*, PIERS Proceedings, March 2008.

[Par09] P. Parasogloua, E.P.J Parrotta,b, J.A. Zeitlera, J. Rasburnc, H. Powellc, L.F. Gladdena, M.L. Johnsa, *"Quantitative Moisture Content Detection in Food Wafers"*, 34th International Conference on Infrared, Millimeter, and Terahertz Waves, 2009. IRMMW-THz 2009.

[Per14] M. F. Pereira, *"THz and Mid Infrared (TERA-MIR) Semiconductor Materials: From Microscopic Theory to Industrial Applications"*, 16th International Conference on Transparent Optical Networks (ICTON), Jul. 2014.

[Pet13] B. St. Peter, S. Yngvesson, P. Siqueira, P. Kelly, A. Stephen Glick, and A. Karellas, *"Development and Testing of a Single Frequency Terahertz Imaging System for Breast Cancer Detection"*, IEEE Journal of Biomedical and Health Informatics, Vol. 17, No.4, July 2013.

[Pic06] E. Pickwell and V. P. Wallace, *"Biomedical applications of terahertz technology"*, J. Phys. D: Appl. Phys. 39 R301-R310, 2006.

[Sas12] [21]T. Sasakia , K. Itatanib , T. Sakamotoc , J. Nishizawad, *"Nondestructive sample preparation of pharmaceutical samples for wide frequency range THz spectroscopy"*, 37th International Conference on Infrared, Millimeter, and Terahertz Waves (IRMMW-THz), Sept. 2012.

[She11] D. M. Sheen, D. L. McMakin and T. E. Hall, *"Active Millimeter-Wave and Sub-Millimeter-Wave Imaging for Security Applications"*, IRMMW-THz, October 2011.

[Sho95] M. Shoucri, R. Davidheiser, B. Hauss, P. Lee, M. Mussetto, S. Young and L. Yujiri, *"A passive Millimeter Wave Camera for Aircraft Landing in Low Visibility Conditions"*, IEEE AES Systems Magazine, May 1995.

[Sue15] J. Y. Suen, Member, IEEE, M. T. Fang, S. P. Denny, and P. M. Lubin , *"Modeling of Terabit Geostationary Terahertz Satellite Links From Globally Dry Locations"*, IEEE Transactions on Terahertz Science and Technology, Vol. 5, No. 2, March 2015.

[Wag09] M. P. Wagh, Y.H. Sonawane and O. U. Joshi, *"Terahertz Technology: A Boon to Tablet Analysis"*, Indian J. Pharm. Sci., 71(3), 235-241, May-June 2009.

CHAPTER 2

INITIAL WORK

2.1 Single-pixel and Multiple-pixel THz imaging systems

As it was introduced in the previous chapter, there are an increasing number of applications that can take advantage from the capabilities of the THz based technologies. Popular application fields where active research on THz is being currently done are medicine (skin cancer detection, caries detection,...[Kaw13 and Jos10]), security and surveillance (detection of hidden weapons or explosives,

detection of gases,...[She11 and Coo11]), viticulture (control of the vine state [Hor08]), food sector [Kim12], space and aeronautics [Sho95], industrial [Ame13 and Oka08], passive tomography imaging [Yin07] and investigation on proteomics in the pharmaceutical industry [Wag09].

The main advantages of this technology rely on the particular properties of THz waves, especially on their penetration in dielectric material, and on their high sensitivity to humidity and water content. These properties allow non-destructive evaluation in single layered and multi-layered structures in industry in order to detect abnormalities or strange bodies. Furthermore, different material properties such as density or humidity can be analyzed, and materials can be characterized and even sometimes identified.

On the other hand, the disadvantages are related to the development of devices and sub-systems operating at mm-wave frequencies. High sensitive devices with smaller dimensions, low noise amplifiers and mixer are demanded for these applications. Moreover, new materials capable of working at these frequencies are also required. In the recent years, new technologies such as GaAs, SiGe, GaN, and new fabrication techniques [Hen09 and Sen09] have been developed, making the millimeter and sub-millimeter frequency bands more accessible to new applications.

When developing THz image acquisition systems, there are two strategies that represent the two extremes in an existing compromise between cost, and complexity. One of them is developing a sensor matrix with as many THz sensors as the desired number of pixels in the final image. This is a very simple approach that doesn't require complex focusing structures with moving parts, and has the advantage of obtaining very fast acquisition times, and

with very good reliability. Of course, cost is the main drawback of this strategy; since THz sensors will be the cost dominating components until the technology reaches a mature enough state where cheap mass production techniques are applied to the sensors fabrication. In [Lee05 and Yuj03] we can see two examples of these multiple pixel THz image acquisitions systems.

Figure 2.1 - 1040 pixel THz camera working at 89 GHz, with dielectric lens.

On the other hand, the alternative strategy consists in using a single pixel, and use some kind of scanning system, to sweep the full target image plane. In [Coo10] we can see an example of a single-pixel system that uses a mirror system to acquire a full image.

In this case, the cost is much lower than when comparing with multiple pixel systems, but the acquisition times increase due to the fact that the sensors have to make multiple acquisitions to get the full image, making these systems impractical for real-time applications when a high number of pixels is required on the final image. Moreover, the scanning systems usually require complex and precise mechanical systems to properly align the focusing mirrors in

a fast enough way, making the long term reliability of the system an important factor to take into account.

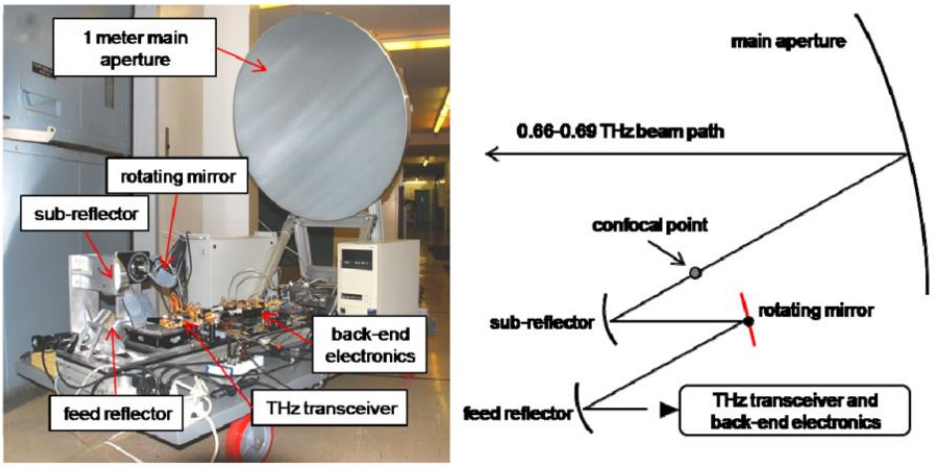

Figure 2.2 - Single pixel camera with scanning mirror system at 670 GHz.

Falling somewhere in the middle between the above described extremes, fall the multipixel systems that use more than a single pixel to acquire the image, but not the full amount of pixels of the full output image. The most typical examples are 1D pixel arrays that sweep the image plane in the other dimension to get the final 2D image result. In [Coo11, Fri11, Gro09 and App99] several examples of these intermediate systems can be found.

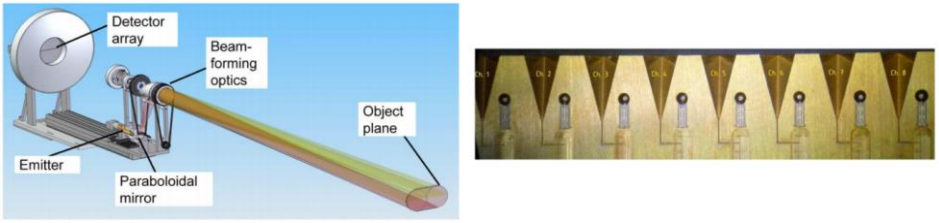

Figure 2.3 - 8 pixel array camera with mechanical scanning system.

In these cases, the compromise between cost and fast acquisition times and the application requirements, drive the number of sensors used by the system, and the complexity of the scanning mechanisms.

2.2 THz systems in food industry

As it was discussed in the previous chapter, there is a great interest in the food industry for technologies capable of detecting small foreign objects in the food products, at several points of the production process. Moreover, the current perception coming from the industry is that the commercially available technological products are not covering adequately the existing demand.

There are currently some commercial products for the detection of foreign bodies in food products, which are based on radiofrequency technologies. The best example is the product developed by Food Radar Systems AB from Sweden, which uses the variations of electrical permittivity of the foreign bodies, to detect them. The food product, which has to be of liquid or semi-liquid nature, flows through a metallic pipe with a section where a low frequency electromagnetic field is generating a resonance. When a foreign body crosses that section, its different electrical permittivity alters the electromagnetic properties of the cavity, changing the resonance frequency. This change can be measured and detected, triggering an alert that activates a valve mechanism that rejects the contaminated section of the food product.

This system works at lower frequencies and uses a different principle than the one used in the current work. It also requires the product to be liquid, and to have some degree of homogeneity to detect the contrast, since no imaging is done, and no image processing techniques can be used. Anyway, it is a good example of the growing interest of applying radiofrequency technologies in the food industry.

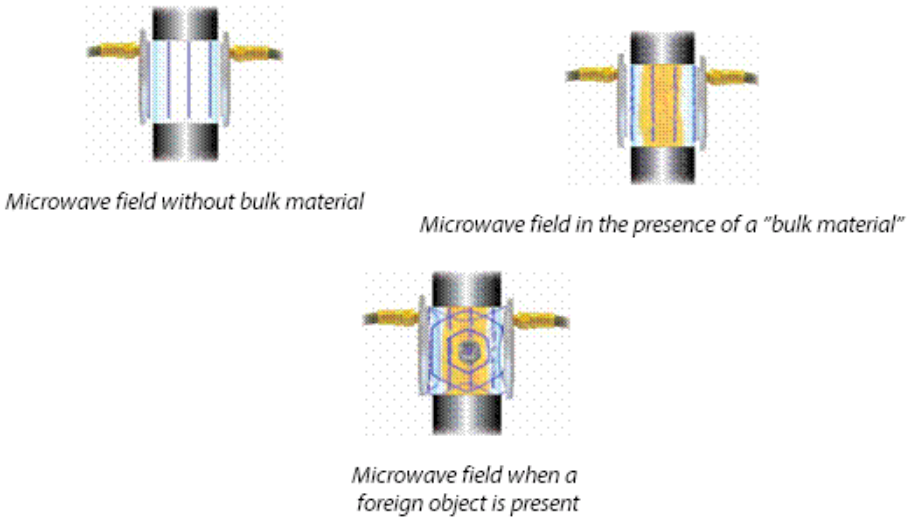

Figure 2.4 - Principle of operation used by Food Radar Systems AB.

No examples of commercially available single-pixel or multi-pixel THz imaging systems for food industry applications where found at the moment of writing this dissertation, so we hope that the current work can be a useful contribution to the future development of such systems.

Figure 2.5 - Food Radar Systems AB prototype system

2.3 Frequency scanning antennas.

As a first step for choosing a design for the frequency scanning antenna, that fulfils all the technical requirements presented in the previous chapter, the main approaches to the problem were explored. The two most prominent technologies used for frequency scanning will be presented in the following sections, Leaky Wave Antennas, and Phased Arrays.

2.3.1 Leaky Wave Antennas

Leaky Wave Antennas, or LWA's, are part of the group of antennas that use the principle of "traveling waves" as a mechanism of

radiation, since the former is originated by wave propagating through a waveguide. These antennas consist in structures in which power is coupled from a guided mode to free space, in a continuous or discrete way, among the longitude of the guiding structure. It can be considered that the guided mode “leaks” power to free space, hence giving the name to this family of antennas. In LWA’s the angle of leakage is frequency dependant and hence the radiation pattern main beam direction.

The most basic example of a LWA would be a rectangular metallic waveguide with a slit among all the longitude of one of its sides, as it can be seen in Figure 2.6 - . This slit allows a power leakage from the propagating mode to free space among all the longitude of the waveguide.

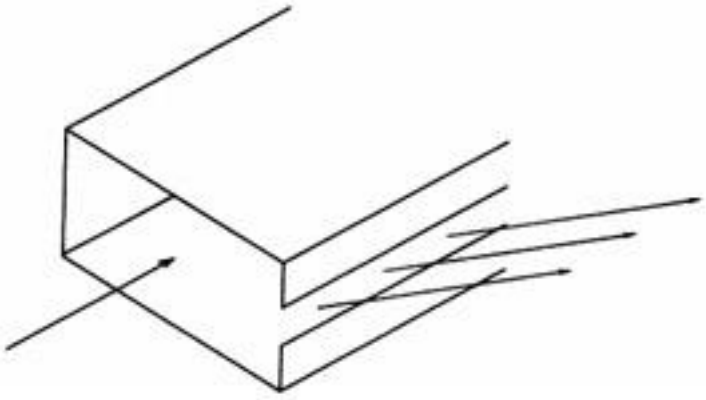

Figure 2.6 - Example of WLA structure.

Using this principle, this kind of antennas have been subject of research for more than 50 years, with a very wide range of guiding structures and other geometrical parameters like slit locations and shapes having been analyzed, to obtain the desired radiation diagrams shapes.

The first LWA was researched by Hansen in the 40's, in a patent named "Radiating Electromagnetic Waveguide" [Han46], that presented the structure of Figure 2.7 - .

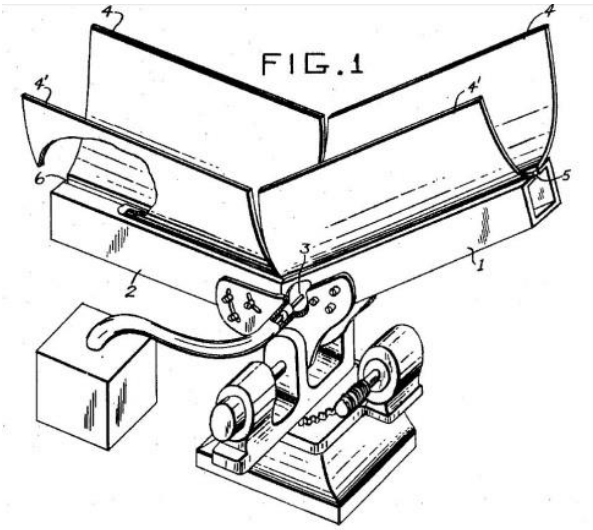

Figure 2.7 - Waveguide structure presented by Hansen.

This LWA is composed by two sections of rectangular waveguide, with a longitudinal slit, similar to the previous example. The main difference is that, for enhancing the adaptation of the leaky wave to the free space, and for narrowing the shape of the radiation pattern in the axis perpendicular to the guide, a longitudinal horn section was added to the slit output.

From the 50's to the 70's, there was a lot of research in this topic, focused in the theoretical aspects. One of the main aspects studied was the role the leaky modes played in the radiation of the antenna [Tam63, Tam67, Oli07, Fel73, Hes61, Hes69 and Mit84]. Other aspects were the search for LWA's based on metallic structures

[Oli63, Oli82, Oli85, Ell81, Ell83 and Col62], and studies of the equivalent networks of these antennas [Mar86, Fel62 and Oli51].

Starting with the 80's, more advanced designs were researched, with LWA's based on dielectric waveguides, planar technologies and printed designs. [Oli81, Oli84, Jac88, Pen81 and Gug93].

In the 90's, several papers were presented, focused on beam shaping applications [Oht90, Oht91, Oht94 and Oht99], and on new structures with desired and undesired effects of the leakage [Oli63, Oli66, Oli88 and Oli90].

In the last years, the state of the art of LWA's consists in non-conventional hybrid structures that use complex guiding geometries with ferrites or metamaterials. Several of these structures will be described with more detail at the end of this section.

The basis of the "leaky wave" phenomena can be easily explained by analyzing the way a wave travels through a waveguide. The main dominant mode in a closed rectangular waveguide can be seen as the superposition of two plain wavefronts that are reflected by the walls of the waveguide with an incident angle of Θ (which varies with the frequency), as shown in Figure 2.8 -

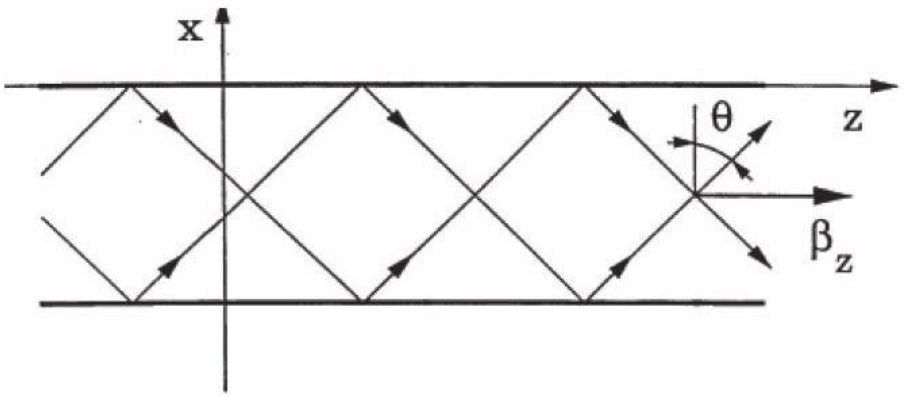

Figure 2.8 - Reflection of plane waves in a waveguide.

If a small aperture is made in one of the walls of the waveguide, part of the power is not reflected in the wall, and propagates in free space. At the same time, the reflected power continues propagating through the waveguide, with some attenuation due to the power lost in the reflection.

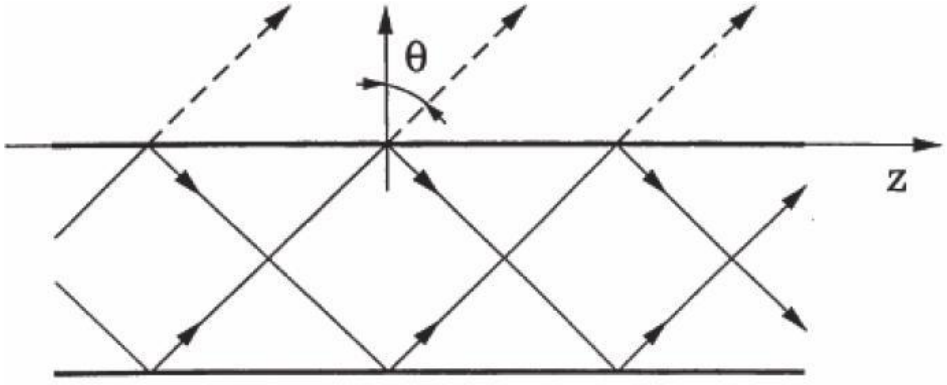

Figure 2.9 - Reflection and power coupling to free space.

The field in the aperture can be described by the complex wave number $k_z = \beta_z - j\alpha_z$: the phase constant β_z is a slight modification of propagation constant inside the waveguide, and the "leakage" constant α_z rules the loss related with the radiated power. The phase difference experienced by the wave between the apertures, will rule the direction of propagation of the radiated power. Since this phase difference depends on the frequency, different frequencies will have different propagation directions, making the LWA's frequency scanning antennas.

As a summary of all the above exposed, introducing a leakage mechanism in a waveguide, we obtain a leaky mode that couples power to a free space radiating mode, in a propagation direction that changes with frequency.

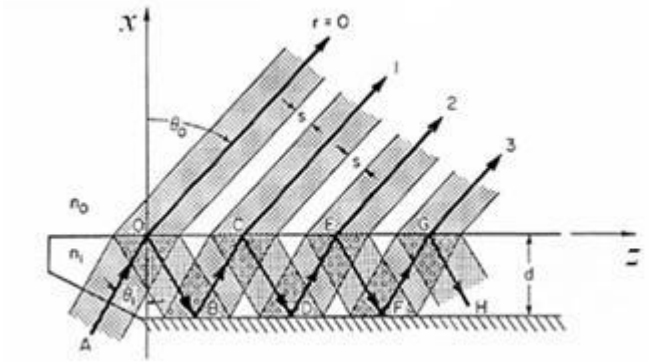

Figure 2.10 - Reflection and propagation of the leaky mode.

All the guiding structure constitutes an effective aperture for the antenna, and usually an absorbing load component has to be connected at the end of the waveguide to dissipate the remaining power; usually LWA's radiate between 90% and 95% of the input power for practical reasons, since reaching higher efficiencies would require very large structures, and very low fabricating tolerances. Since the "leakage" constant α_z controls the degree of power coupling, high values of α_z will radiate much of the power in a short length of waveguide, generating low directivities and wide beams, and low values of α_z will require greater lengths of waveguide to couple the power to free space, producing higher directivities and narrower beams. Moreover, the α_z parameter can be changed in different sections of the waveguide, and the power distribution tapered to reduce the sidelobe level, or even synthesize custom radiation patterns.

There is a strict relation between the radiation characteristics and the wave number of the waveguide propagating mode. The propagation angle is ruled by the following equation:

$$sin\theta \cong \beta_z/k_0$$

As it can be easily deducted, one problem arising from this, is the difficulty of this kind of antennas to radiate in broadside angles, perpendicular to the direction of propagation, since that would correspond to the cut-off frequency of the waveguide. It is also complicated to reach endfire angles, parallel to the propagation direction, since that would require very high frequencies compared with cut-off, allowing the generation of undesired high-order modes.

This limits the radiation of classic LWA's to just a single quadrant. However, in recent years, some advanced LWA's have been developed, making use of dielectric and metamaterial structures, capable of radiating from backfire to endfire directions. We will discuss some examples of this advanced LWA's, which were taken into consideration as starting points for the frequency scanning antenna we wanted to obtain.

The first of these structures is the one presented in [Iwa08]. In this case, the authors present a guiding structure consisting in a rectangular waveguide with tilted corrugations in one of its sides, and a narrow slot in the other, constituting the leakage mechanism. Since the corrugations are quite deep, and are tilted by some degrees, they act as short circuited stubs, but with a lower cut-off frequency than that of the main waveguide, generating right-handed or left-handed propagation, depending on the frequency. This way, the antenna is capable of scanning in forward and backward directions, from -9.9º to 2.2º in a 1.8 GHz bandwidth at 60 GHz.

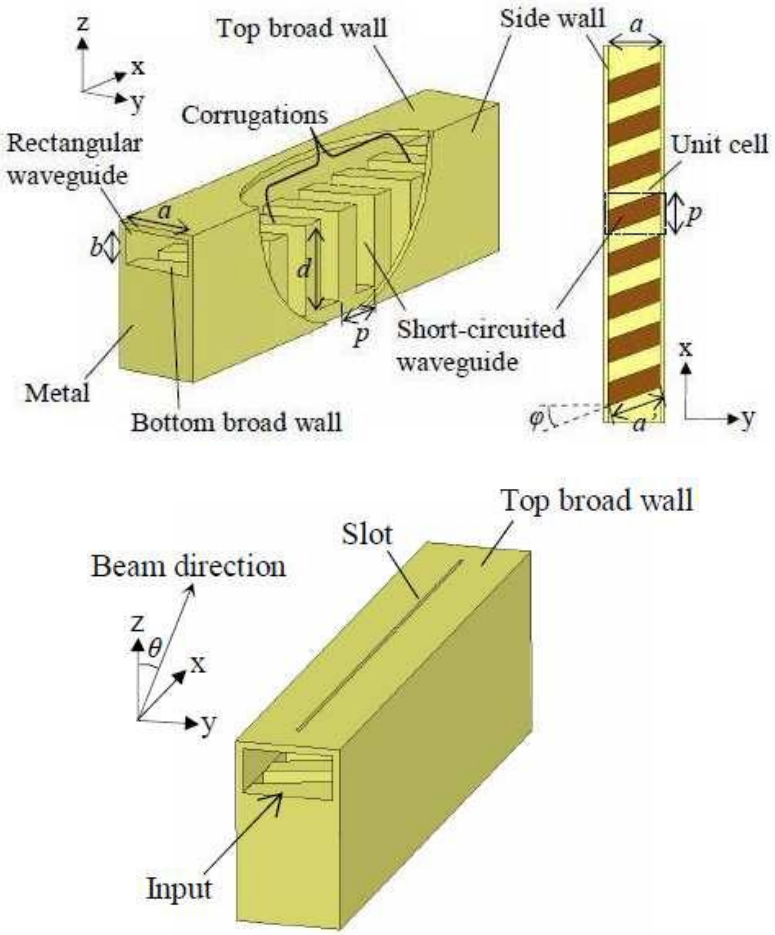

Figure 2.11 - LWA with tilted corrugations. [Iwa08]

Another structure using a stub loaded waveguide is the one presented in Fig. 2.12, this one makes use of short stubs to control the phase constant, and uses slots in the other wall of the waveguide for radiation. The working band of this antenna goes from 10 to 12 GHz achieving a scanning of 60 degrees [Ike10].

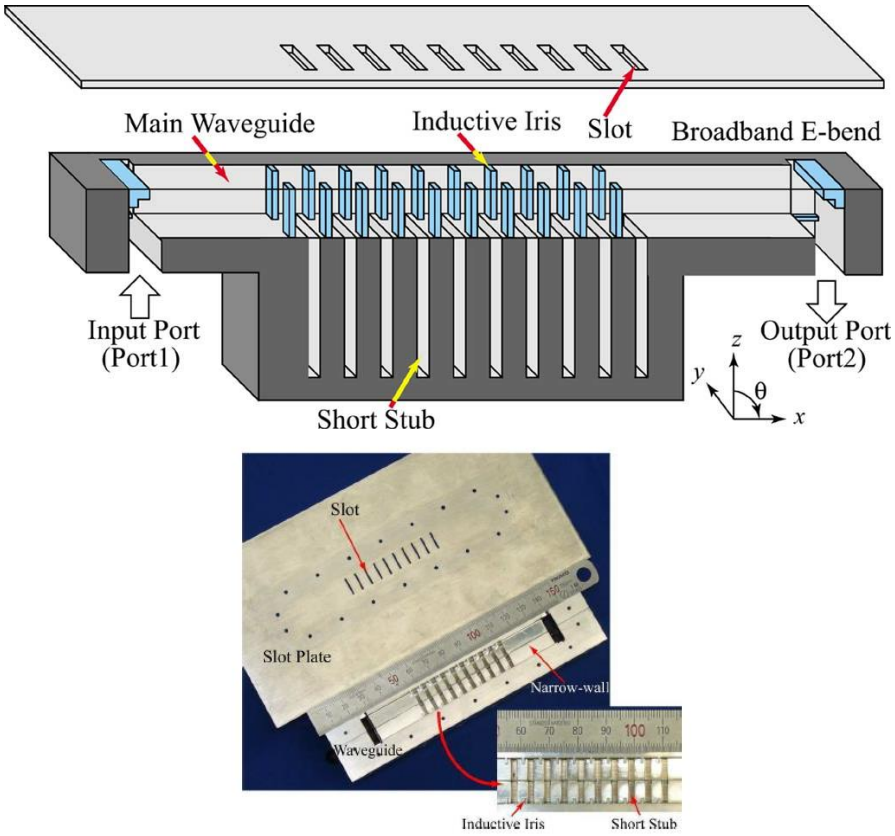

Figure 2.12 - LWA with meta-material waveguide. [Ike10]

The third structure analyzed is the one presented in [Che10], see Fig. 2.13. In this case, the waveguide used is a substrate integrated waveguide (SIW) which can be fabricated using PCB methods, reducing the cost of fabrication. This antenna can work in linear or circular polarization, with very good axial ratio. The working band of this antenna is from 33 GHz to 39 GHz, covering a 33º scanning angle.

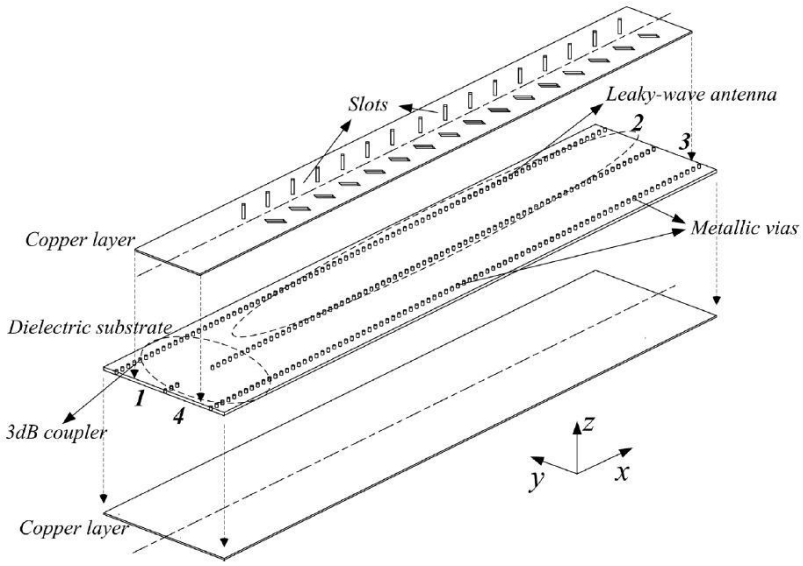

Figure 2.13 - Dual mode SIW leaky wave antenna. [Che10]

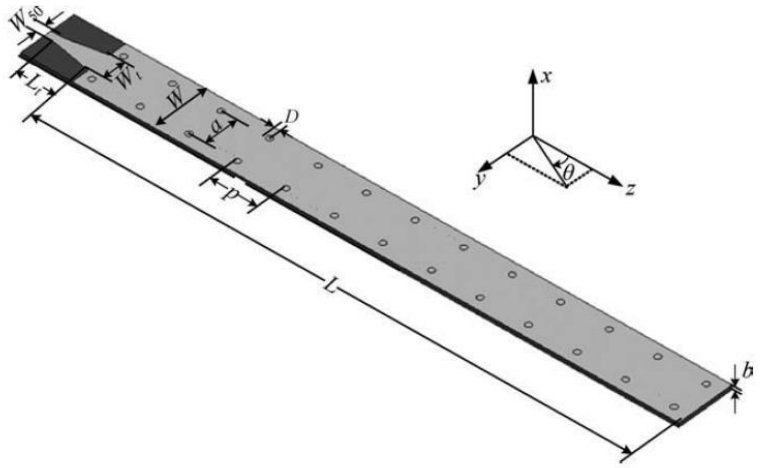

Figure 2.14 - SIW leaky wave antenna with separated bias. [Wan11]

Another structure using SIW waveguide is the one presented in [Wan11], see Fig. 2.14. In this case, the radiation mechanism is the SIW structure itself, because the vertical vias that form the lateral walls of this waveguide, are not close enough, generating a leakage

on the sides of the structure. This antenna is capable of radiating 15º in a 1 GHz bandwidth from 10 to 11 GHz.

Finally, one last SIW based structure, presented in [Xuj08] was analysed, see Fig. 2.15. In this case, the antenna uses a "half-mode" SIW structure, consisting on a traditional SIW structure cut in half. The center of the structure acts as a magnetic wall, introducing some leakage at the same time. The working band is from 25 to 28 GHz and the scanning achieved less than one degree.

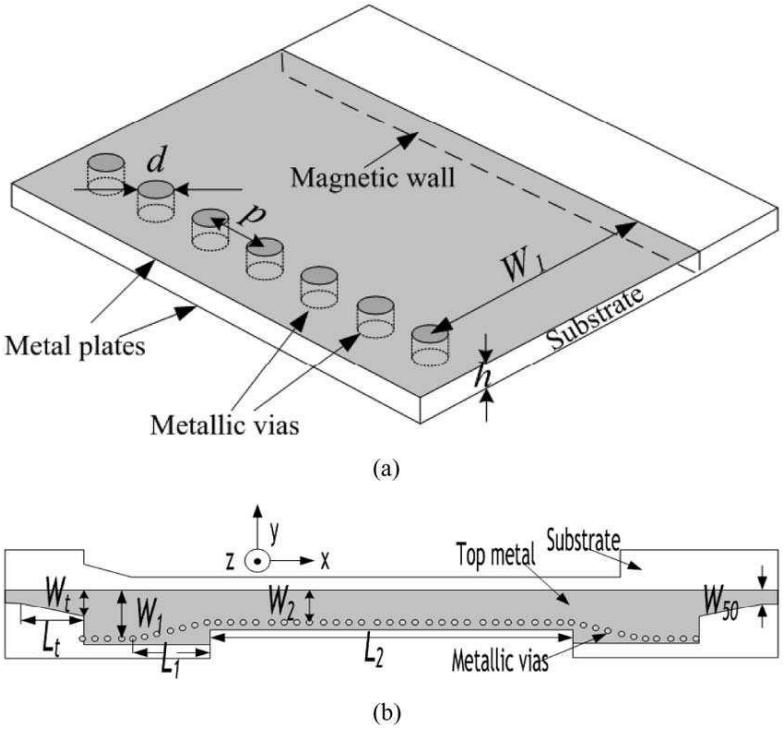

Figure 2.15 - Half-mode SIW leaky wave antenna. [Xuj08]

The main drawbacks of the analyzed approaches are usually the difficulty of the fabrication of the complex structures at high frequencies in some cases, the high losses at mm-wave frequencies when using planar substrates, and the not so good matching results

that have been obtained from simulation for the meta-material approach referenced structures. Apart from that, the analyzed antennas usually perform well in some of the necessary parameters, but lack performance in others, and no candidate was found with a good balance in terms of return loss, scanning angle, compactness and ease of fabrication. For these reasons, it was decided to explore other frequency scanning approaches that could lead to more optimal results, like phased arrays.

2.3.2 Phased Arrays

Phased array antennas consist on a group of radiating elements, ideally with an individual control over the phase and amplitude of the signal that feeds each element. By manipulating the phase and amplitude, constructive and destructive interference can be produced in arbitrary directions, and a customized radiation pattern can be synthesized. In antenna array terms, what phased arrays do is modify the array factor by controlling the phase and amplitude of the array elements. To accomplish that, phased arrays usually include amplifiers and phase shifter components on each of its individual antennas.

Phased arrays have been studied since they were first proposed in 1905 by Nobel laureate Karl Ferdinand Braun, and were further developed specially during World War II for radar applications requiring electronic scanning of the radiation beam. Nowadays, one of their main applications is on the military field, especially for radar systems that require very fast tracking and scanning capabilities, not achievable by mechanical pointing and steering systems.

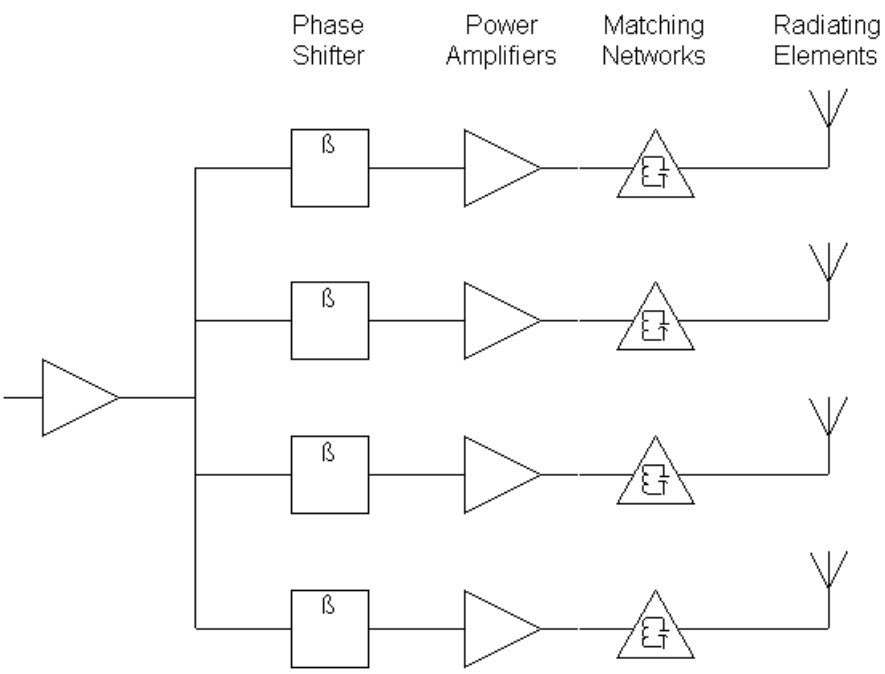

Figure 2.16 - Generic phased array block diagram.

Figure 2.17 - Example of phased array radar tracking station.

In a simpler approximation in a single dimension, if only a phase shifter is used to control the phase of the individual elements, leaving them with the same amplitude, and a linear phase change is applied to the array antennas, and angular shift of the array factor can be achieved, changing the direction of radiation of the array. The following figure shows how an equiphase front is created when such a linear phase shift is applied to the elements of an antenna array.

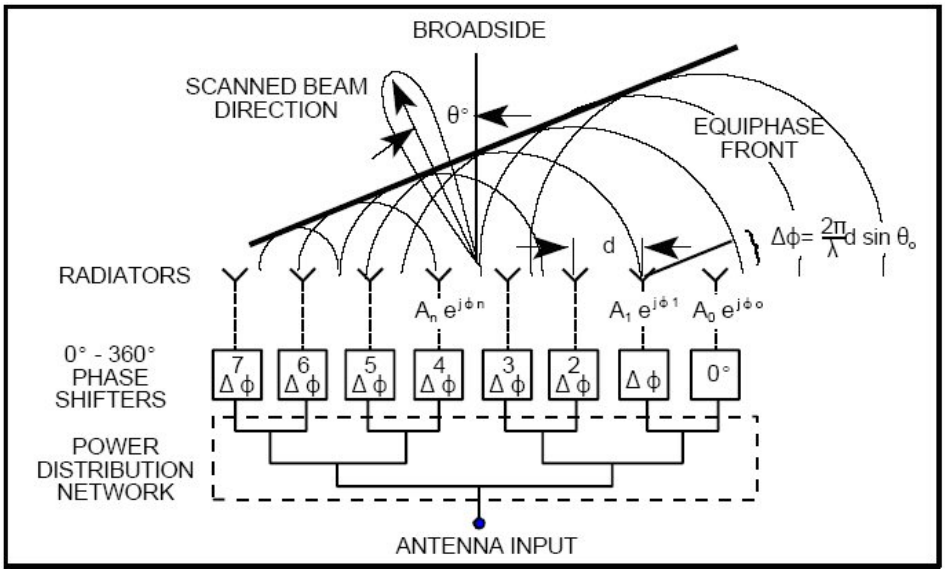

Figure 2.18 - Antenna array with linear phase offset applied to its elements.

In this case, the angle of radiation of the array θ_0, as a function of the phase offset between consecutive elements $\Delta\Phi$ and the distance between elements d, is related by the following equation:

$$\Delta\phi = \frac{2\pi}{\lambda} d \sin\theta_0$$

The exposed approach has the main drawback of requiring components like phase shifters, which increment the cost and complexity and are hard to implement at mm-wave frequencies. However, if the linear phase shift could be achieved in a way without

requiring such complex components thanks to the different path length travelled by a certain frequency bandwidth, phased arrays would be a very good option for the design of a frequency scanning antenna we are pursuing. The next section describes how this could be done.

2.3.3 Proposed Antenna Design

Pondering the above exposed about Leaky Wave Antennas and Phased Arrays, it was decided that the best approach to obtain the required Frequency Scanning Antenna design would be to use a passive phased array strategy.

To achieve that, a passive feeding network based on delay lines is proposed. A transmission line can act as a delay line, with a phase increment that depends on the frequency. If a feeding network composed by paths of different length is designed, a phase offset between consecutive elements of an antenna array that changes with frequency can be obtained, as it will be explained in more detail on the following chapters.

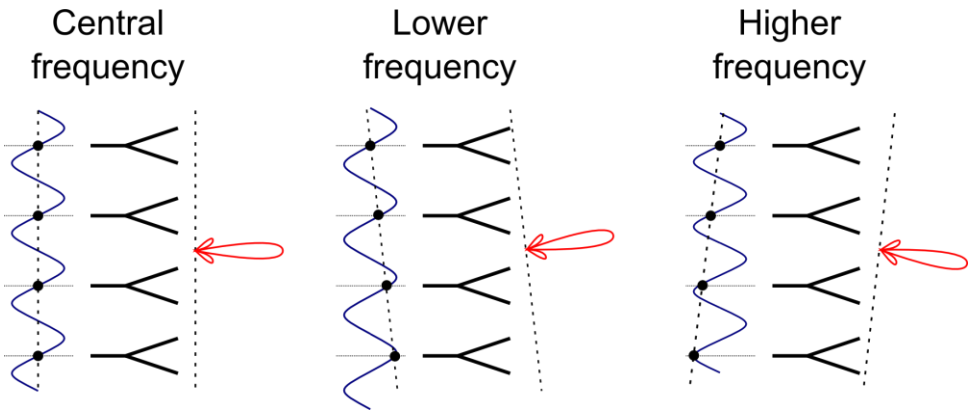

Figure 2.19 - Beam steering principle. Each operational frequency leads to a different phase shift introduced by the path length between consecutive horns.

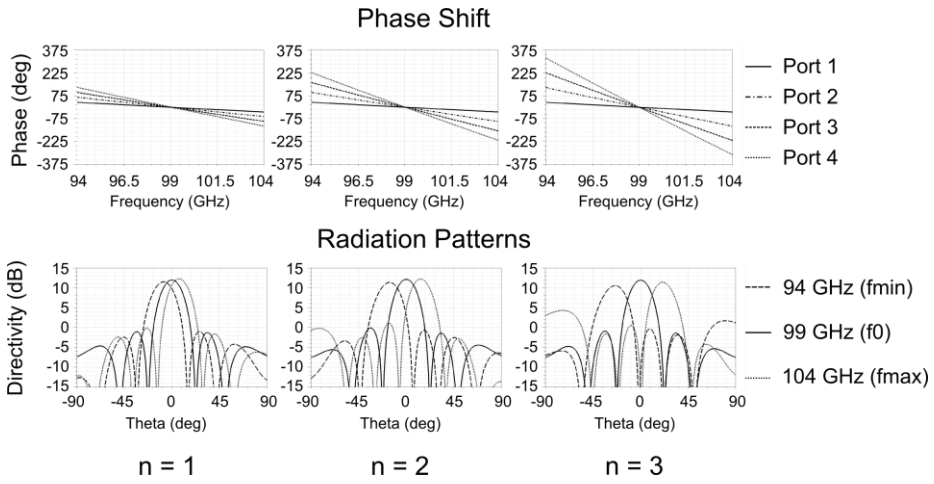

Figure 2.20 - Phase variation between the outputs of a metallic waveguide four port structure and far field radiation pattern as function of the parameter n for different frequencies.

2.4 References

[Ame13] I. Amenabar, F. Lopez and A. Mendikute, *"In Introductory Review to THz Non-Destructive Testing of Composite Mater"*, Journal of Infrared, Millimeter and Terahertz Waves, 34:152-169(2013).

[App99] R. Appleby, R.N. Anderton, S. Price, N.A. Salmon, G.N. Sinclair, J.R. Borrill, P.R. Coward, P. Papakosta and A.H. Lettington, *"Compact real-time (video rate) passive millimeter-wave imagener",* Proc. of SPIE on Passive Mill.-Wave Imaging Tech. III, Vol. 3703,13-19, April 1999.

[Ari06] S. Ariyoshi, C. Otani, A. Dobroiu, H. Matsuo, H. Sato, T. Taino, K. Kawase and H.M. Shimizu, *"Superconducting Detector Array for Terahertz Imaging Applications"*, Japanese Journal of Applied Physics, Vol. 45 No. 37, 2006.

[Bas12] M. A. Basha, A. Abdellatif and S. Safavi-Naeini, *"Low-Cost Fabrication Of millimeter-wave All-wave All-Silicon High Efficiency*

Antenna", IEEE Antennas and Propagation Society International Symposium, Chicago 2012.

[Che10] Y. J. Cheng, W. Hong and K. Wu, *"Millimeter-Wave Half Mode Substrate Integrated Waveguide Antenna with Quadri-Polarization"*, Transactions on Antennas and Propagation, Vol. 58, No. 6, June 2010.

[Col62] R. E. Collin, *"Analytical Solution for a Leaky-Wave Antenna"*, IRE Transactions on Antennas and Propagation, September 1962.

[Coo10] K. B. Cooper, R. J. Dengler, N. Llombart, A. Talukder, A. V. Panangadan, C. S. Peay, I. Mehdi, P. H. Siegel, *"Fast, high-resolution terahertz radar imaging at 25 meters"*, Proceedings of SPIE, 2010.

[Coo11] K. B. Cooper, R. J. Dengler, N. Llombart, B. Thomas, G. Chattopadhyay and P. H. Siegel, *"THz Imaging Radar for Standoff Personnel Screening"*, IEEE Transactions on Terahertz Science and Technology, Vol.1, No.1, Sept. 2011.

[Ell81] R. S. Elliott, *"Antenna theory and design"*, Prenctice-Hall Inc., Englewood Cliffs, Nj, 1981.

[Ell83] R. S. Elliott, *"An improved design procedure for small arrays of shunt slots"*, IEEE Transactions on Antennas and Propagation, Vol. AP-31, No.1, pp. 48-53, January 1983.

[Fel62] L. B. Felsen and W. K. Kahn, *"Network properties of discontinuities in multi-mode circular waveguides"*, Proceedings of the IEE- Part C: Monographs, Vol. 109, Issue: 16, pp. 388-400, September 1962.

[Fel73] L. B. Felsen and N. Marcurvitz, *"Radiation and Scattering of Waves"*, Englewood Cliffs, NJ: Prentice-Hall, 1973.

[Fri11] F. Friederich, W. von Spiegel, M. Bauer, F. Meng, M. D. Thomson, S. Boppel, A. Lisauskas, B. Hils, V. Krozer, A. Keil, T. Löffler, R. Henneberger, A. K. Huhn, G. Spickermann, P. Haring Bolivar and H. G. Roskos, *"THz Active Imaging Systems With Real-Time Capabilities"*, IEEE Transactions on Terahertz Science and Technology, Vol. 1, No. 1, September 2011.

[Gro09] E. N. Grossman, C. R. Dietlein, M. Leivo, A. Rautiainen and A. Luukanen, *"A Passive, Real-time, Terahertz Camera for Security Screening, using Superconducting Microbolometers"*, Microwave Symposium Digest, June 2009.

[Gug93] M. Guglielmi and D. R. Jackson, *"Broadside Radiation from Periodic Leaky-Wave Antennas"*, IEEE Transactions on Antennas and Propagation, Vol. 41, No. 1, January 1993.

[Han46] W. W. Hansen, *"Radiating Electromagnetic Waveguide"*, U.S. Patent No. 2,402,622, June 1946.

[Hen09] M. Henry, C. E. Free, B. S. Izqueirdo, J. Batchelor and P. Young, *"Millimeter Wave Substrate Integrated Waveguide Antennas: Design and Fabrication Analysis"*, IEEE Transactions on Advanced Packaging, Vol. 32, No. 1, February 2009.

[Hes61] A. Hessel and A. A. Oliner, *"Wave Propagation in a Medium with a Progressive Sinusoidal Disturbance"*, IEEE Transactions on microwave Theory and Techniquese, pp. 337-343, July 1961.

[Hes69] A. Hessel, *"General characteristics of travelling-wave antennas"*, Chapter 19 in Antenna Theory, McGraw-Hill, pp. 151-257, New York, 1969.

[Hor08] Y. L. Hor, J. F. Federici, and R. L. Wample, *"Non-destructive evaluation of cork enclosures using terahertz/ millimeter wave spectroscopy and imaging"*, Appl. Optics 47, 72-78, January 2008.

[Ike10] T. Ikeda, K. Sakakibara, T. Matsui and H. Hirayama, *"Beam-Scanning Performance of Leaky-Wave Slot-Array Antenna on Variable Stub-loaded Left-Handed Waveguide",* IEEE Transactions on Antennas and Propagation, Vol. 58, No. 6, June 2010.

[Iwa08] T. Iwasaki, H. Kamoda, T. Derham and T. Kuki, *"A Composite Right/Left-Handed with Tilted Corrugations for Millimeter-Wave Frequency Scanning Antenna"*, Proceedings of the 38th European Microwave Conference, October 2008, Amsterdan, The Netherlands.

[Jac88] D. R. Jackson and A. A. Oliner, *"A Leaky-Wave Analysis of the High-Gain Printed Antenna Configuration"*, IEEE Transactions on Antennas and Propagation, Vol. 36, No. 7, July 1988.

[Jos10] C. S. Joseph, A. N. Yaroslavsky, L. Lagraves, T. M. Goyette and R. H. Giles, *"Dual Frequency Continuous Wave Terahertz Transmission Imaging of Nonmelanoma Skin Cancer"*, Proc. SPIE 7601, Terahertz Technology and Applications III, 760104, March 2010.

[Kap07] B. Kapilevich, B. Litvak, M. Einat and O. Shotman, *"Passive mm-wave sensor for in-door and out-put homeland security applications"*, International Conference on Sensor Technologies and Applications, 2007.

[Kaw13] M. Kawase, K. Yamamoto, K. Takagi, R. Yasuda, M. Ogawa, Y. Hatsuda, S. Kawanishi, Y. Hirotani, M. Myotoku, Y. Urashima, K. Nagai, K. Ikeda, H. Konishi, J. Yamakawa and M. Tani, *"Non-Destructive Evaluation Method of Pharmaceutical Tablet by Terahertz-Time-Domain Spectroscopy: Application to Sound-Alike Medicines"*, Journal of Infrared, Millimeter and Terahertz Waves, 34:566-571(2013).

[Kim12] G. Kim, S. D. Lee, J. H. Moon, K. B. Kim and D. K. Lee, *"Terahertz Technology for the Detection of Food Contaminants"*, 37th Conference on IRMMW-THz, September 2012.

[Lee05] A. W. M. Lee and Q. Hu, *"Real-time, continuous-wave terahertz imaging by use of a microbolometer focal-plane array"*, Optics Letters, Vol. 30 No.10, Oct. 2005.

[Li11] L. Li, J. Yang, G. Cui, Z. Jiang and X. Zheng, *"Method of Passive MMW Image Detection and Identification for Close Target"*, Journal of Infrared, Millimeter and Terahertz Waves, 32:102-115(2011).

[Lov07] J.A. Lovberg, C. Martin and V. Kolinko, *"Video-Rate Passive Millimeter-Wave Imaging Using Phased Arrays"*, IEEE MTT-S International, June 2007.

[Mar86] N. Marcuvitz, *"Waveguide Handbook"*, McGraw-Hill, 1951, reprinted by Peter Peregrinus Ltd, London 1986.

[Mit84] R. Mittra, *"Leaky-wave antennas"*, Ch. 20 in Antenna Engineering Handbook, 2nd. Ed., R. C. Johnson and H. Jasik (eds.), New York, McGraw-Hill 1993.

[Miz05] K. Mizuno, H. Matono, Y. Wagatsuma, H. Warashina, H. Sato, S. Miyanaga and Y. Yamanaka, *"New Applications of Millimeter-Wave Incoherent Imaging"*, IEEE MTT-S International, June 2005.

[Oht90] I. Ohtera, *"Focusing properties of a microwave radiator utilizing a slotted rectangular waveguide"*, IEEE Transactions on Antennas and Propagation, Vol.38, pp. 121-124, January 1990.

[Oht91] I. Ohtera and H. Ujiie, *"Focusing properties of leaky-microwave from equiangular spiral slotted rectangular waveguide"*, Electronics and Communications in Japan (Part I: Communications), Vol. 74, Issue 12, pp. 33-43, December 1991.

[Oht94] I. Ohtera, H. Ujiie and T. Yoneyama, *"A paraboloid antenna fed by the triangular spiral-bent slotted waveguide"*, Electronics and

Communications in Japan (Part I: Communications), Vol.77, Issue 5, pp. 55-67, May 1994.

[Oht99] I. Ohtera, *"Diverging/Focusing of Electromagnetic Waves by Utilizing the Curved Leakywave Structure: Application to Broad-Beam Antenna for Radiating Within Specified Wide-Angle"*, IEEE Transactions on Antennas and Propagation, Vol. 47, No. 9, September 1999.

[Oli51] A. A. Oliner, *"Equivalent circuits for slots in rectangular waveguide"*, Microwave Res. Inst., Polytech. Inst. Brooklyn, Rep. R-234, for the Air Force Cambridge Res. Cent., under Contract AF-19(122)-3, Aug. 1951; available as NTIS order number AD653302.

[Oli63] A. A. Oliner, *"Radiating periodic structures: analysis in terms of k vs. β diagrams"*, short course on Microwave Field and Network Techniques, Polytechnic Institute of Brooklyn, New York, 1963.

[Oli66] A. A. Oliner and R. G. Malech, *"Mutual coupling in infinite scanning arrays"*, Chapter 3 in Microwave Scanning Antennas, Vol. II, R. C. Hansen, Editor, Academic, New York, 1966.

[Oli81] A. A. Oliner, S. T. Peng, T. I. Hsu and A. Sanchez, *"Guidance and leakage properties of a class of open dielectric waveguides: part II-New Physical Effects"*, IEEE Transctions on Microwave Theory and Techniques, Vol. MTT-29, pp. 855-869, September 1981.

[Oli82] A. A. Oliner and P. Lampariello, *"A novel leaky-wave antenna for millimeter waves based on the groove guide"*, Electronic Letters, vol. 18, no. 25/26, pp. 1105-1106, December 1982.

[Oli84] A. A. Oliner, *"Lumped-Element and Leaky-Wave Antennas for Millimeter Waves",* Final Report on RADC Contract No. F19628-81-K-0044, Polytechnic Institute of New York, 1984.

[Oli85] A. A. Oliner and P. Lampariello, *"The dominant mode properties of open groove guide: An improved solution"*, IEEE Trans. Microwave Theory Tech., vol. MTT-33, pp. 755-764, Sept. 1985.

[Oli88] A. A. Oliner, *"Scannable millimeter wave arrays"*, Final Report on RADC Contract No. F19628-84-K-0025, Polytechnic University, New York, 1988.

[Oli90] A. A. Oliner, "*A new class of scannable millimeter wave antennas"*, Proc. 20th European Microwave Conf., pp. 95-104, September 1990, Budapest, Hungary.

[Oli07] A. A. Oliner and D. R. Jackson, *"Leaky-Wave Antennas"*, Chapter 11 in Antenna Engineering Handbook, Volakis J. L., 4rd ed., McGraw-Hill, 2007.

[Oka08] S. Oka, H. Togo, N. Kukutsu and T. Nagatsuma, *"Latest Trends in Millimeter-wave Imaging Technology"*, PIERS Proceedings, Mar.2008.

[Pen81] S. T. Peng and A. A. Oliner, *"Guidance and leakage properties of a class of open dielectric waveguides: Part I- Mathematical Formulations"*, IEEE Transactions on Microwave Theory and Techniques, Vol. MTT-29, September 1981, pp-843-845.

[Sen09] S. Sengele, H. Jiang, J. H. Booske, C. L. Kory, D. W. van der Weide and R. Lawrence Ives, *"Microfabrication and Characterization of a Selectively Metallized W-Band Meander-Line TWT Circuit"*, IEEE Transactions on Electron Devices, Vol 56, No. 5, May 2009.

[She11] D. M. Sheen, D. L. McMakin, and T. E. Hall, *"Active Millimeter-Wave and Sub-Millimeter-Wave Imaging for Security Applications"*, IRMMW-THz, Oct. 2011.

[Sho95] 7.M. Shoucri, R. Davidheiser, B. Hauss, P. Lee, M. Mussetto, S. Young and L. Yujiri, *"A passive Millimeter Wave Camera for Aircraft Landing in Low Visibility Conditions"*, IEEE AES Systems Magazine, May 1995.

[Tam63] T. Tamir and A. A. Oliner, *"Guided Complex Waves"*, parts I and II, Proceedings IEEE, 110:310-334, 1963.

[Tam67] T. Tamir, *"Wave-Number Symmetries for Guided Complex Waves"*, Electronic Letters, Vol. 3, No. 5, May 1967.

[Wag09] M. P. Wagh, Y.H. Sonawane and O. U. Joshi, *"Terahertz Technology: A Boon to Tablet Analysis"*, Indian J. Pharm. Sci., 71(3), 235-241, May-June 2009.

[Wan11] X. M. Wang, Y. C. Jiao, Z. B. Weng and F. S. Zhang, *"Design of Leaky-Wave Antenna Based on TE10 Mode Substrate Integrated Waveguide"*, Microwave and Optical Technology Letters, Vol. 53, No.4, April 2011.

[Xuj08] J. Xu, W. Hong, H. Tang, Z. Kuai and K. Wu, *"Half-Mode Substrate Integrated Waveguide (HMSIW) Leaky-Wave Antenna for Millimeter-Wave Applications"*, IEEE Antennas and Wireless Propagation Letters, Vol. 7, 2008.

[Yin07] X. Yin, B. W. H. Ng, B. Ferguson, S.P. Mickan and D. Abbot, *"2-D Wavelet segmentation in 3-D T-ray tomography"*, IEEE Sensors J., Vol. 7, No. 3, March 2007.

[Yuj03] L. Yujiri, M. Shourcri and P. Moffa, *"Passive Millimeter-Wave Imaging"*, IEEE Microwave Magazine, Sep. 2003.

CHAPTER 3

FREQUENCY SCANNING ANTENNA ARRAY AT F-BAND, DESIGN AND RESULTS

3.1 Introduction

The main goal of this chapter is the design a F-band antenna which steers its beam in one of its axis for imaging applications. Usually, fixed beam antennas [Coo10 and Kap07], which are mechanically moved with reflectors, are used to acquire the image. Also, multiple pixel [Ari06, Gro09 nad Wei05] detectors are used, so each one receives different image position contributions and therefore the image acquisition time is minimized.

Several approaches using Leaky Wave antennas technologies were considered at the beginning of this thesis for the design of the frequency scanning antenna [Che10, Gug93, Ike08, Iwa08 and Wan11]. All of these approaches lacked a good matching over enough frequency bandwidth for our purposes. Even though, they have a radiation diagram that produces a proper illumination for a reflector system imaging setup, with good radiation patterns, low side lobes and pixel shaped appearance, suitable for imaging applications. Other solutions such as microstrip delay lines [Vaz10] or waveguide based frequency scanning approach at 300GHz [Alv13, Cam12 and Cam14] have been also considered but both require a large bandwidth to achieve wide scanning.

For the above reasons, a novel approach using a horn array with a delayed line based feeding network has been implemented in rectangular waveguide technology, resulting in a frequency scanning antenna with acceptable matching performance, wide scanning angles, high gain value, and pixel shaped beamwidth.

In particular, this approach feeds a horn antenna array using a rectangular waveguide based distribution network, so the phase at each one of the horn antenna array inputs is dependent of the frequency of the wave travelling through the feeding network, so a radiation pattern that steers with the frequency is achieved.

The design, manufacture, and measurement procedure of this antenna, together with some experimentally obtained imaging results are presented in this chapter. For the first time, the acquisition of a mm- wave image using the proposed frequency beam steering technology has been performed.

The use of this frequency scanning principle can lead to a cost effective solution for mm-wave or submm-wave imaging applications, since it reduces the number of sensors required in one of the image dimensions. A proof of concept prototype with promising results has been developed and tested to prove the validity of the proposal.

3.2 Frequency Scanning Antenna Array

3.2.1 Working principle

First, in order to achieve the objective of sweeping the targets electronically steering in one of the two axes, a mm-wave frequency dependent beam steerable array antenna has been designed. The antenna is composed by two different components that can be designed separately, an array of horn antennas and their corresponding feeding network.

The feeding network has been designed to generate a linear phase ramp at the output feeding ports of the network,

corresponding to each horn antenna. Since the slope of the phase ramp will change with frequency, so will the phase difference between the ports, and the resulting radiation beam will steer, see Figure 3.1.

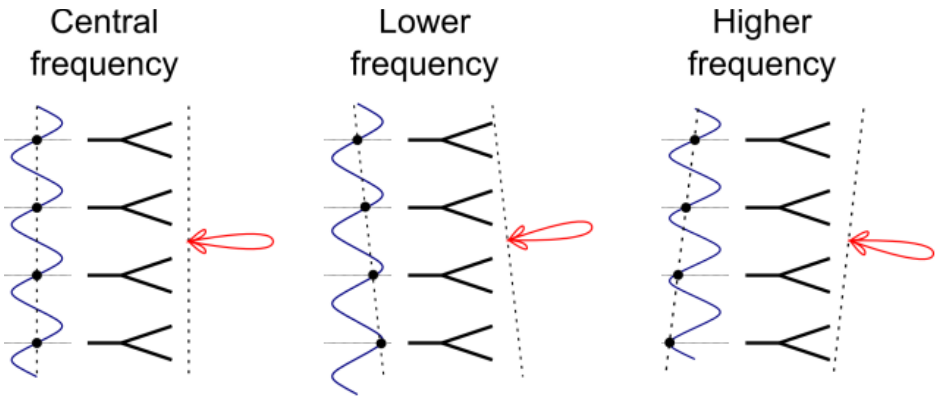

Figure 3.1 – Beam steering principle.

The feeding network structure supplies the appropriate incremental phase needed to achieve the beam steering with frequency, to each horn of the array. In particular, a phase difference of 2πn radians (with n being an integer number) between consecutive horns, at the central working frequency f_0 has to be guaranteed, in order to obtain a radiation beam perpendicular to the array. To get the required phase ramp a metallic rectangular waveguide structure with a different path length for each of the feeding lines connected to the horns have been used.

As the phase shift at f_0 is always a multiple of 2π, all horns are in-phase and the radiation pattern of the array has its main lobe in the boresight direction. However, at frequencies different from f_0, due to the dispersion of the waveguide, the phase shift between consecutive horns is not an integer multiple of 2π anymore,

generating a phase slope of at the input of the horn array that steers the radiation pattern, see Figure 3.1 and Figure 3.2.

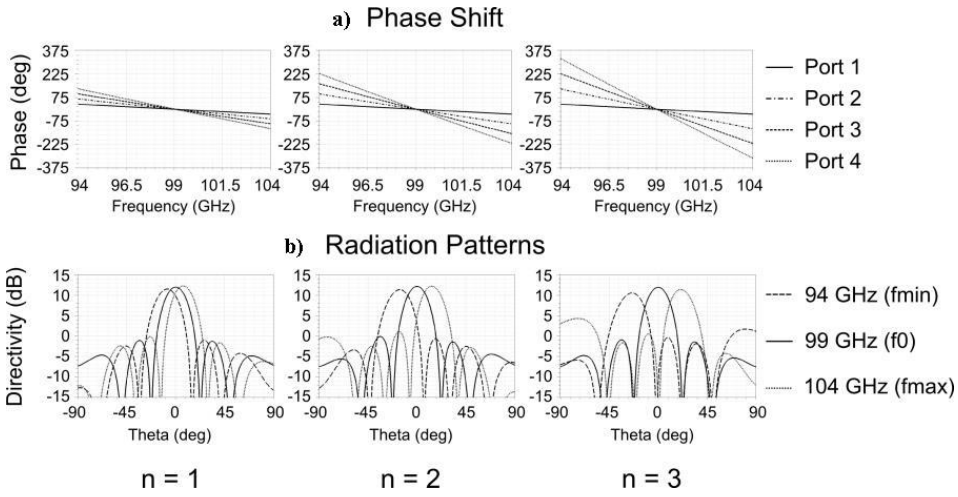

Figure 3.2 – (a) Phase variation between the outputs of a metallic waveguide four port structure. (b) Far field radiation pattern as function of the parameter n for different frequencies.

It is important to notice that the parameter n value controls the maximum value of the scanning angle. In particular, for a fixed value of the operational bandwidth around f_0, a certain amount of scanning angle will be obtained for a value of n. Conversely, if higher values of *n* are chosen, the phase shift between horns will increase for the same frequencial displacement from f_0, and wider scanning angles will be obtained for the same operational bandwidth, see Figure 3.2. A compromise between scanning angle and purity of radiation pattern must be selected since wider scanning angles produce higher scan loss in the resultant radiation pattern and higher sidelobes.

As, in theory, arbitrarily high values of parameter n can be used, it could be possible to obtain very wide scanning angles with this kind of feeding network, even for small operational bandwidths. However,

in practice, high values of *n* require very long paths in the feeding network; therefore, the size and the subsequent losses in the metallic waveguides will enforce an upper limit and also the aforementioned fact that scan loss and sidelobes will increase with the scanning angle. Nevertheless, wide scanning angles of about 40º with a quite compact structure can be achieved. In Figure 3.2, the output phase differences and far field radiation patterns for several values of n parameter, in a four port feeding network working from 94 to 104 GHz, are shown, illustrating the previously exposed principle. As a consequence of increasing the n parameter the increase of the scan loss and higher side lobes, are also observed.

To achieve the necessary path differences in each one of the output ports of the feeding network, the two approaches presented in Figure 3.3 can be taken into account. The first one uses a series feeding scheme [Che86 and Wan01]; where the splitters are placed at the input of each horn, feeding the horn and also the next splitters and horns, in a series scheme. Phase delay waveguide sections are introduced between each splitter to obtain the desired phase difference between consecutive horns, with the length of these sections controlling the n parameter. The problem of this approach relies on needing to have the same power at the input of each horn antenna to maximize the aperture efficiency. This requirement leads to having to use uneven distribution power splitters, and with an asymmetry that gets larger with each consecutive splitter. The fabrication process for these splitters is more difficult and expensive, or even unfeasible for very uneven splittings at very high frequencies [Li06].

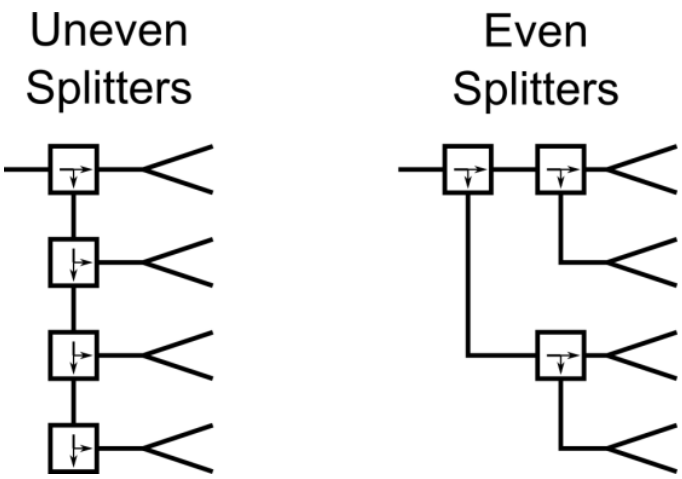

Figure 3.3 – Uneven (series) and even (parallel) splitter approaches for the feeding network.

Conversely, the second approach is based on a parallel feeding scheme. In this case, each path incorporates all the accumulative length difference with respect to the first output port, to obtain the linear phase ramp at the output ports. This configuration requires a reduced number of power splitters in comparison with the first option, and the power splitters are always even, reducing the difficulty and cost of fabrication. The main drawback of this approach is that it requires a larger space to accommodate all the waveguide branches, and limits the number of output ports to a power of two. In Figure 3.4, an example of a four port feeding network using even power dividers with proportional path lengths is shown.

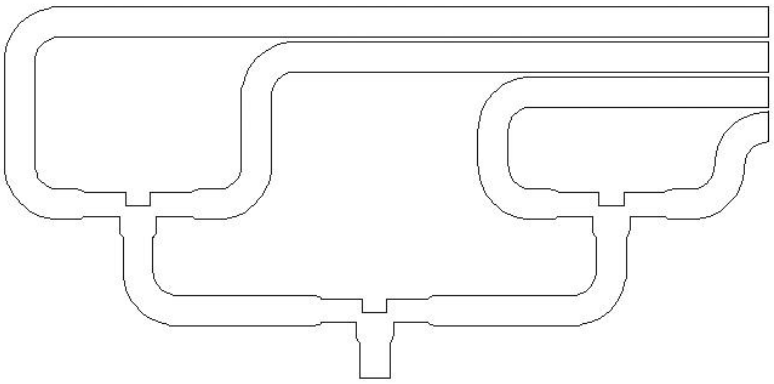

Figure 3.4 – Schematic of a four port parallel feeding network configuration.

3.2.2 Feeding Network. Proposed structure.

Based on the working principle described in the previous section, a feeding network working at a central frequency of 100GHz has been designed. The selected feeding network is based on the previously presented parallel approach, and composed of WR-8 waveguide sections (2.032 mm x 1.016mm).

As a first task, several junctions with different shapes were simulated in order to choose the better option for our application.

A rectangular Y-junction in the H-plane was modelled with the simulation software Mician μwave Wizard [Mic15] and the obtained results are depicted in Fig. 3.6. The matching is under -10 dB for the whole band of interest.

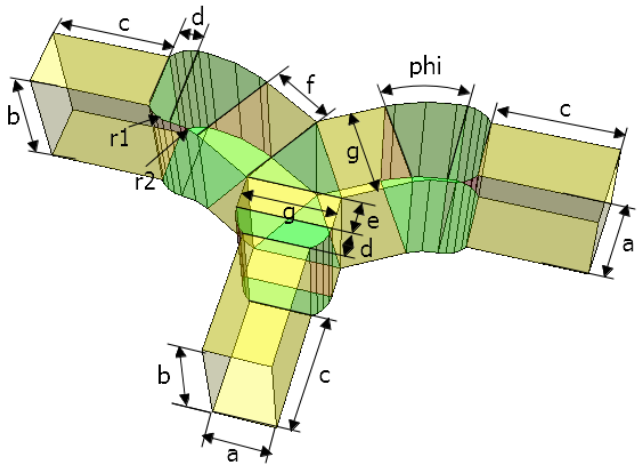

Figure 3.5 – Y-junction designed with Mician μwave Wizard.

Table 3.1 – Parameters for the Y-junction in mm.

a	b	c	d	e	f	g	phi	r1	r2
1.016	2.032	2	0.5	0.55	1.11	1.47	30°	0.5	1

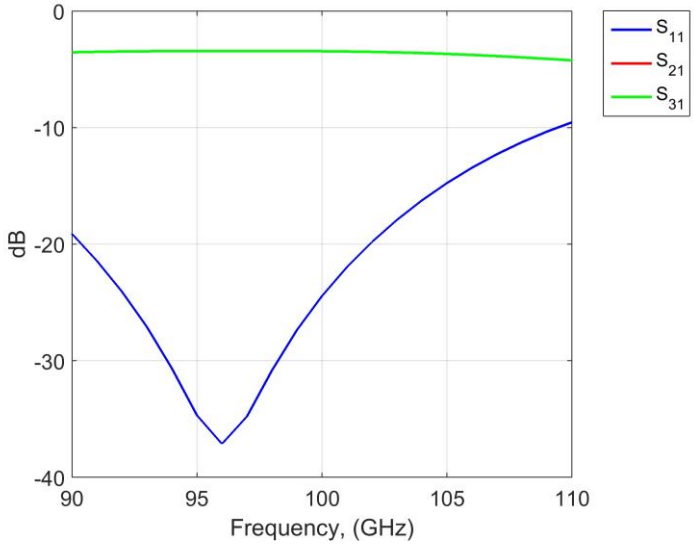

Figure 3.6 – Simulated S parameters for a Y-junction with Mician μwave Wizard Software.

The next T-junction to be simulated was a rectangular waveguide junction with compensation insert. The insert is located opposite to port 1 and has rounded corners to simulate the effect of the milling tool. The results for the simulation are presented in Figure 3.8.

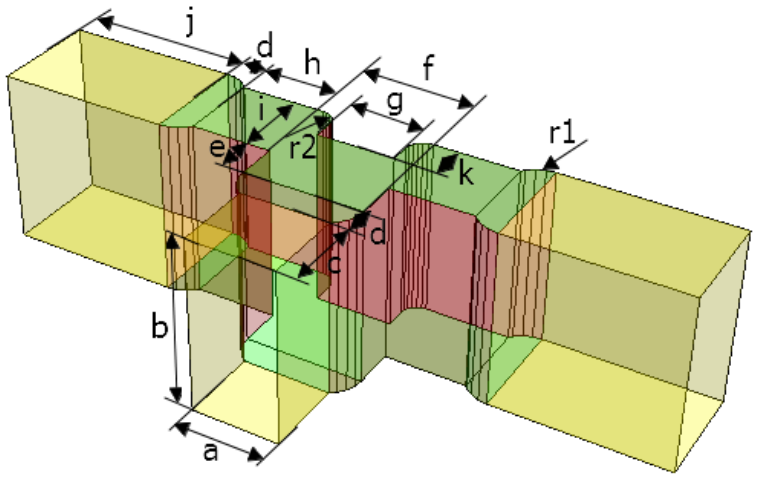

Figure 3.7 – Rectangular T-junction with insert.

Table 3.2 – Parameters for the T-junction with insert in mm.

a	b	c	d	e	f	g	h	i	j	k	r1	r2
1.016	2.032	0.94	0.4	0.49	1.38	0.9	0.94	0.96	2	0.44	0.4	0.2

It can be seen that the S_{11} is under -22 dB for the working band.

Next, a Rectangular waveguide T-junction with compensation triangular insert was tested. The insert is located opposite to port 1, again with rounded corners. The matching achieved is under -18 dB for the band of interest as it can be observed in Figure 3.10.

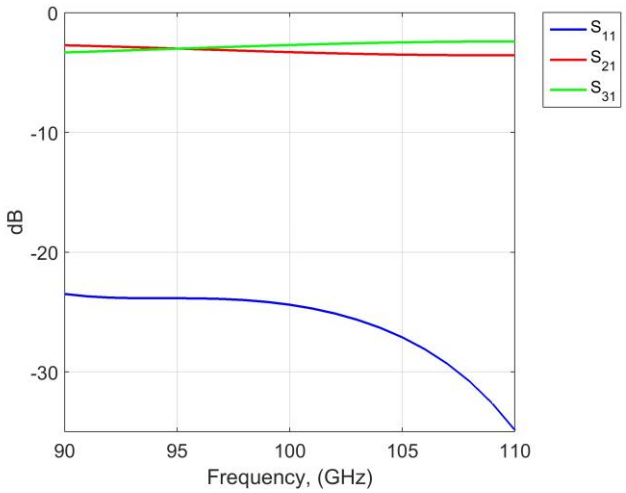

Figure 3.8 – S-parameters for a rectangular T-junction with inserts simulated with Mician μwave Wizard.

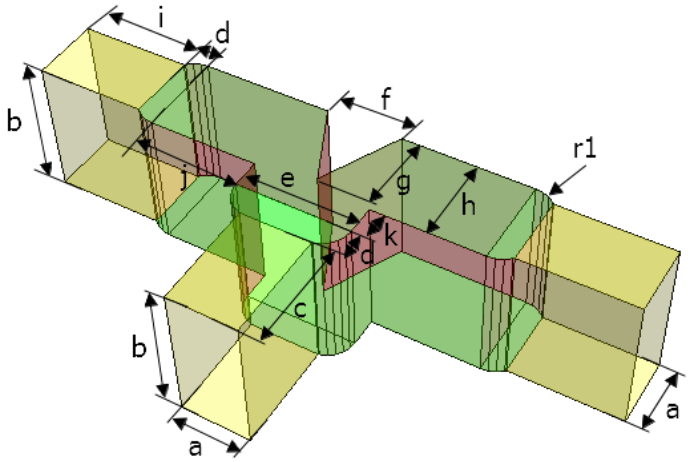

Figure 3.9 – Rectangular T-junction with a triangular insert.

Table 3.3– Parameters for the T-junction with a triangular insert in mm**.**

a	b	c	d	e	f	g	h	i	j	k	R1
1.016	2.032	1.57	0.4	1.64	1.08	1.13	1.28	1.6	1.57	0.42	0.4

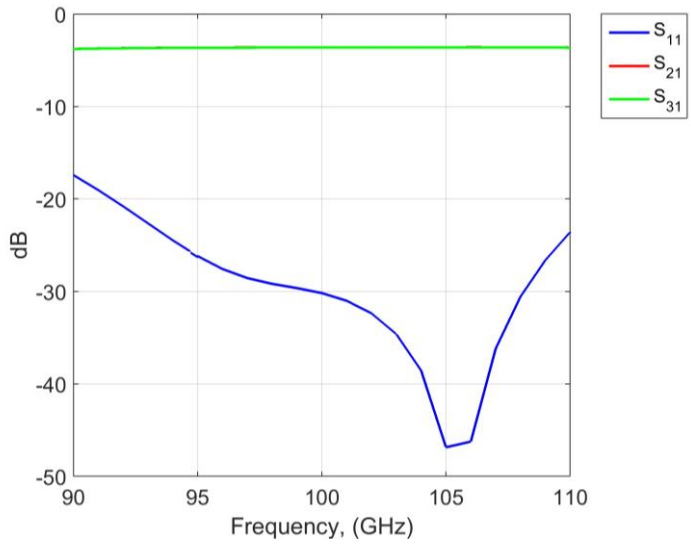

Figure 3.10 – S-parameters for a T-junction with a triangular insert simulated with Mician μwave Wizard.

Next, a standard waveguide T-junction without any insert was simulated. The matching achieved is under -10 dB for the band of interest as it can be observed in Figure 3.12.

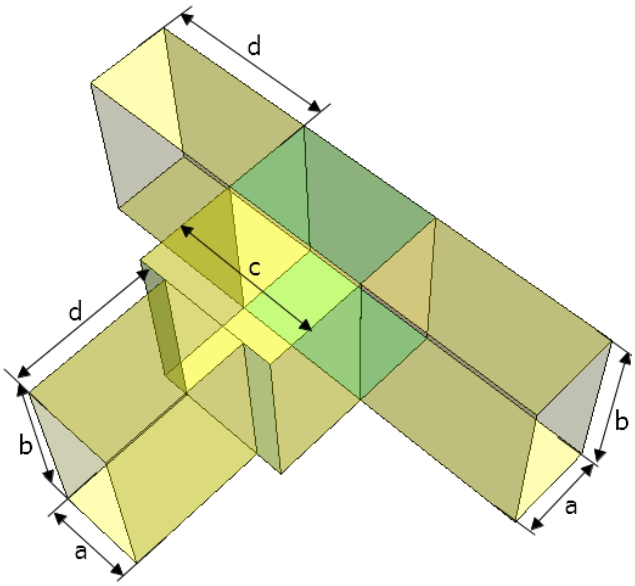

Figure 3.11 –Rectangular T-junction.

Table 3.4 – Parameters for the T-junction in mm.

a	b	c	d
1.016	2.032	1.68	1.6

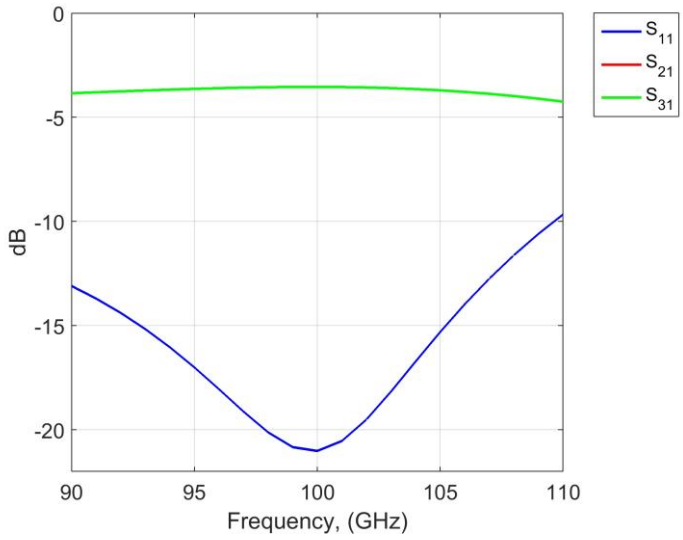

Figure 3.12 –S-parameters for a Rectangular T-junction simulated with Mician μwave Wizard.

The last element to be tested was the Hybrid ring. It has a simple form and the fabrication is easier than the other options, with the exception of the simple T-junction. The adaptation is below 15 dB for the working band for both simulations, but in this case, some unbalance between the output ports can be observed at the band edges, due to the asymmetry of the structure, see Figure 3.14 and Figure 3.15.

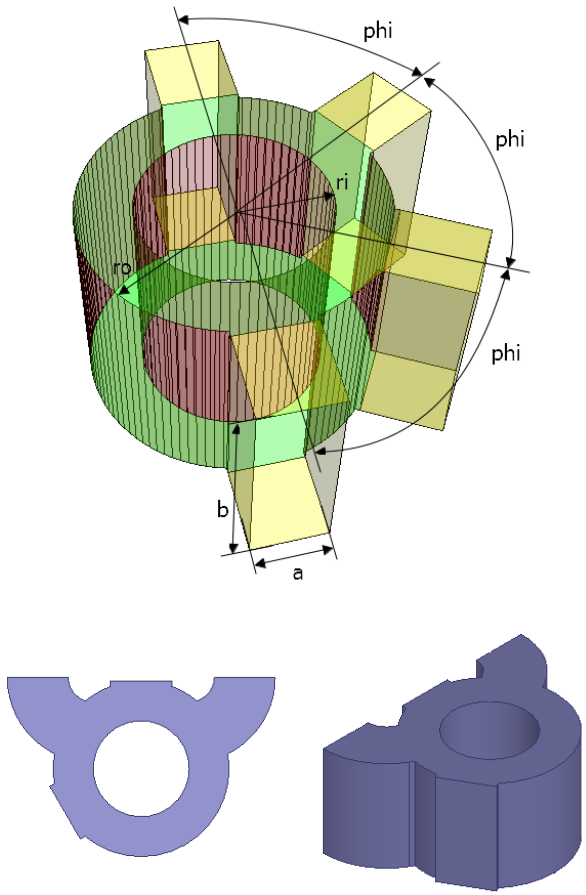

Figure 3.13 – Hybrid rings depicted with Mician Microwave Wizard and Ansys HFSS.

Table 3.5 – Parameters for the Hybrid ring in mm**.**

a	b	Phi	ri	ro
1.016	2.032	60º	0.8	1.464

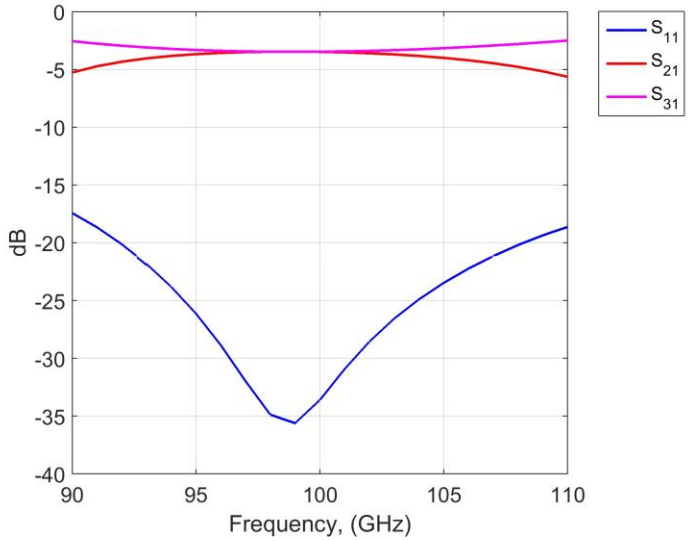

Figure 3.14 –Hybrid ring simulated with Mician μwave Wizard.

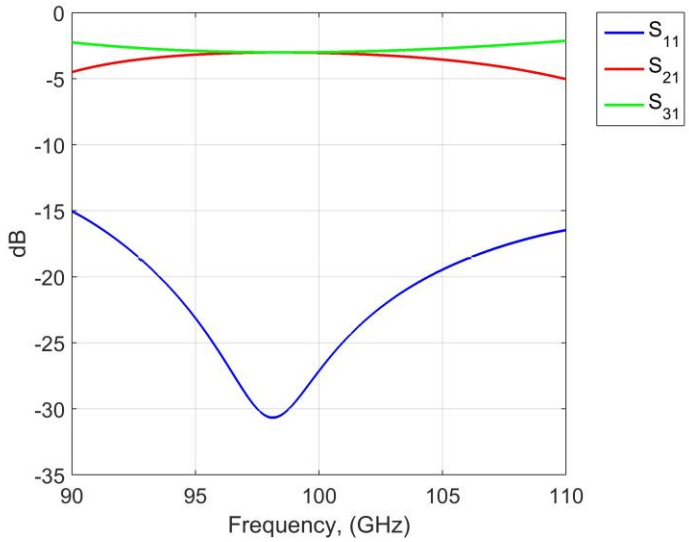

Figure 3.15 –Hybrid ring simulated with Ansys HFSS.

Table 3.6 – Splitter's comparison.

Splitter	S_{11} (dB)	Fabrication complexity
Y-junction	-10	Medium
T-junction with inserts	-22	Medium
T-junction with triangular insert	-18	High
T-junction	-10	High
Hybrid ring	-15	Low

After careful analysis of the results, it was decided to implement the even power splitter elements with the hybrid ring component, which is easier to fabricate with traditional milling techniques than the other T-shaped splitter designs considered. These couplers have the additional advantage of introducing an extra phase shift between their outputs that can be added to the one achieved by the different paths, reducing the overall length, and resulting in a more compact structure. The main drawback of these power splitter structures is the unbalance they introduce at the frequency band edges, as it will be seen later in this chapter and we will have to take into consideration how to terminate the hybrid ring extra port that will not be used.

Several bends are needed for the distribution network, with bending angles of 30, 60 and 90 degrees. Classical mitter bends would require the use of very small milling tools, so curved bends have been chosen for ease of fabrication reasons. The curved bend structures have been simulated for 30, 60 and 90 degree bending angles.

Table 3.7 – Parameters for the bends in mm.

a	b	ri	ro
1.016	2.032	0.8	1.816

- 90 degrees bend.

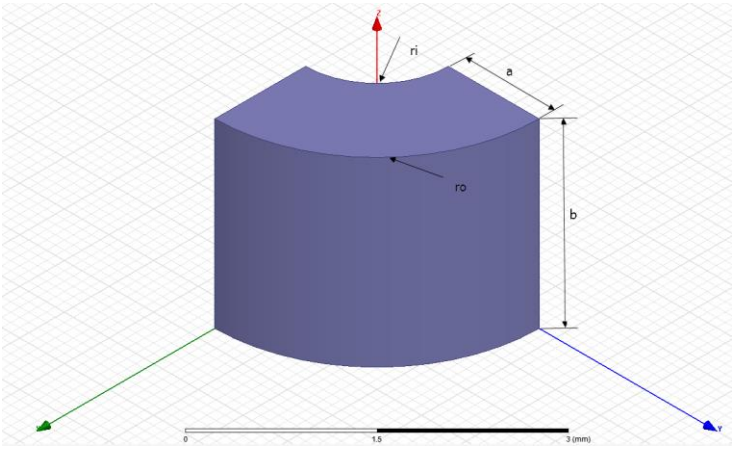

Figure 3.16 – 90 degrees bend depicted with HFSS.

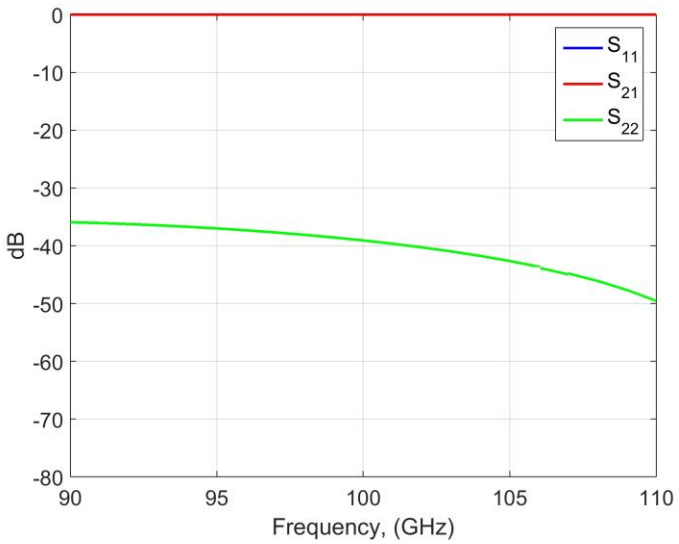

Figure 3.17 – Results of the μwave Wizard simulation for the 90 degrees bend.

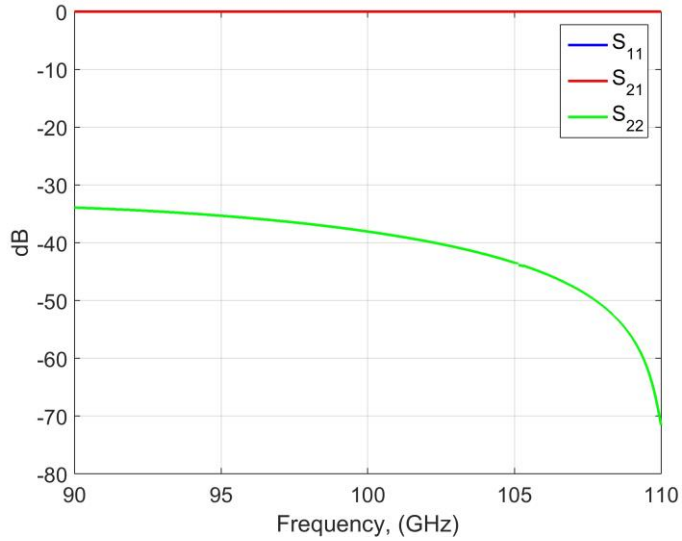

Figure 3.18 – Results of the HFSS simulation for the 90 degrees bend.

- 60 degrees bend

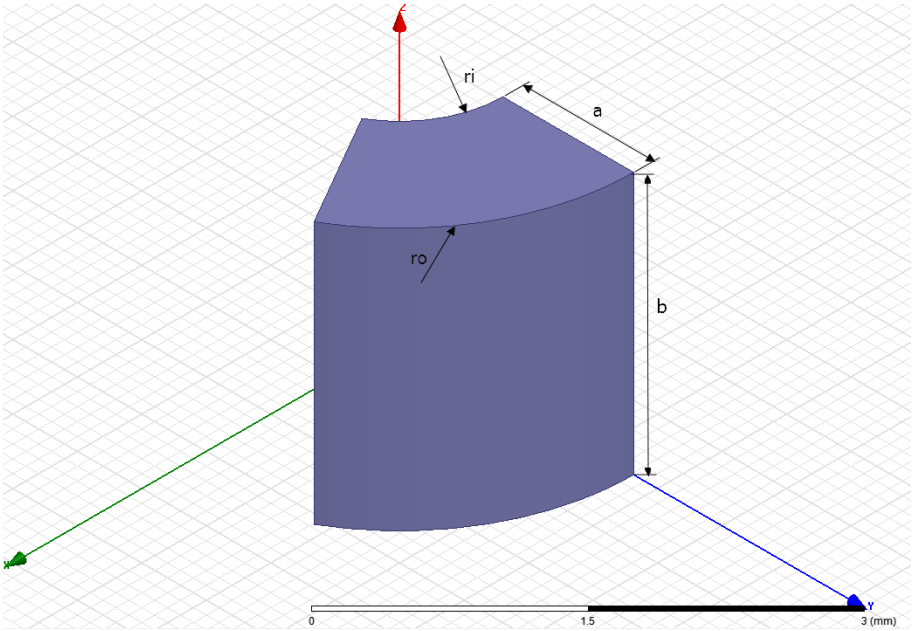

Figure 3.19 –60 degrees bend depicted with HFSS.

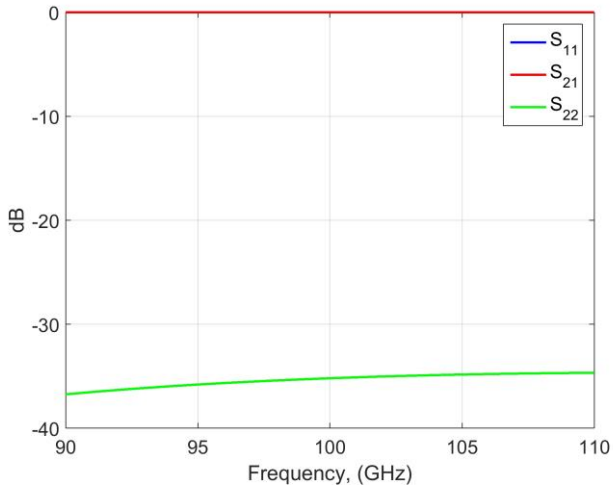

Figure 3.20 – Results of the μwave Wizard simulation for the 60 degrees bend.

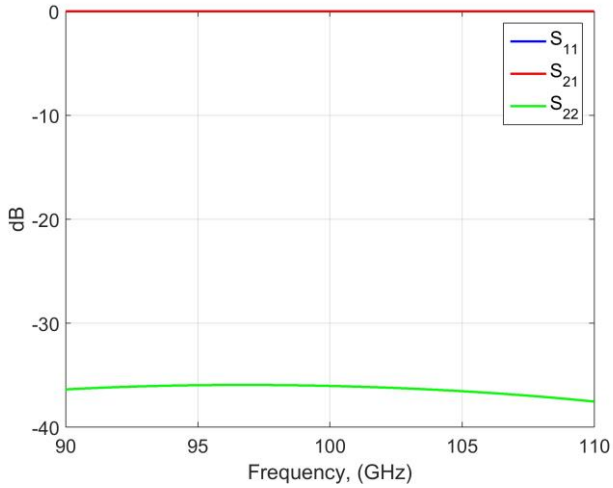

Figure 3.21 – Results of the HFSS simulation for the 60 degrees bend.

- 30 degrees bend

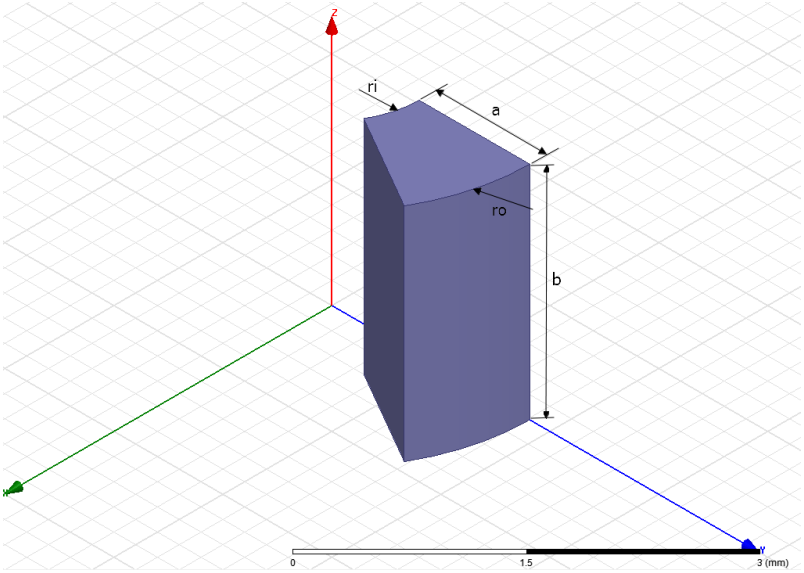

Figure 3.22 –30 degrees bend depicted with HFSS.

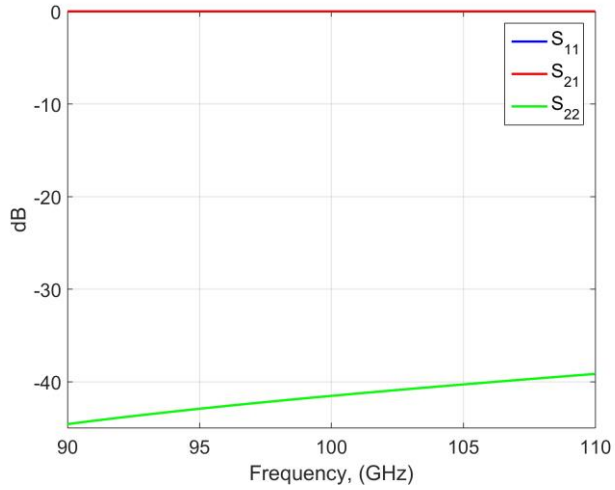

Figure 3.23 – Results of the μwave Wizard simulation for the 30 degrees bend.

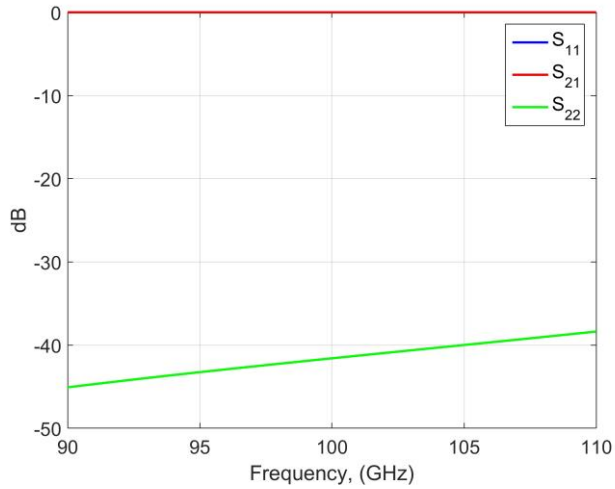

Figure 3.24 – Results of the HFSS simulation for the 30 degrees bend.

A good matching has been achieved for the three simulated bends under -30 dB for all the elements.

Furthermore, with the objective of optimizing the space and reducing the size of the feeding network, stepped wider sections in the WR-8 waveguide with a size of 2.832 mm x 1.016 mm have been implemented, see Figure 3.25. These sections have the effect of reducing the value of the guided wavelength λ_g, and therefore, the physical length of the waveguide needed to achieve the phase difference between horns, can be shorter. Figure 3.25 shows the detail of the stepped waveguide sections. The design of this stepped component was done with a tapered change of the waveguide width, in order to minimize the S_{11} parameter of the section, and taking into account the rounding effects of the milling tool used for the fabrication process, and the discrete penetration height steps of the tool.

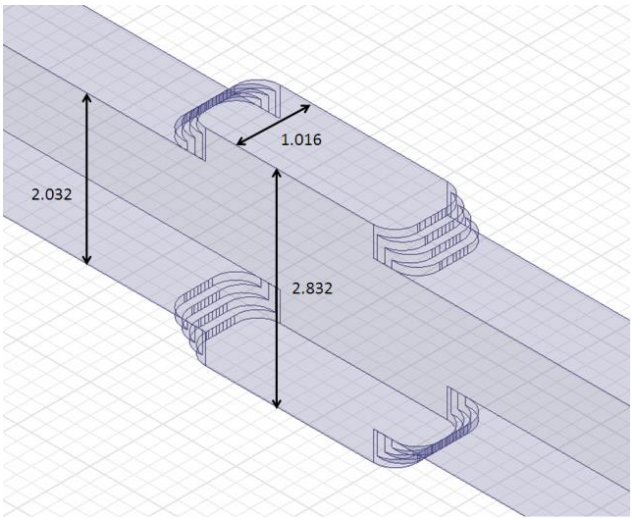

Figure 3.25 – Stepped waveguide sections.

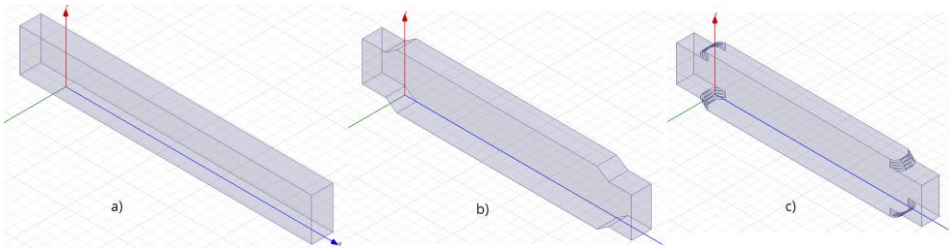

Figure 3.26 – Waveguide section a) without step, b) with ideal step and c) with fabricable step.

In order to see the increment of the electrical length achieved by using these stepped sections the electrical field of three waveguide sections with the same physical length has been represented in the following figures.

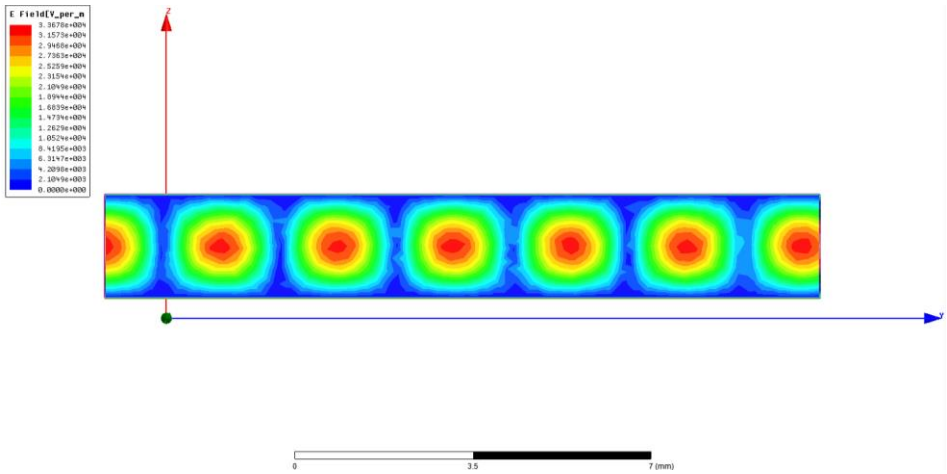

Figure 3.27 E-field distribution in the waveguide without step.

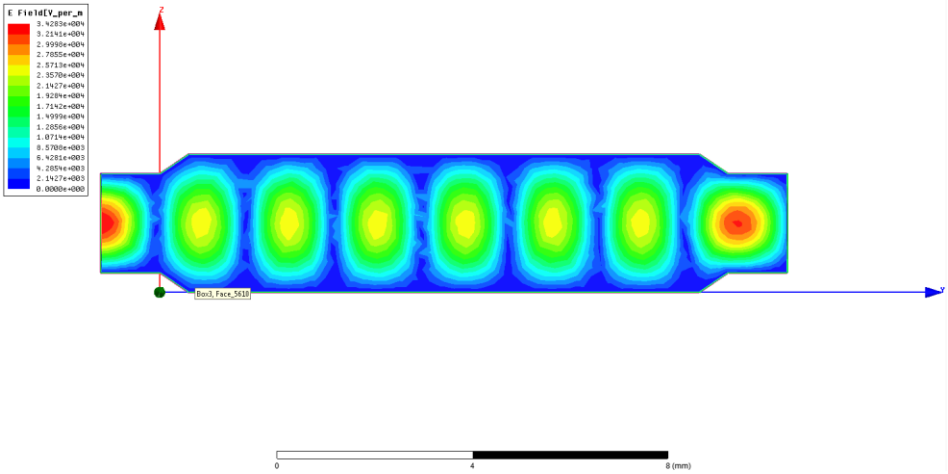

Figure 3.28 E-field distribution in the waveguide with an ideal step.

As it can be observed in the pictures, for the same length of waveguide, the electrical length of the section without step is of 3 lambdas approximately, while the ideal and fabricable stepped sections have almost 4 lambdas of electrical length.

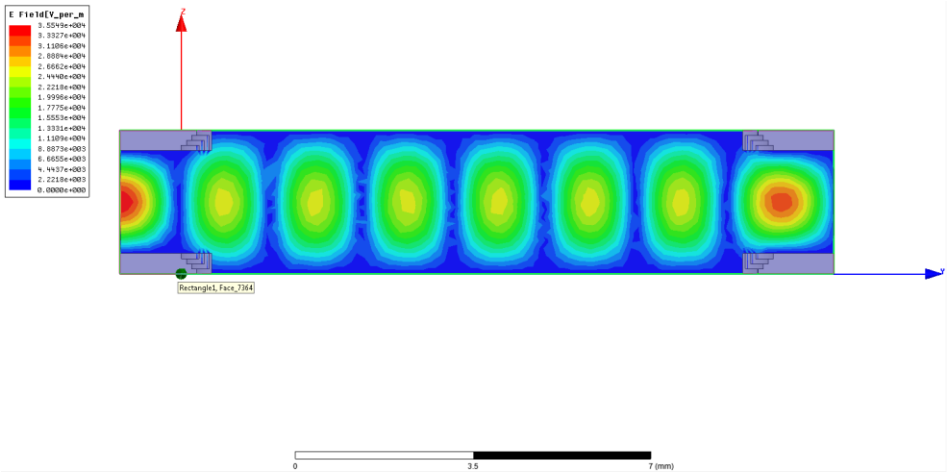

Figure 3.29 E-field distribution in the waveguide with a fabricable step.

After designing the individual components of the distribution network, the next step is integrating them in the whole network, and adjusting the waveguide section lengths to obtain the desired phase difference between the output ports. Several values of the parameter n were considered, as a previous step to determine the required length of the waveguide sections. In particular, a value of n=2 was selected since it was considered that the resulting beam scanning angle was enough to scan the desired FoV while keeping a compact feeding network at the same time.

The resultant feeding network layout is shown in Figure 3.30, with the stepped sections highlighted with a different colour.

The distance between output ports has been set to 2mm (0.6 λ) in a compromise between minimizing the grating lobes that are present in the array radiation patterns when the individual antennas are very separated, and the technological difficulties of fabricating the horn array if the elements are too close.

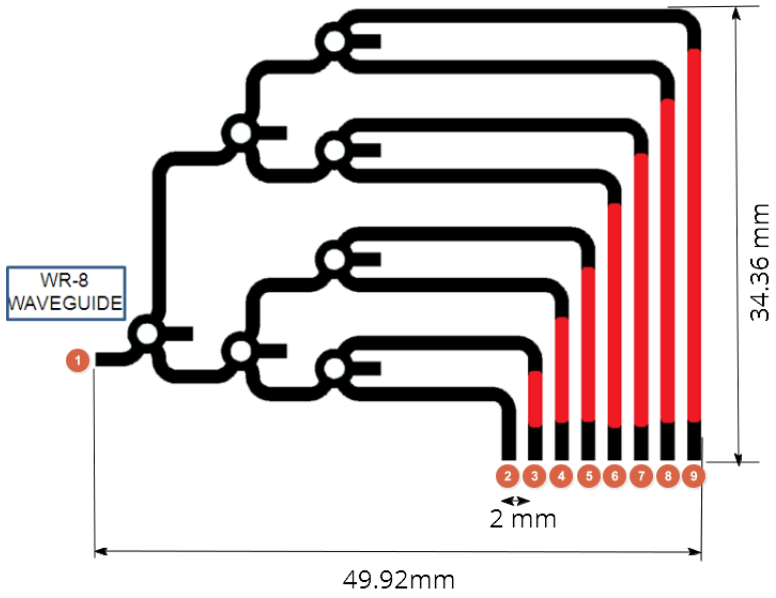

Figure 3.30 – Layout of the proposed feeding network with the added stepped waveguide sections.

One we have designed the different necessary elements a simulation of the network before attaching the antenna has been done with Mician μwave Wizard and with Ansys HFSS [Hfs15].

In Figure 3.31 the schematic for the complete feeding network is presented. The hybrid ring fourth port has been attached to a load.

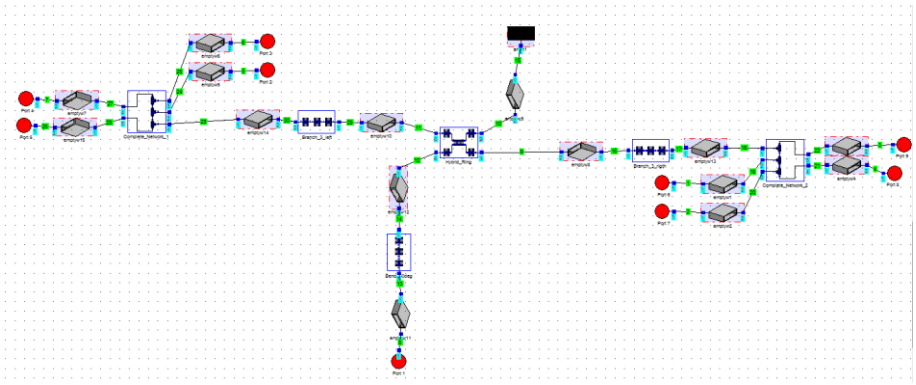

Figure 3.31 – Schematic of the proposed feeding network simulated with Mician μwave Wizard.

The results of magnitude and phase have been depicted for both simulations. In Figure 3.32 and Figure 3.33 simulations with Mician μwave Wizard are presented.

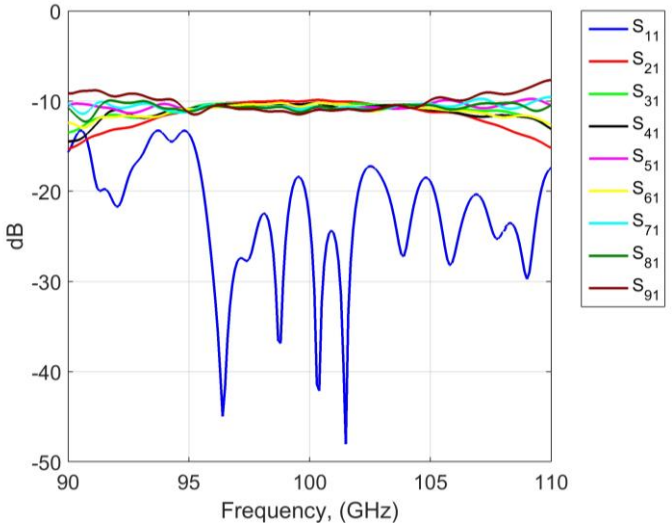

Figure 3.32 – S-parameters magnitude obtained at the output ports of the proposed feeding network simulated with Mician μwave Wizard.

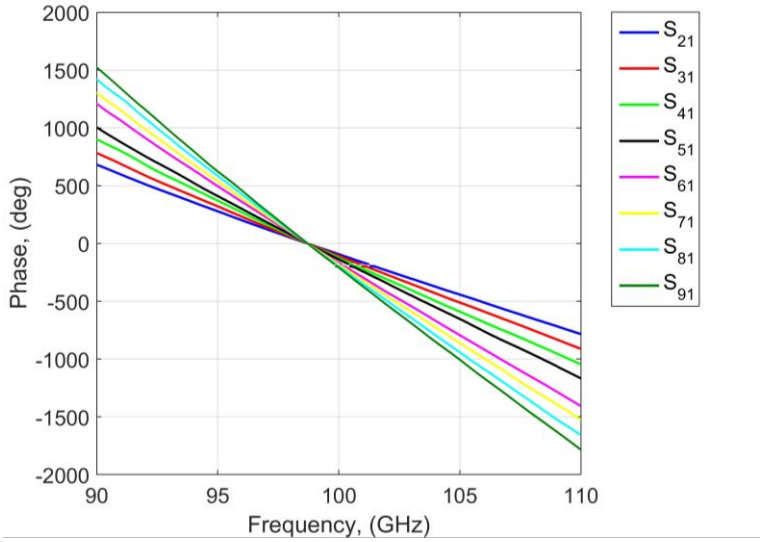

Figure 3.33 – Phase obtained at the output ports of the proposed feeding network simulated with Mician μwave wizard.

The same results obtained with Ansys HFSS are presented in Figure 3.34 and Figure 3.35.

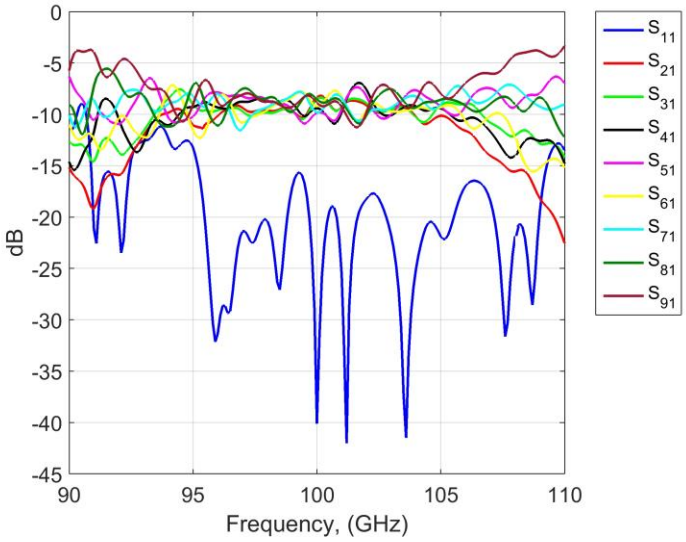

Figure 3.34 – Magnitude obtained at the output ports of the proposed feeding network simulated with Ansys HFSS.

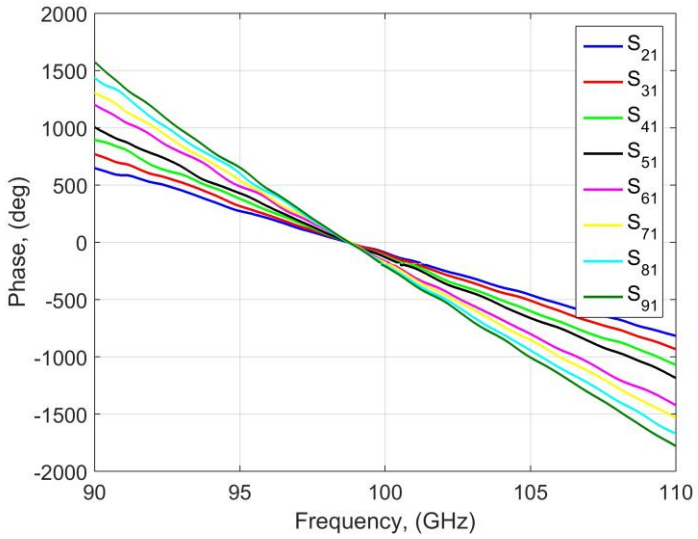

Figure 3.35 – Phase obtained at the output ports of the proposed feeding network simulated with Ansys HFSS.

A matching value below -10 dB is obtained for the band of interest. The power distribution over the output ports is quite regular in the center of the band, although noticeable unbalance can be observed at the band edges, mainly due to the unbalance introduced by the hybrid rings in those frequencies.

The phases comply with the desired linear phase ramp at the output ports of the network, with the cero crossing (corresponding to the boresight beam) at 99 GHz.

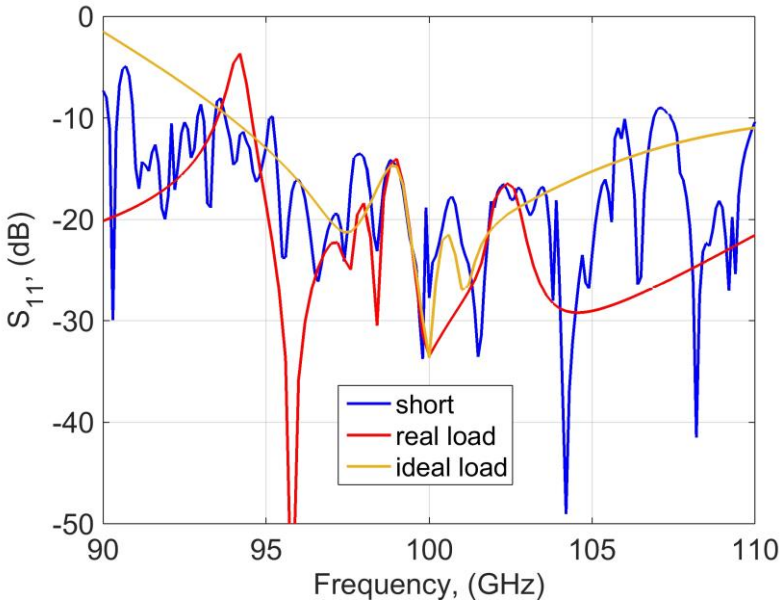

Figure 3.36 S_{11} for the complete structure with the four.

Taking into account the achieved results, it was decided to finish the ports with a short, because although the best results would be achieved by introducing an ideal load, the available real load consisting on a lossy graphite conical spike, leads to slightly worse results than in the short ended case.

3.2.3 Radiating elements

Once the feeding network had been designed an H-plane eight horn antenna array was developed which would be attached to the feeding network output ports.

Our main design goal was to obtain as circular shape as possible for the array beam, since it was going to be the pixel of the image acquisition system.

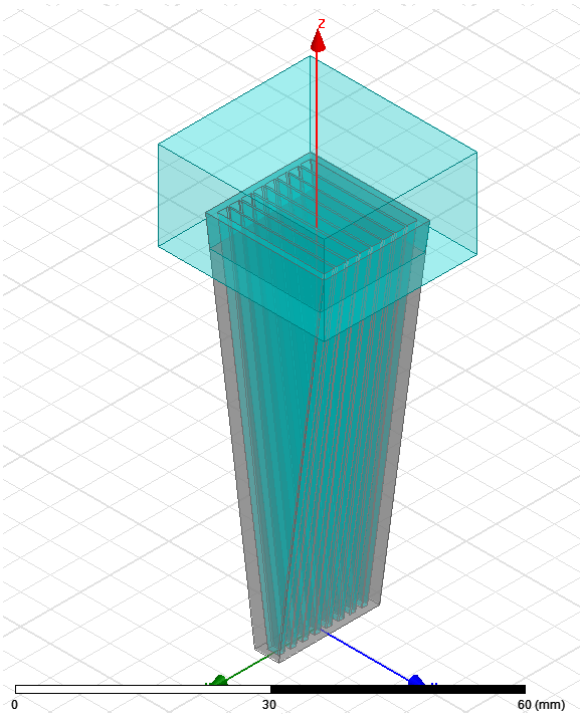

Figure 3.37 – 8-horn antenna array.

The array of pyramidal horns was designed and optimized using Ansys HFSS. Figure 3.37 shows the array structure, and in Figure 3.38 and Figure 3.39, the E-plane and H-plane radiation pattern of the

array at 90, 100 and 110 GHz is presented. All the patterns exhibit a very similar beamwidth.

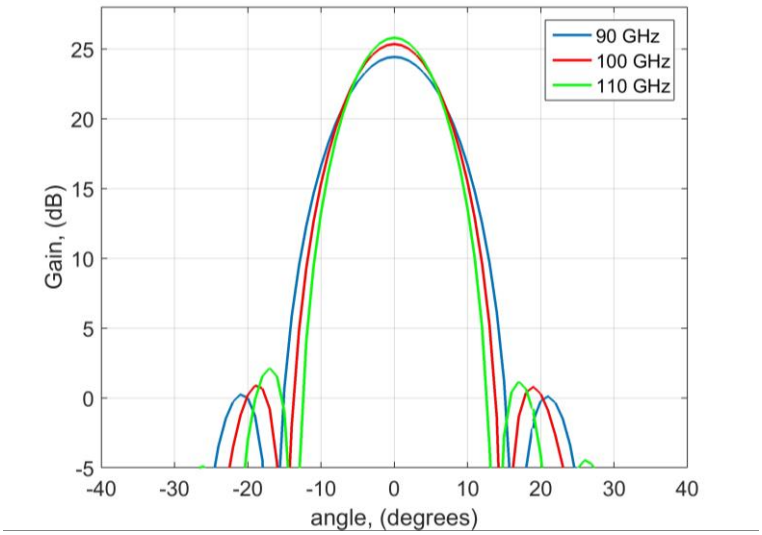

Figure 3.38 – E-plane radiation diagram of the eight horn antenna array.

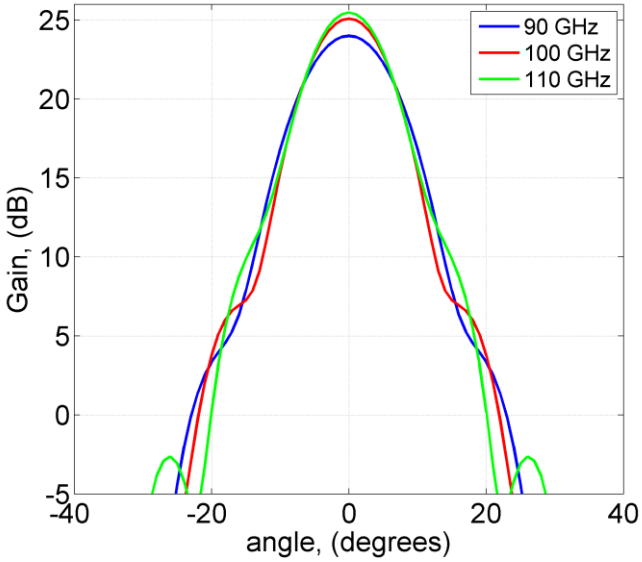

Figure 3.39– H-plane radiation diagram of the eight horn antenna array.

3.2.4 Complete structure.

3.2.4.1 Simulation.

Once the performance of the feeding network and the antenna was verified, the complete attached structure was simulated with Ansys HFSS. A schematic of the complete structure, split along the E-plane to take advantage of its symmetry to reduce computing time, can be seen in Figure 3.40.

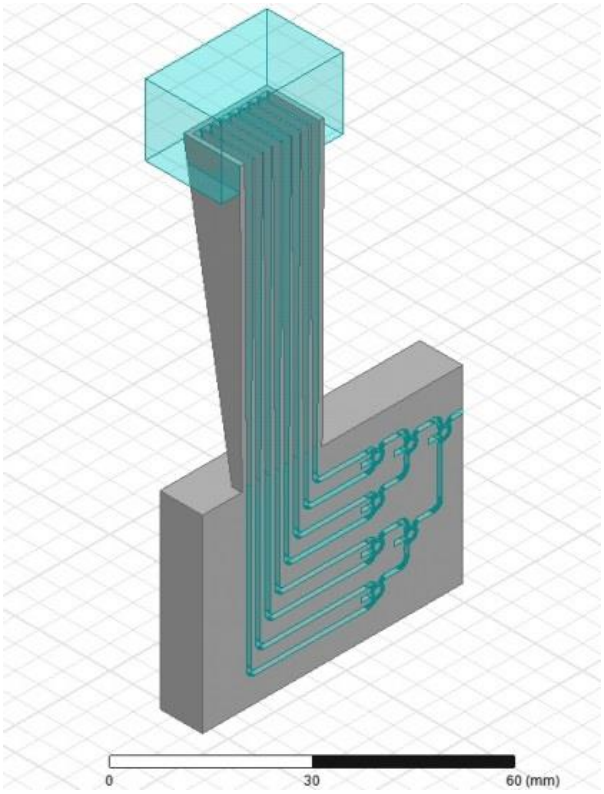

Figure 3.40 – Schematic of the overall structure split along the E-plane.

The performance of the complete system has been analysed. First the return losses have been simulated and depicted in Figure 3.41. Aluminium conductivity losses were included in the simulation

process and compared with the ideal case of a perfect electric conductor. The results are slightly different, but without significant impact in the behaviour of our system.

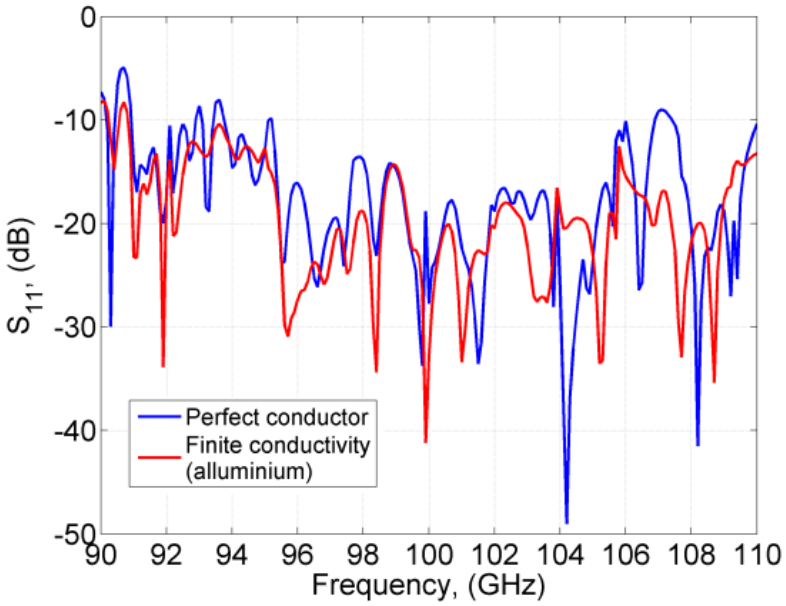

Figure 3.41 – Simulated results for the S_{11} parameter of the structure.

Finally, the simulated E-plane far field radiation pattern of the structure is presented in Figure 3.42. The main beam steering angle as a function of the frequency can be clearly observed. In the boresight direction, 25 dB of directivity are achieved at 99 GHz and scan losses of up to 3 dB are obtained at the edges of the band. High sidelobes level is observed in this simulation with values up to 20 dB.

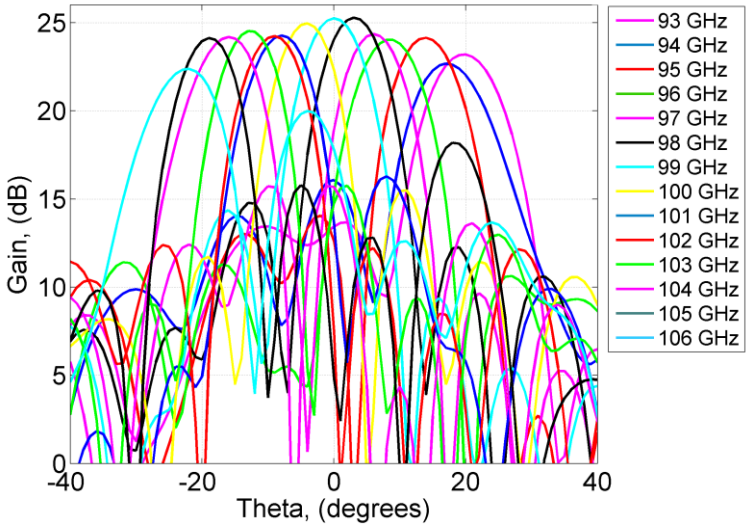

Figure 3.42 – Simulated E-plane radiation pattern of the complete structure at several frequencies.

3.2.4.2 Prototype Fabrication.

After finishing the design, the manufacture of the structure was made in aluminium. The antenna array and the feeding network were fabricated as separate pieces that can be assembled at a later stage. This gives more flexibility to the fabrication process, as the optimal manufacturing technique can be applied to each of the pieces. It also allows for future modification of each one of the pieces without affecting the other. The feeding network was fabricated in two symmetric halves split along the E-plane, and the waveguides were milled in the aluminium block using a high precision milling machine with a milling tool of 0.6 mm diameter. The H-plane horn was fabricated in a single aluminium block using wire electro discharge machining (EDM). Fabricating the array in a single piece is critical for minimizing the losses and avoiding alignment issues.

A picture of the fabricated structure is displayed in Figure 3.43. The total dimensions of the complete structure are 55 x 100 x 22 mm.

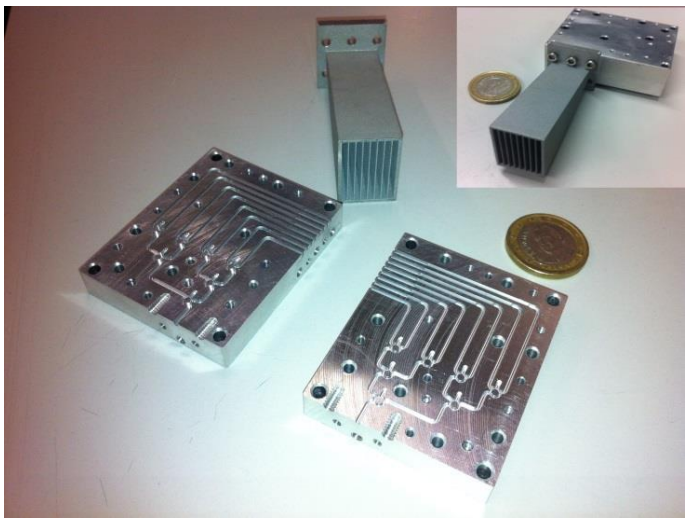

Figure 3.43 – Disassembled components of the fabricated structure.

3.2.4.3 Experimental results.

Once this frequency scanning antenna array was analysed, several measurements of the fabricated antenna prototype structure were done to confirm the agreement with the simulation results and to validate the design. The reflection coefficient, the radiation pattern and the gain measurement were characterized.

- Reflection coefficient measurement

These measurements were performed with an Agilent PNA-X N5242A network analyser equipped with two Oleson Microwave labs (OML) millimeter wave frequency extenders operating in the 90-140 GHz frequency band.

The S_{11} measurement was carried out connecting the antenna to the T/R module, calibrating with a rectangular waveguide calibration

kit and placing absorber material in the boresight direction so as to avoid the possible reflections.

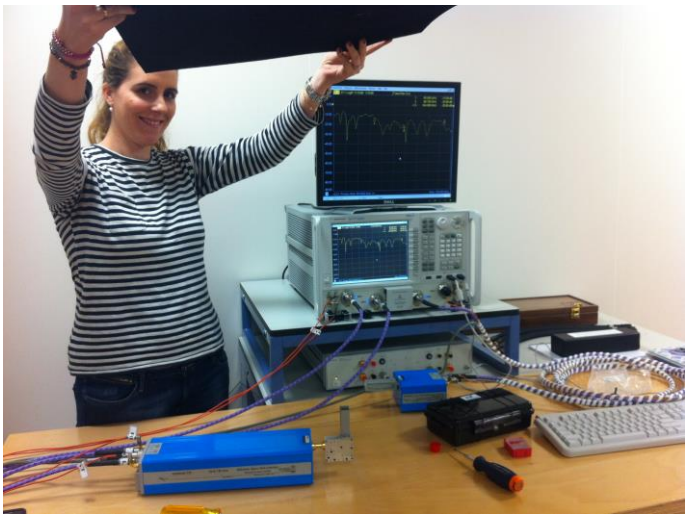

Figure 3.44 – Set-up for the reflection coefficient measurement.

The comparison between the measured and simulated S_{11} parameters is shown in Figure 3.44. A good agreement between both results can be observed. The measured S_{11} within the 94-110 GHz frequency band is under -10dB, indicating an acceptable matching. A slight frequency shift of 0.5 GHz can be observed, probably due to fabrication tolerances.

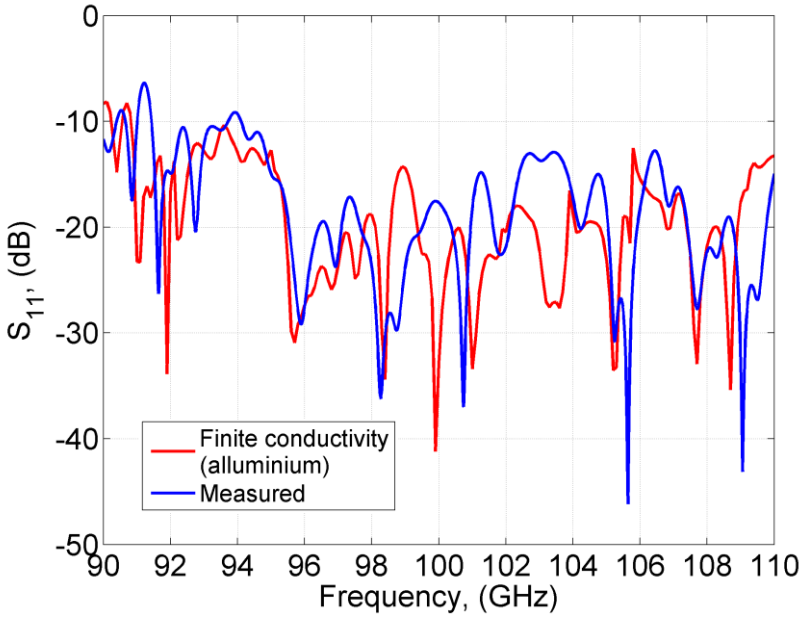

Figure 3.45 – Measured and simulated reflection coefficient parameter of the fabricated antenna.

- Radiation pattern measurement

Afterwards, the measurement of the radiation pattern was performed in near field. A near field probe was attached to the transmission module, placed 5 cm away from the antenna aperture and a 10x10 cm plane in 1 mm steps was measured. The frequency scanning antenna was placed in a 2D precision positioner. The near field pattern was acquired and a transformation to far field using an in-house Matlab code, which includes probe correction techniques [Par78], was performed.

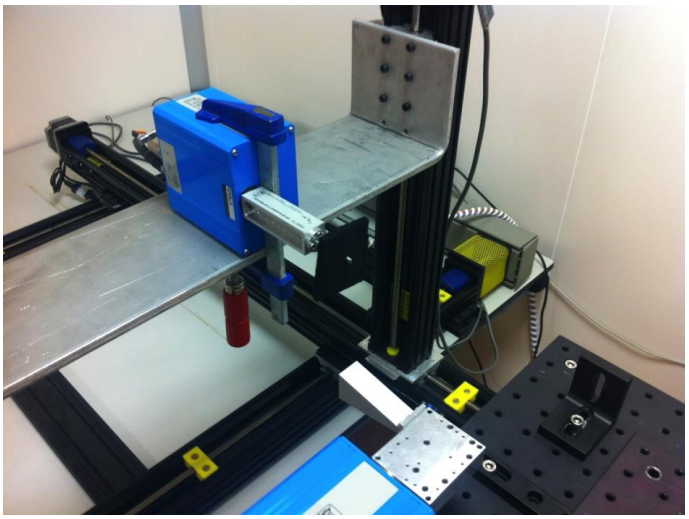

Figure 3.46 – Measurement set-up for the radiation pattern characterization.

The measured E-plane radiation pattern is depicted in Figure 3.47. The agreement with the simulated results presented in Figure 3.42 is really good. The beam pointing direction changes with frequency as derived in the simulation and the gain at the edges of the frequency band is also decreased. Note the increment of the sidelobe levels at the limit of the frequency band. This fact leads to a restriction of the usable frequency range for acquiring the image to the 96-103 GHz band, as will be explained at the next section. Outside of that band, the level of aberration introduced by the sidelobes could generate too much distortion in the image.

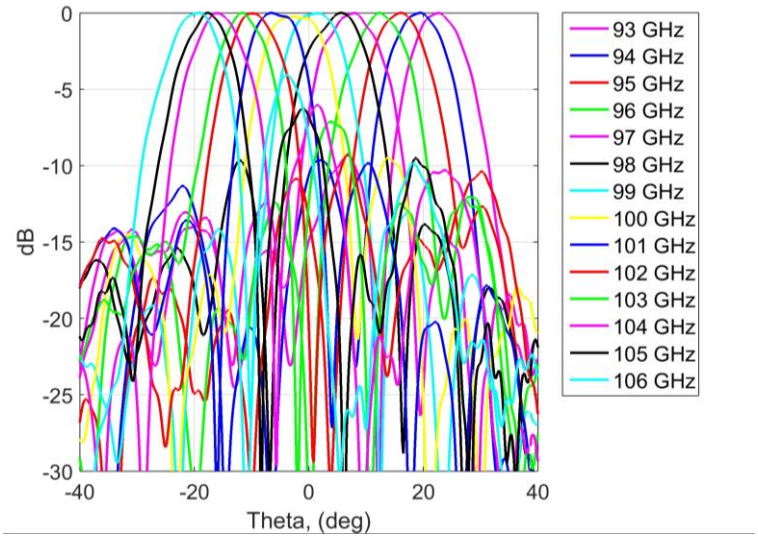

Figure 3.47 – Normalized measured E-plane radiation pattern of the fabricated antenna at several frequencies.

The normalized measured radiation pattern for H-plane is depicted in Figure 3.48; the agreement with simulated results is also good. Beam symmetry is also noticeable and the beamwidth is similar for all the frequencies.

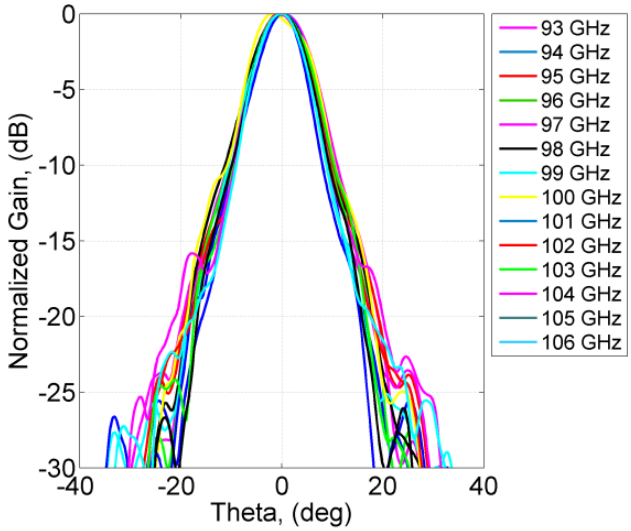

Figure 3.48 – Measured H-plane radiation diagram of the fabricated antenna.

- Far field gain measurement.

The antenna gain in the band of interest has been also measured. The gain result has been determined using the three antenna method with a calibrated gain horn antenna [Ish96].

To obtain this parameter with low error by the comparison method we have to be sure of being in the Fraunhöfer region (far field distance $R > \frac{2 \cdot D^2}{\lambda}$). Due to this fact we placed the antennas 1 meter away one from the other and we measured them, comparing the results with the ones of a calibrated-gain antenna.

First of all, the system was calibrated with a Flann microwave Ltd. standard gain horn in the 75-110 GHz band. A transition with losses below 0.1 dB from WR-8 to WR-10 was used to attach the standard gain horn. Data was saved from 90GHz to 100GHz.

After this, we measured our antenna rotating from -15º to 15º each 1º recording the frequency responses in the same band.

Figure 3.49 shows the simulated directivity and gain (gain includes metallic losses) as well as the measured gain, combining all the measurement obtained results. Good agreement between results is shown. The measured gain is approximately 1 dB below the simulated gain, probably because of additional losses in the feeding network.

Once the gain has been obtained we can introduce it to the radiation pattern results and the result gain distribution is shown in Figure 3.50.

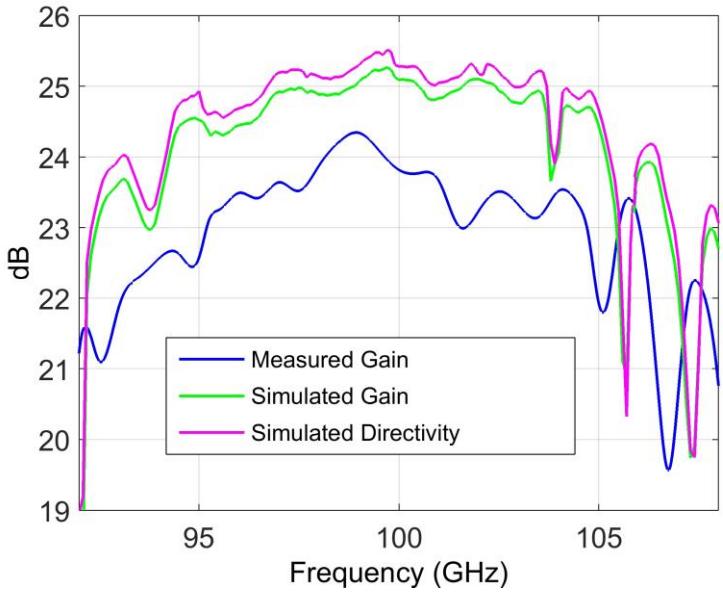

Figure 3.49 – Simulated gain and directivity and measured gain of the fabricated antenna.

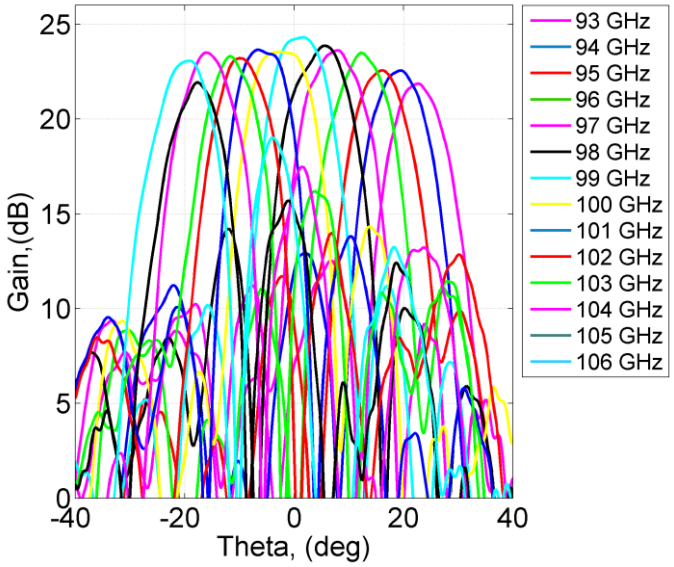

Figure 3.50 – Measured E-plane radiation pattern of the fabricated antenna at several frequencies applying the measured gain.

Furthermore, simulated and measured half-power beamwidth is depicted in Figure 3.51. A beamwidth of around 10º in the band of interest is obtained for all the cases, with very good agreement between simulation and measurements.

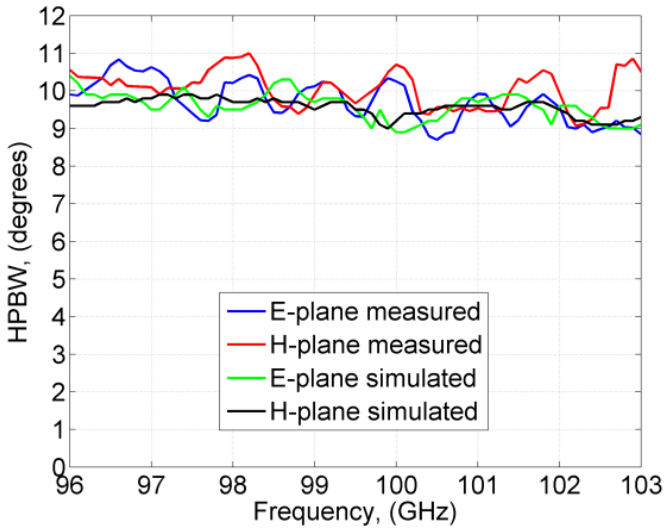

Figure 3.51 – Simulated and measured half-power beamwidth of the proposed antenna configuration.

Additionally, the 2D representations of the far field radiation pattern for several frequencies are displayed in Figure 3.52. In these plots, it can be easily observed how the main beam is scanning with frequency and the position and amplitude of sidelobes.

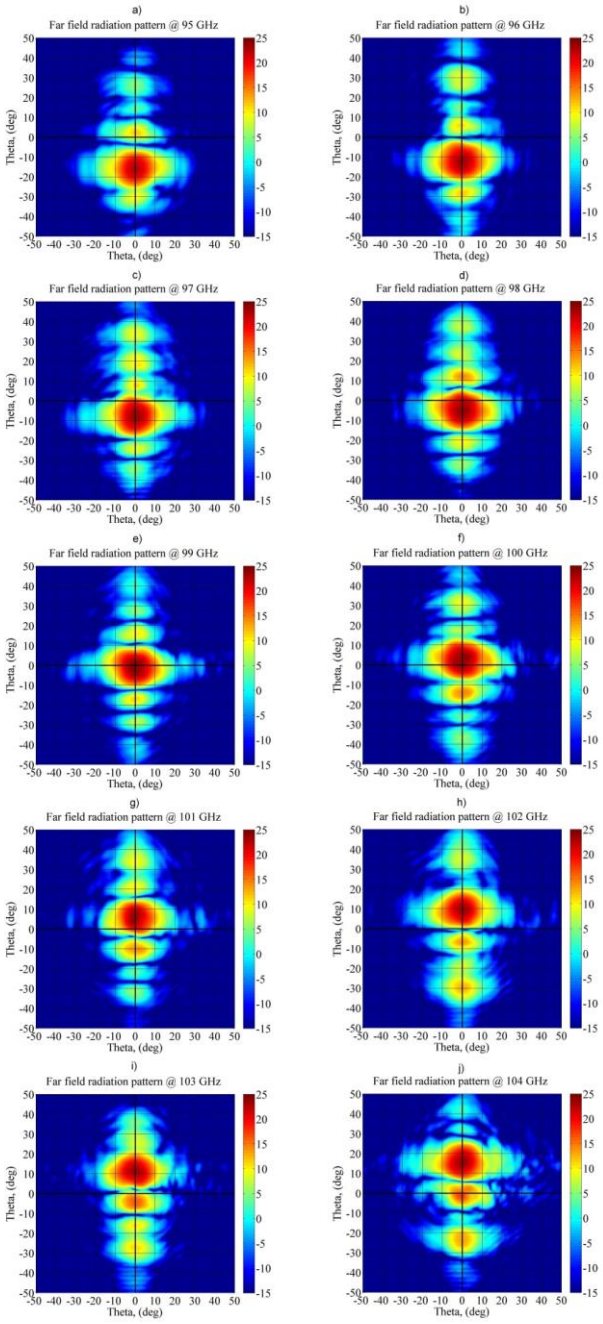

Figure 3.52 –Measured 2D radiation patterns of the fabricated antenna at frequencies from 95 to 105 GHz.

3.3 Imaging Test.

3.3.1 Proposed Image Acquisition Setup.

The fabricated frequency scanning antenna prototype was attached to the focal point of a low-cost generic satellite TV offset parabolic reflector with diameter 60 cm and f/D=0.65. The antenna orientation was chosen so that the scanning plane (E-plane) of the antenna is in the vertical axis of the paraboloid (offset-axis). A mechanical positioner was placed 2.5 meters away from the reflector, to scan the image plane in the horizontal axis. The resolution is 401 points in horizontal axis and 401 frequency points translated to the vertical axis. The image acquisition time is less than 4 min (500 ms sweep time). The setup can be seen in Figure 3.53. The alignment of the setup was quite cumbersome due to the high frequencies involved.

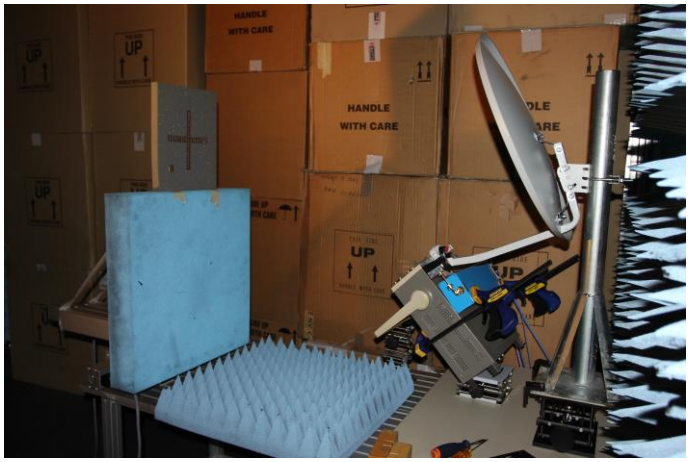

Figure 3.53 – Detail of the antenna attached to the TV parabolic reflector and mechanical positioner to move the image in horizontal axis.

The measurements were carried out using an Agilent PNA E8361C network analyser that controlled a 90-140 GHz T/R OML millimetre-

wave extension module, see Figure 3.54. The T/R module has internal X8 multipliers to transform LO and RF signals in the 10-18 GHz frequencies, supplied by the PNA, to the convenient frequency band to drive the mm-wave mixers in the case of LO signals and to propagate through the test port the required RF mm-wave signal. The OML extension module provides an output power above -4dBm and a dynamic range of 100 dB measured with 10 Hz IF bandwidth. The results are calculated by means of a bidirectional mm-wave directional coupler connected to the test port to receive both the transmitted mm-wave and the reflected mm-wave signal which are then transformed with the mixer given by the LO signal to IF frequencies and then sent back to the PNA. The PNA is programmed to record the S_{11} parameter, which will be proportional to the reflected signal from the imaging target (active operation).

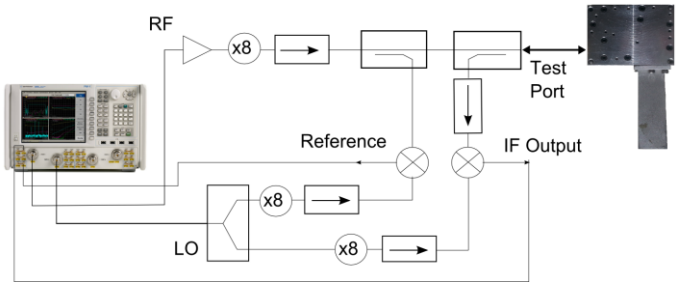

Figure 3.54 – Proposed image acquisition setup schematic.

3.3.2 Image Acquisition Setup Simulation Results.

The proposed image acquisition setup was simulated using the Ticra's GRASP reflector system simulation software [Tic08].

The TV parabolic reflector dimensions and the measured radiation patterns of the fabricated frequency scanning antenna were used as input data for GRASP software.

Figure 3.55 shows the GRASP simulated -3dB contour beams of the antenna pattern at the image plane (2.5 m away). These patterns represent the pixels of the image acquisition system. It can be seen how the pixels move in the vertical axis with frequency, scanning approximately 100mm at the image plane and the pixel is quite circular (35 mm diameter) and its size and displacement is rather constant between 97 and 101 GHz.

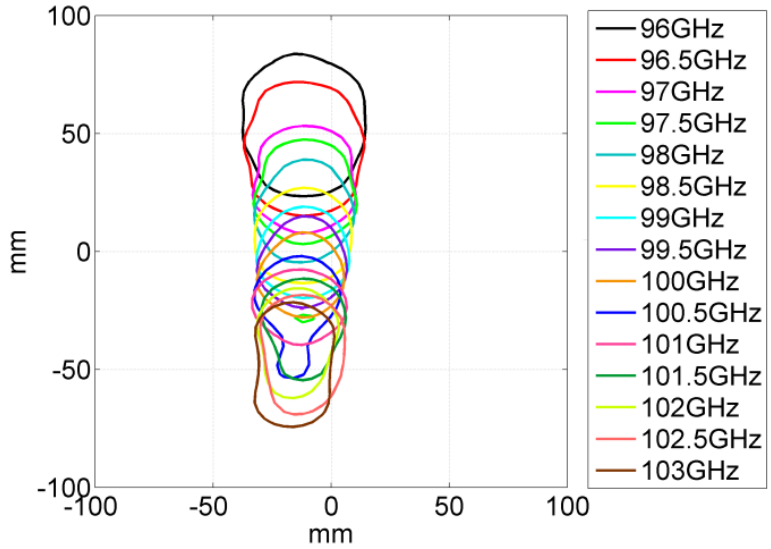

Figure 3.55 – Simulated -3 dB contour beams at the image plane, obtained with GRASP.

The antenna pattern at the image plane at 100 GHz is presented in Figure 3.56. The relatively high level of the secondary lobes, its position and shape can be observed in the figure. This result will disturb the image acquisition quality and happens similarly at all the frequencies within the usable band.

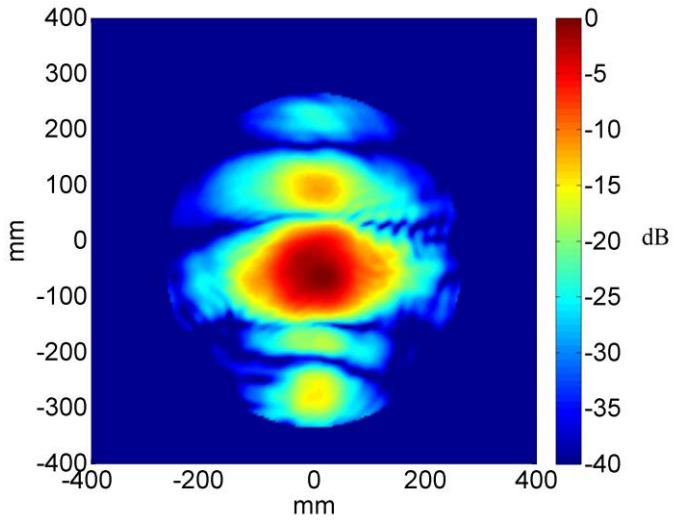

Figure 3.56 – Simulated E-field at the image plane at 100 GHz, obtained with Ticra GRASP.

3.3.3 Image Results.

As an initial test, a flat mirror surface was placed at the target position to align the setup and register the reflected value to be used as a baseline. The reflected value of such mirror placed 2.5 m away was around -35 dB lower than the reflection generated by a waveguide short connected directly to the OML extension module. This means that with around 100 dB of dynamic range on the extension header, we could have 65 dB of dynamic range with the antenna prototype at this position. However, 20 additional dB of dynamic range reduction should be taken into account, since the IF bandwidth had to be increased to make the image acquisition time faster. As a first test, a 1 € coin was used as a target. The visible image compared with the mm-wave one is plotted in Figure 3.57. A frequency-space transformation in the vertical axis (by means of GRASP simulation results to translate the frequency to position) is the only post processing performed to the acquired raw data to represent the mm-wave image.

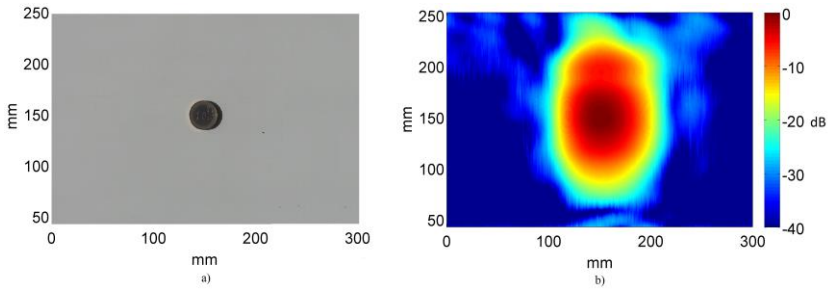

Figure 3.57 – a) Visible photo and b) mm-wave image of a 1€ coin at 2.5 m distance.

The elliptical shape of the resulting image is produced by the high sidelobe level in the E-plane (see Figure 3.50).

The second acquisition model used was a metallic cross made with drawing pins and a euro coin in one of the corners. The not planar surface of these drawing pins reflected the incident power over a broader area, making the reflected power lower than in the case of the euro coin, see Figure 3.58.

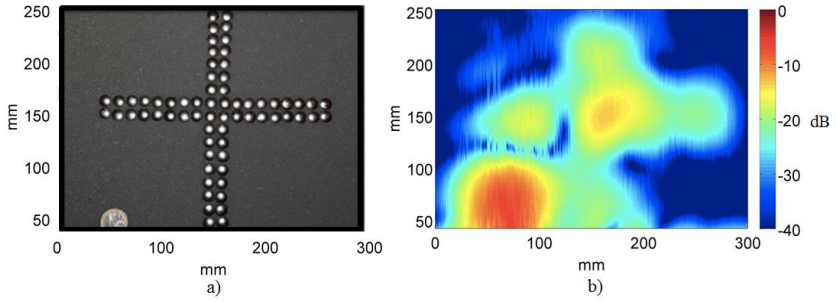

Figure 3.58 – a) Visible photo and b) mm-wave acquired image of a drawing pins cross and 1€ coin.

The quality of the acquired images is not as good as the one obtained by other mm-wave cameras because the high level of the sidelobes is affecting the results, although the cross and the coin can be clearly discerned.

These results show the validity of the concept of using a frequency scanning antenna to obtain mm-wave images in a simple and cheaper way, and using a single sensor.

3.4 Conclusions

The first mm-wave images obtained by using a frequency scanning antenna have been presented in this chapter. The designed antenna prototype implements the innovative concept of using incremental length waveguide sections to obtain the desired phase shifts at the input of the horns in a compact structure. The measured antenna results show a total scanning angle of more than 30º over a 7 GHz bandwidth with very symmetric beams, a S_{11} parameter below 10 dB, and low scan losses (less than 2 dB). The simulations and measurements have a good agreement with a difference of 1 dB between the gain values. The validity of using the proposed frequency scanning antennas for image acquisition has been demonstrated. The two presented mm-wave images have been generated using a simple experimental setup configuration, obtaining some good and promising first results. All the represented images have been generated from the raw data obtained from the network analyzer, with no postprocessing applied. Improvements in the feeding network will be made in the following chapters, to minimize the sidelobes of the frequency scanning radiation pattern, in order to get better imaging results.

3.5 References

[Alv13] Y. Álvarez, R. Camblor, C. García, J. Laviada, C. Vázquez, S. Ver-Hoeye, G. Hotopan, M. Fernández, A. Hadarig, A. Arboleya and F. Las-Heras, *"Submillimeter-Wave Frequency Scanning System for Imaging*

Applications", IEEE Transactions on Antennas and Propagation, Vol. 61, Issue:11, pp. 5689–5696, 2013.

[Ari06] S. Ariyoshi, C. Otani, A. Dobroiu, H. Shimizu, *"Superconducting Detector Array for Terahertz Imaging Applications"*, Japanese Journal of Applied Physics, Vol. 45, No. 37, 2006.

[Cam12] R. Camblor Diaz, S. Ver Hoeye, C. Vazquez, G. Hotopan, M. Fernandez and F. Las Heras, *"Sub-millimeter wave frequency scanning 8x1 antenna array"*, Progress in Electromagnetic Research, Vol. 132, 215-232, Sept. 2012.

[Cam14] R. Camblor, S. Ver Hoeye, C. Vázquez, G. Hotopan, M. Fernández, A. Hadarig and F. Las-Heras, "Sub-millimeter wave imaging system based on frequency scanning antenna", International Conference on Electromagnetics in Advanced Applications (ICEAA), , pp. 750-752, 2014.

[Che86] M.H. Chen, *"A 19-way isolated power divider via the TE10 circular waveguide mode transition"*, Microwave Symposium Digest, IEEE MTT-S, Baltimore, MD, 511-513, June 1986.

[Che10] Y. J. Cheng, W. Hong and K. Wu, *"Millimeter-Wave Half Mode Substrate Integrated Waveguide Frequency Scanning Antenna with Quadri-polarization"*, IEEE Transactions on Antennas and Propagation, Vol. 58, No. 6, June 2010.

[Coo10] K.B. Cooper, R. J. Dengler, N. Llombart, A. Tallukder, A. V. Panangadan, C. S. Peay, I. Mehdi, P. H. Siegel, *"Fast, high-resolution terahertz radar imaging at 25 meters"*, Proceedings of SPIE, Vol.7671, 2010.

[Gro09] E. N. Grossman, C. R. Dietlein, M. Leivo, A. Rautianinen and A. Luukanen, *"A Passive, Real-time, Terahertz Camera for Security*

Screening, using Superconducting Microbolometers", IEEE MTT-S International Microwave Symposium Digest, June 2009.

[Gug93] M. Guglielmi and D. R. Jackson*, "Broadside Radiation from Periodic Leaky-Wave Antennas"*, IEEE Transactions on Antennas and Propagation, Vol. 41, No. 1, Jan. 1993.

[Hfs15] (2015) Ansys HFSS 16.2 [Online]. Available: http://www.ansys.com/es_es/Productos/Flagship+Technology/ANSYS+HFSS

[Ike08] T. Ikeda, K. Sakakibara, T. Matsui and H. Hirayama, *"Beam-Scanning Performance of Leaky-Wave Slot-Array Antenna on Variable Stub-Loaded Left_Handed Waveguide"*, IEEE Transactions on Antennas and Propagation, Vol. 56, No. 12, Dec. 2008.

[Ish96] S. Ishigami, H. Iida, and T. Iwasaki, *"Measurements of complex antenna factor by the near-field 3-antenna method"*, IEEE Transactions on Electromagnetic Compatibility, Vol. 38, 424-432, Aug. 1996.

[Iwa08] T. Iwasaki, H. Kamoda, T. Derham and T. Kuki, *"A composite Right/Left-Handed Rectangular Waveguide with Tilted Corrugations for Millimeter-wave Frequency Scanning Antenna"*, Proceedings of the 38th European Microwave Conference, Oct. 2008, Amsterdam, The Netherlands.

[Kap07] B. Kapilevich, B. Litvak, M. Einat and O. Shotman, *"Passive mm-wave sensor for in-door and out-door homeland security applications"*, 2007 International Conference on Sensor.

[Li06] L. Li and K. Wu, *"Integrated planar spatial power combiner"*, IEEE Transactions of Microwave Theory and Techniques, Vol.54, 1470-1476, Jun. 2006.

[Mic12] (2015, Jan.) μWave Wizard 7.11, Mician GmbH [Online]. Available: http://www.mician.com/content/products/wave_wizard

[Par78] D. Paris, W. Leach Jr. and E. Joy, *"Basic theory of probe-compensated near-field measurements"*, IEEE Trans. Antennas and Propagation, Vol. 26, 373-379, Mayv1978.

[Tic08] Grasp 9.8. Ticra [Online]. Available: http://www.ticra.com

[Vaz10] C. Vazquez, S. Ver Hoeye, M. Fernandez, L. F. Herran and F. Las Heras, *"Frequency Scanning Probe for Microwave Imaging"*, APSURSI, July 2010.

[Wan01] K.L. Wan, Y.L. Chow and K.M. Luk, *"Simple design of dual-frequency unequal power divider"*, IEEE Electronics Letters, Vol. 37, 1171 – 1173, Sept. 2001.

[Wan11] X. Wang, Y. Jiao, Z. Weng and F. Zhang, *"Design of Leaky-Wave Antenna Based on TE10 Mode Substrate Integrated Waveguide"*, Microwave and Optical Technology Letters, Vol. 53, No.4, April 2011.

[Wei05] A. Wei, M. Lee and Q. Hu, *"Real-time, continuous-wave terahertz imaging by use of a microbolometer focal-plane array"*, Optics Letters Vol. 30, No.19, October 2005.

CHAPTER 4

FREQUENCY SCANNING ANTENNA ARRAY AT W-BAND, DESIGN AND RESULTS

4.1 Introduction

At the previous chapter, a frequency scanning array that linearly changes the phase and steers the radiation beam with the frequency for single-pixel imaging applications was designed, and the first mm-wave images acquired using a simple mirror system, were presented. One of the conclusions was that, apart from the proven feasibility of using such frequency scanning array for mm-wave imaging, the high level of the side lobes of such system presented a limitation in the resulting image quality that could be achieved by the system. In order to improve the quality, a new frequency scanning array with lower side lobe levels has been developed, analyzed and tested. Also, the system has been improved with respect to chapter 3 with an improved quality reflector and a conveyor belt to simulate a production chain environment.

Since the objective of this kind of project is to develop a low-cost real-time mm-wave imaging solution, we have selected a central frequency of 79 GHz to take advantage in future of standard commercial components (e.g., oscillators, switches, etc.) that are already available for automotive radar. It is expected that in the following years the interest on radar systems on this band will dramatically increase, and the price of the components will probably go down, making this frequency band very interesting for the development of low cost imaging systems. However, since the focus of this work is the optimized antenna and the associated system comprising the reflector, conveyor belt and real-time postprocessing, a vector network analyzer has been used to test the system.

The main contribution of this paper is a system capable of sweeping a pixel line, process the raw data, and display it to the user, in real time, proving the feasibility of using single-pixel frequency scanning arrays for conveyor belt applications. Special attention has been paid to reduce the side lobe level by windowing the field at the aperture and to mitigate the radiation pattern distortion by postprocessing techniques. Moreover, the system relies on cost-effective components so the overall cost is reduced if compared with conventional mechanical or electronical conventional beam steering strategies at this frequency band.

4.2 Frequency scanning system

The feeding network of the frequency scanning array antenna presented in the previous chapter, was designed to generate the same amplitude in all its output ports, connected to the array elements. As a result of this, the theoretical sidelobe level was 13 dB below the main lobe level, at the central frequency (Fourier transform of a rectangular amplitude distribution). The sidelobe level was even higher at the extreme frequencies, due to the beam scanning effect, that decreases the main lobe level as a result of the misalignment between the main lobe of the array factor and the main lobe of the radiation pattern of the unit elements of the antenna array.

In order to obtain lower side lobe levels, the most common solution consists in windowing the amplitudes of the array elements, modifying the array factor, which will be no longer a sinc function with sidelobe levels of 13 dB. Windowing the amplitudes introduces an interesting trade-off between sidelobe level, and directivity of the main beam. This can be explained since the amplitude windowing

"narrows" the amplitude distribution, "widening" the corresponding Fourier transform that results in the far field distribution. For that reason, a careful analysis of several amplitude windows has been made, in order to determine the best option for the current imaging application.

Since the far field radiation pattern of a certain current distribution is closely related to the Fourier transform of that distribution, it will be interesting to analyze the Fourier transforms of several amplitude windows. Since the result of applying a window to the amplitude distribution is the product of the amplitude by the distribution, the resulting Fourier transform can be interpreted as the convolution of the Fourier transforms of the window and the distribution. If the sidelobe level of the unitary antennas of the array is low enough, the main lobe will be dominant in the convolution, and the sidelobe level and main lobe width of the window Fourier transform will give a very good sign of the effect of applying that particular window. For that reason, the comparison between the Fourier transform of a window and that of a rectangular window (which corresponds to applying no window to a finite amplitude distribution), will be very interesting to determine the best window to apply.

Several well-known windows have been taken into consideration for the array elements amplitude distribution:

- Bartlett Window

$$W(n) = 1 - \left| \frac{n - \frac{N-1}{2}}{\frac{N-1}{2}} \right| \quad (4.1)$$

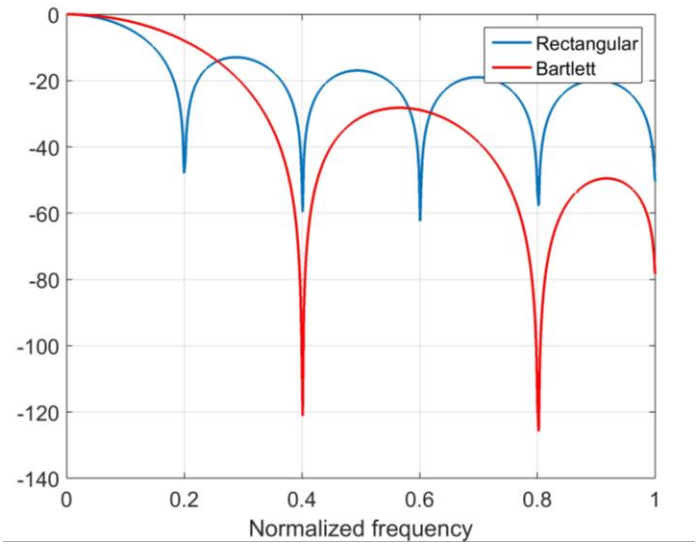

Figure 4.1 – Comparison between rectangular and Bartlett windows Fourier transforms.

- Bartlett-Hann Window

$$W(n) = a_0 - a_1\left|\frac{n}{N-1} - \frac{1}{2}\right| - a_2\cos\left(\frac{2\pi n}{N-1}\right) \quad (4.2)$$

a_0=0.62 a_1=0.48 a_2=0.38

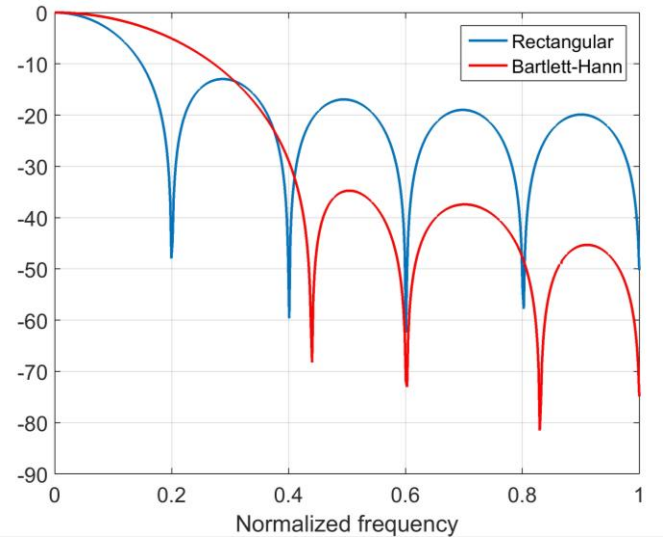

Figure 4.2 – Comparison between rectangular and Bartlett-Hann windows Fourier transforms.

- Blackman Window

$$W(n) = a_0 - a_1 \cos\left(\frac{2\pi n}{N-1}\right) + a_2 \cos\left(\frac{4\pi n}{N-1}\right) \quad (4.3)$$

a_0=0.42659 a_1=0.49656 a_2=0.076849

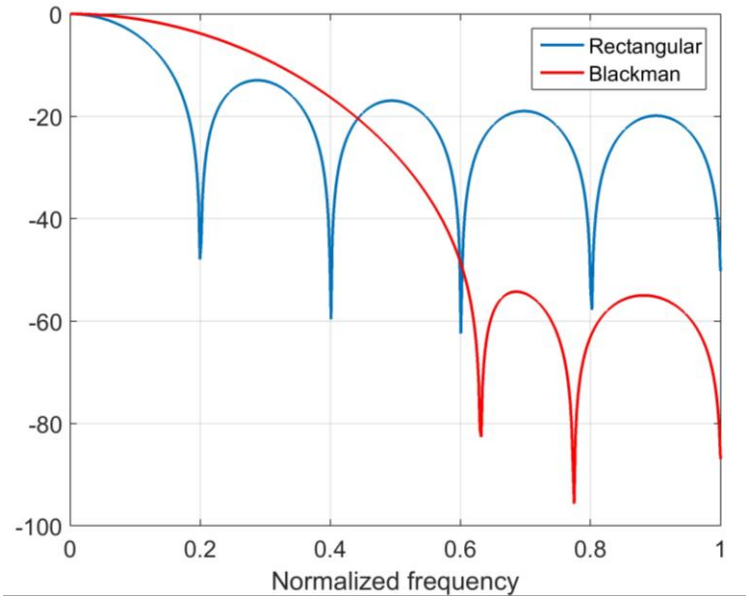

Figure 4.3 – Comparison between rectangular and Blackman windows Fourier transforms.

- Blackman-Harris Window

$$W(n) = a_0 - a_1 \cos\left(\frac{2\pi n}{N-1}\right) + a_2 \cos\left(\frac{4\pi n}{N-1}\right) - a_3 \cos\left(\frac{6\pi n}{N-1}\right) \quad (4.4)$$

a_0=0.358775 a_1=0.48829 a_2=0.14128 a_3=0.01168

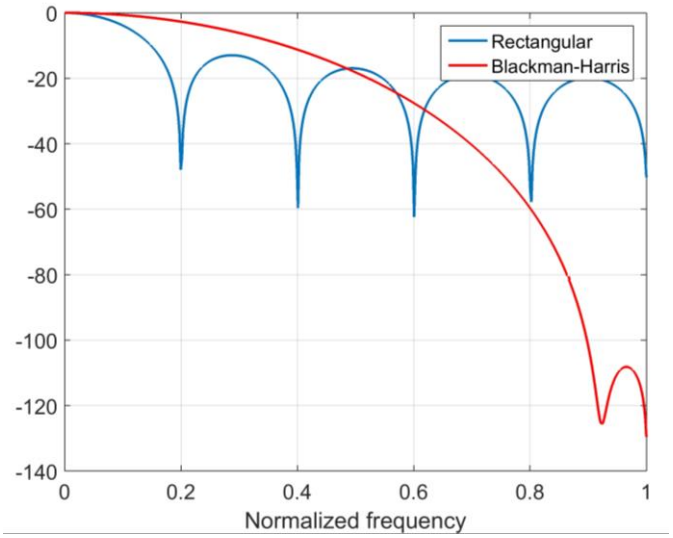

Figure 4.4 – Comparison between rectangular and Blackman-Harris windows Fourier transforms.

- Blackman-Nuttall Window

$$W(n) = a_0 - a_1 \cos\left(\frac{2\pi n}{N-1}\right) + a_2 \cos\left(\frac{4\pi n}{N-1}\right) - a_3 \cos\left(\frac{6\pi n}{N-1}\right) \quad (4.5)$$

a_0=0.3635819 a_1=0.4891775 a_2=0.1365995 a_3=0.0106411

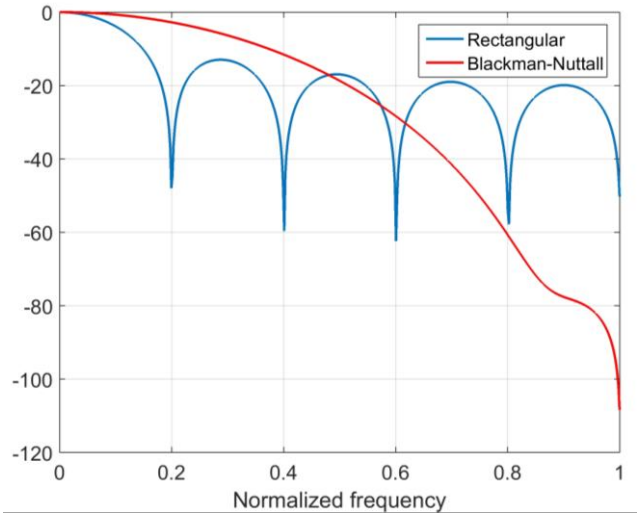

Figure 4.5 – Comparison between rectangular and Blackman-Nuttall windows Fourier transforms.

- Cosine Window

$$W(n) = \cos\left(\frac{\pi n}{N-1} - \frac{\pi}{2}\right) = \sin\left(\frac{\pi n}{N-1}\right) \quad (4.6)$$

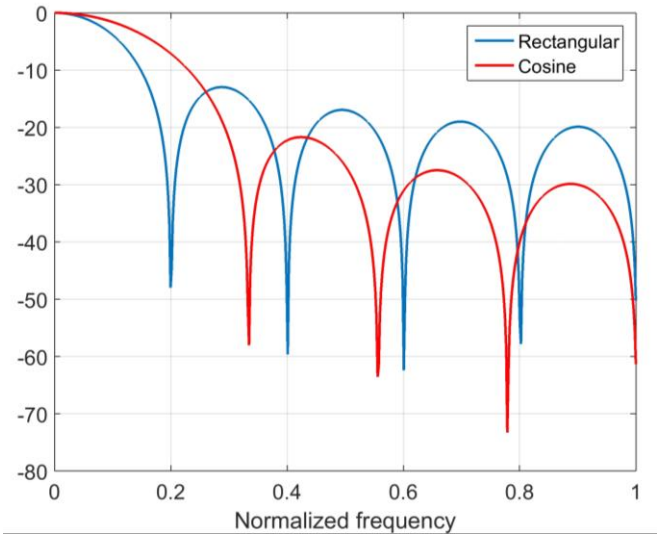

Figure 4.6 – Comparison between rectangular and Cosine windows Fourier transforms.

- Flat-top Window

$$W(n) = a_0 - a_1 \cos\left(\frac{2\pi n}{N-1}\right) + a_2 \cos\left(\frac{4\pi n}{N-1}\right) - a_3 \cos\left(\frac{6\pi n}{N-1}\right) + a_4 \cos\left(\frac{8\pi n}{N-1}\right) \quad (4.7)$$

a_0=1 a_1=1.93 a_2=1.29 a_3=0.38 a_4=0.028

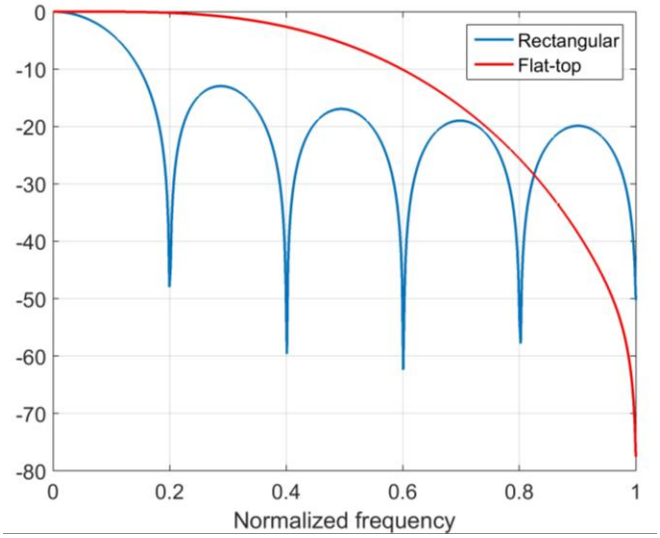

Figure 4.7 – Comparison between rectangular and Flat-top windows Fourier transforms.

- Gaussian Window

$$W(n) = e^{-\frac{1}{2}\left(\frac{n-\frac{N-1}{2}}{\frac{\sigma(N-1)}{2}}\right)^2} \quad (4.8)$$

σ ≤0.5

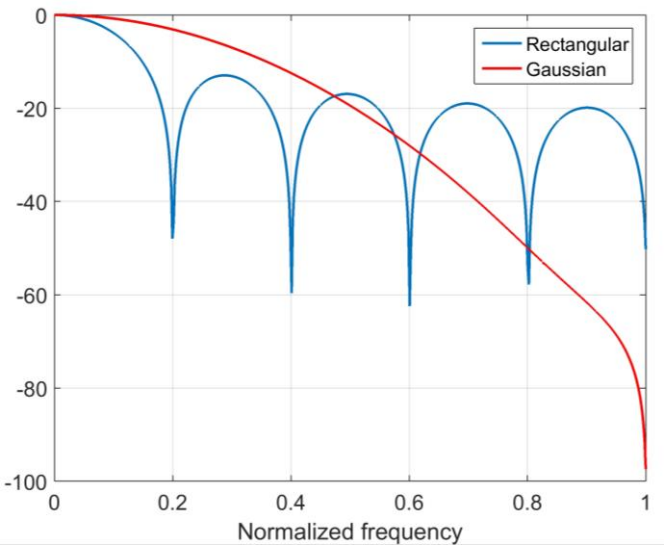

Figure 4.8 – Comparison between rectangular and Gaussian windows Fourier transforms.

- Hamming Window

$$W(n) = \alpha - \beta \cos\left(\frac{2\pi n}{N-1}\right) \quad (4.9)$$

with α=0.54 and β=1- α=0.46

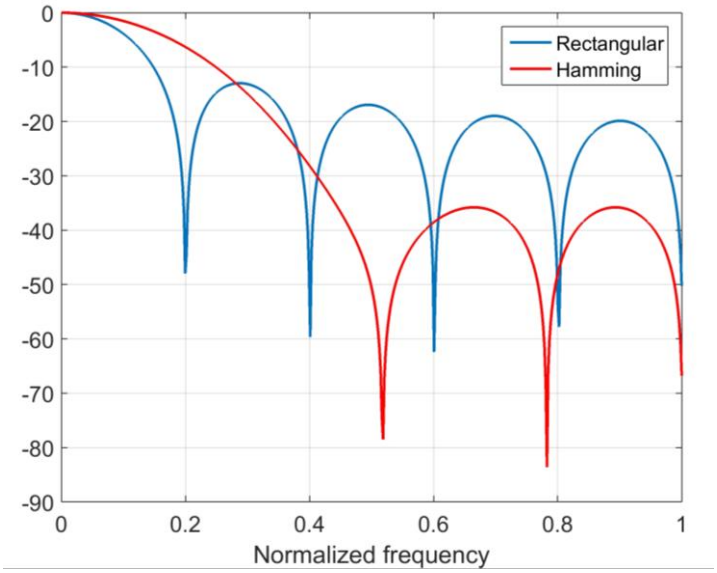

Figure 4.9 – Comparison between rectangular and Hamming windows Fourier transforms.

- Hanning Window

$$W(n) = 0.5\left(1 - \cos\left(\frac{2\pi n}{N-1}\right)\right) \quad (4.10)$$

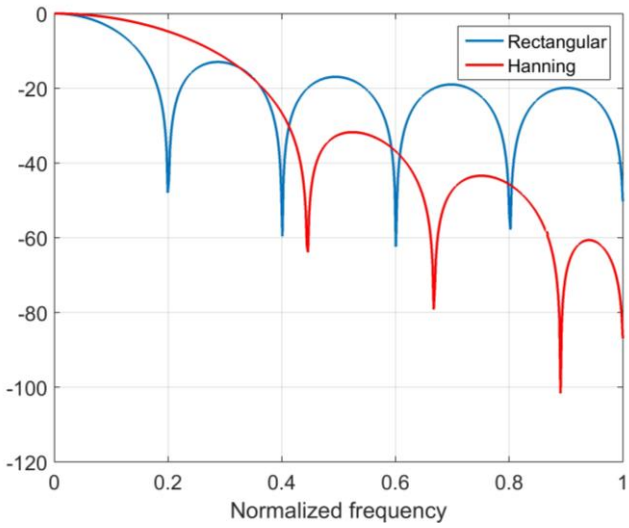

Figure 4.10 – Comparison between rectangular and Hanning windows Fourier transforms.

- Hann-Poisson Window

$$W(n) = \frac{1}{2}\left(1 - \cos\left(\frac{2\pi n}{N-1}\right)\right) e^{\frac{-\alpha|N-1-2n|}{N-1}} \quad (4.11)$$

α: parameter that controls the slope of the exponential.

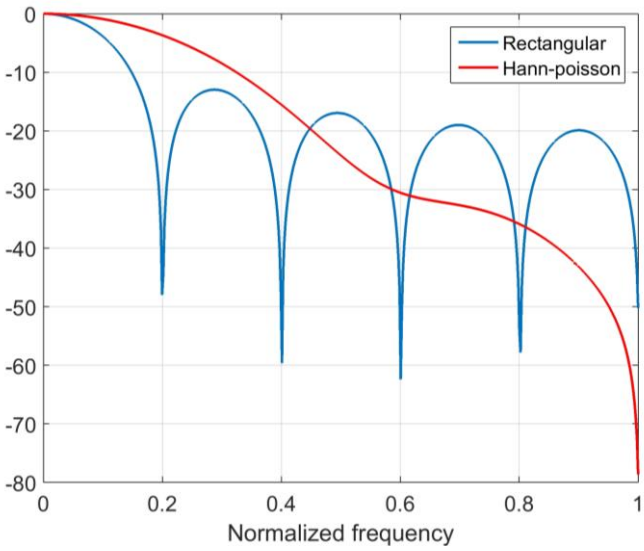

Figure 4.11 – Comparison between rectangular and Hann-poisson windows Fourier transforms.

- Lanczos Window

$$W(n) = sinc\left(\frac{2n}{N-1} - 1\right) \quad (4.12)$$

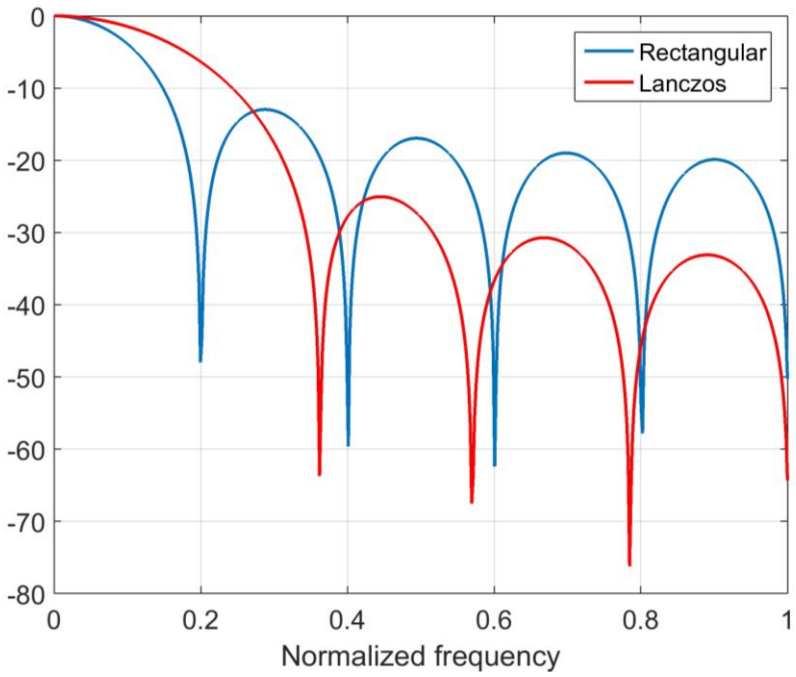

Figure 4.12 – Comparison between rectangular and Lanczos windows Fourier transforms.

- Nuttall Window

$$W(n) = a_0 - a_1 \cos\left(\frac{2\pi n}{N-1}\right) + a_2 \cos\left(\frac{4\pi n}{N-1}\right) - a_3 \cos\left(\frac{6\pi n}{N-1}\right) \quad (4.13)$$

a_0=0.355768 a_1=0.487396 a_2=0.144232 a_3=0.012604

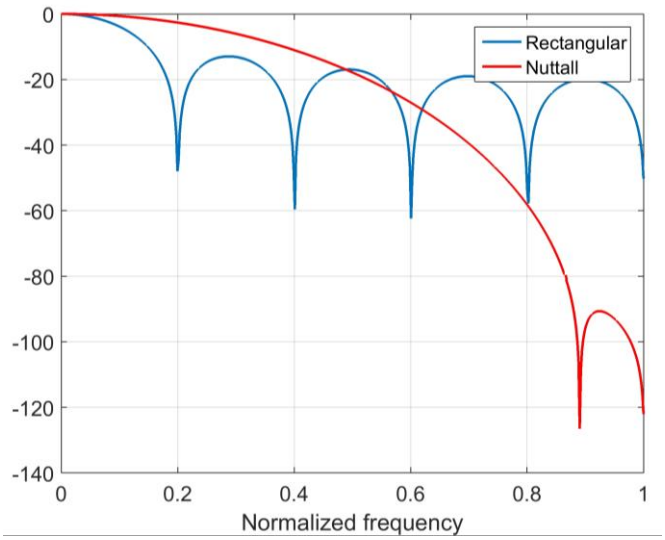

Figure 4.13 – Comparison between rectangular and Nuttall windows Fourier transforms.

- Poisson Window

$$W(n) = e^{-\left|n-\frac{N-1}{2}\right|\frac{1}{\tau}} \quad (4.14)$$

$$\tau = \frac{N}{2}\frac{8.69}{D} \quad (4.15)$$

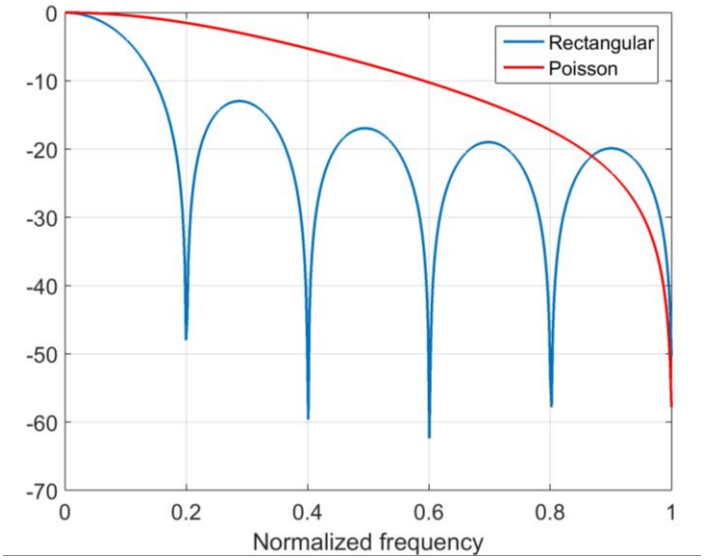

Figure 4.14 – Comparison between rectangular and Poisson windows Fourier transforms.

- Triangular Window

$$W(n) = 1 - \left| \frac{n - \frac{N-1}{2}}{\frac{N+1}{2}} \right| \quad (4.16)$$

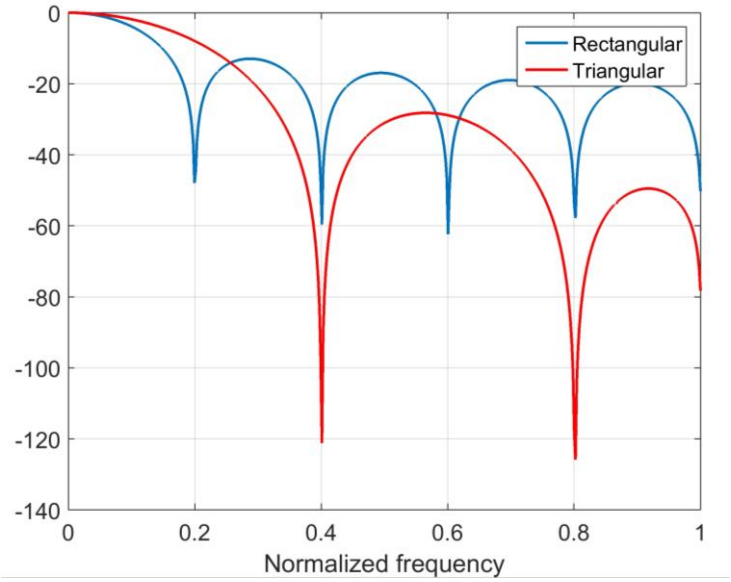

Figure 4.15 – Comparison between rectangular and Triangular windows Fourier transforms.

- Welch Window

$$W(n) = 1 - \left(\frac{n - \frac{N-1}{2}}{\frac{N+1}{2}} \right)^2 \quad (4.17)$$

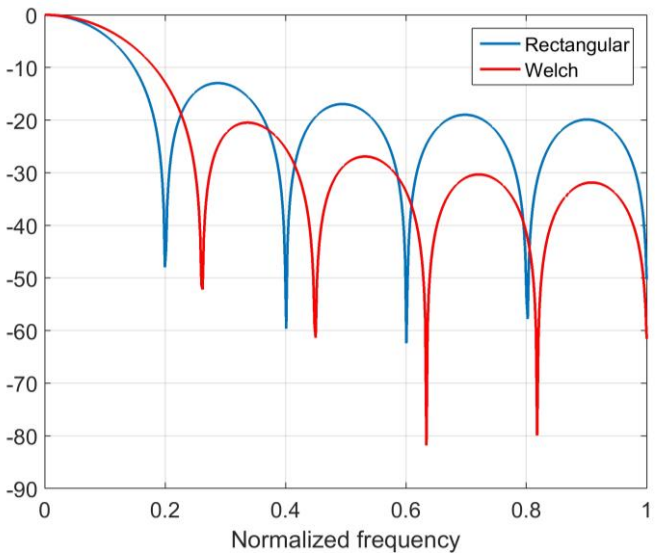

Figure 4.16 – Comparison between rectangular and Welch windows Fourier transforms.

Table 4.1 contains the relative amplitudes with respect to the maximum that the feeding network should provide at the output ports, for the previously presented window functions.

Table 4.1 – Relative amplitudes for each port employing different windows.

Port Number	1	2	3	4	5	6	7	8
Bartlett Window	0.222	0.444	0.667	0.889	0.889	0.667	0.444	0.222
Bartlett-Hann Window	0.142	0.421	0.667	0.889	0.889	0.667	0.421	0.142
Blackman	0.059	0.268	0.636	0.952	0.952	0.636	0.268	0.059

Blackman-Harris Window	0.015	0.147	0.521	0.932	0.932	0.521	0.147	0.015
Blackman-Nuttall Window	0.018	0.156	0.529	0.933	0.933	0.529	0.156	0.018
Cosine Window	0.342	0.643	0.866	0.985	0.985	0.866	0.643	0.342
Flat top Window	-0.087	-0.332	0.912	4.007	4.007	0.912	-0.332	-0.087
Gaussian Window σ=0.5	0.298	0.539	0.801	0.976	0.976	0.801	0.539	0.298
Gaussian Window σ =0.4	0.151	0.381	0.707	0.962	0.962	0.707	0.381	0.151
Gaussian Window σ =0.3	0.035	0.18	0.539	0.934	0.934	0.539	0.18	0.035
Gaussian Window σ =0.2	0	0.021	0.249	0.857	0.857	0.249	0.021	0
Hamming Window	0.188	0.46	0.77	0.972	0.972	0.77	0.46	0.188
Hanning Window	0.117	0.413	0.75	0.97	0.97	0.75	0.413	0.117
Hann-Poisson Window α=1	0.054	0.237	0.537	0.868	0.868	0.537	0.237	0.054

Hann-Poisson Window α=2	0.025	0.136	0.385	0.777	0.777	0.385	0.136	0.025
Lanczos	0.263	0.564	0.827	0.98	0.98	0.827	0.564	0.263
Nuttall	0.014	0.142	0.515	0.931	0.931	0.515	0.142	0.014
Poisson Window	0.005	0.0216	0.100	0.464	0.464	0.100	0.022	0.005
Triangular Window	0.364	0.545	0.727	0.909	0.909	0.727	0.545	0.364
Welch Window	0.595	0.793	0.926	0.992	0.992	0.926	0.793	0.595

Table 4.2 –-3 dB beamwidth and first side lobe level for each window.

Window	Increase in -3 dB beamwidth with respect to rectangular window (%)	First side lobe level (dB)
Bartlett	42.02	-28.2
Bartlett-Hann	75.28	-34.75
Blackman	100	-54.27
Blackman-Harris	135.96	-108.17
Blackman-Nuttall	133.71	n/a
Cosine	51.46	-21.7
Flat-top	366.29	n/a
Gaussian	120.67	n/a
Hamming	56.52	-35.81
Hanning	79.78	-31.75
Hann-Poisson	103.6	n/a

Lanczos	58.65	-25.04
Nuttall	138.2	-90.67
Poisson	225.84	n/a
Triangular	41.57	-28.2
Welch	19.89	-20.5

The directivity radiation pattern of an eight horn antenna array with the same amplitude at the eight ports (rectangular window) or with the amplitude tapered with the previously analyzed windows can be observed in Fig. 4.17. Note that to better observe the directivity reduction effect of the windows, the directivity values have been normalized to the maximum directivity of the rectangular window case.

A more exhaustive study of these different 16 options has been accomplished with the complete structure, and the 3 windows considered to be more suitable for our application, have been analysed with the complete structure. This three windows are the Hanning window, Blackman Window and Gaussian Window with σ=0.3.

In order to obtain the desired amplitude at the output ports of the network, asymmetrical power divider rectangular waveguide elements have been designed. The necessary amplitudes at the output ports of the feeding network have been previously presented in Table 4.1. Uneven T-junctions have been developed varying the width and the length of the junction output branches. This particular asymmetrical power divider [Gru06, Jai14, Zul13] configuration has been chosen due to its easiness of fabrication with standard milling processes, and its good performance.

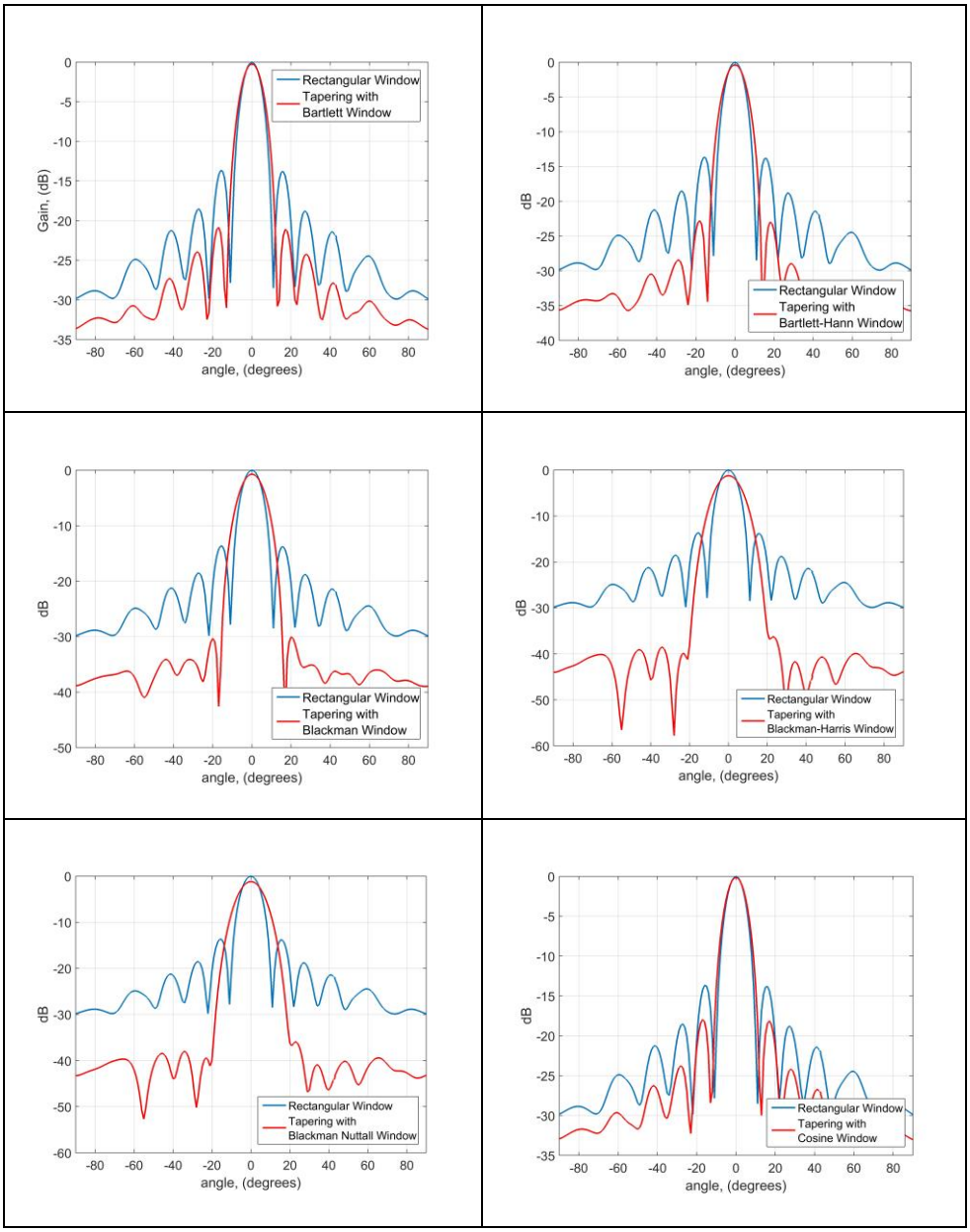
Rectangular Window
Tapering with Bartlett Window
Gain, (dB)
angle, (degrees)
Rectangular Window
Tapering with Bartlett-Hann Window
dB
angle, (degrees)
Rectangular Window
Tapering with Blackman Window
dB
angle, (degrees)
Rectangular Window
Tapering with Blackman-Harris Window
dB
angle, (degrees)
Rectangular Window
Tapering with Blackman Nuttall Window
dB
angle, (degrees)
Rectangular Window
Tapering with Cosine Window
dB
angle, (degrees)

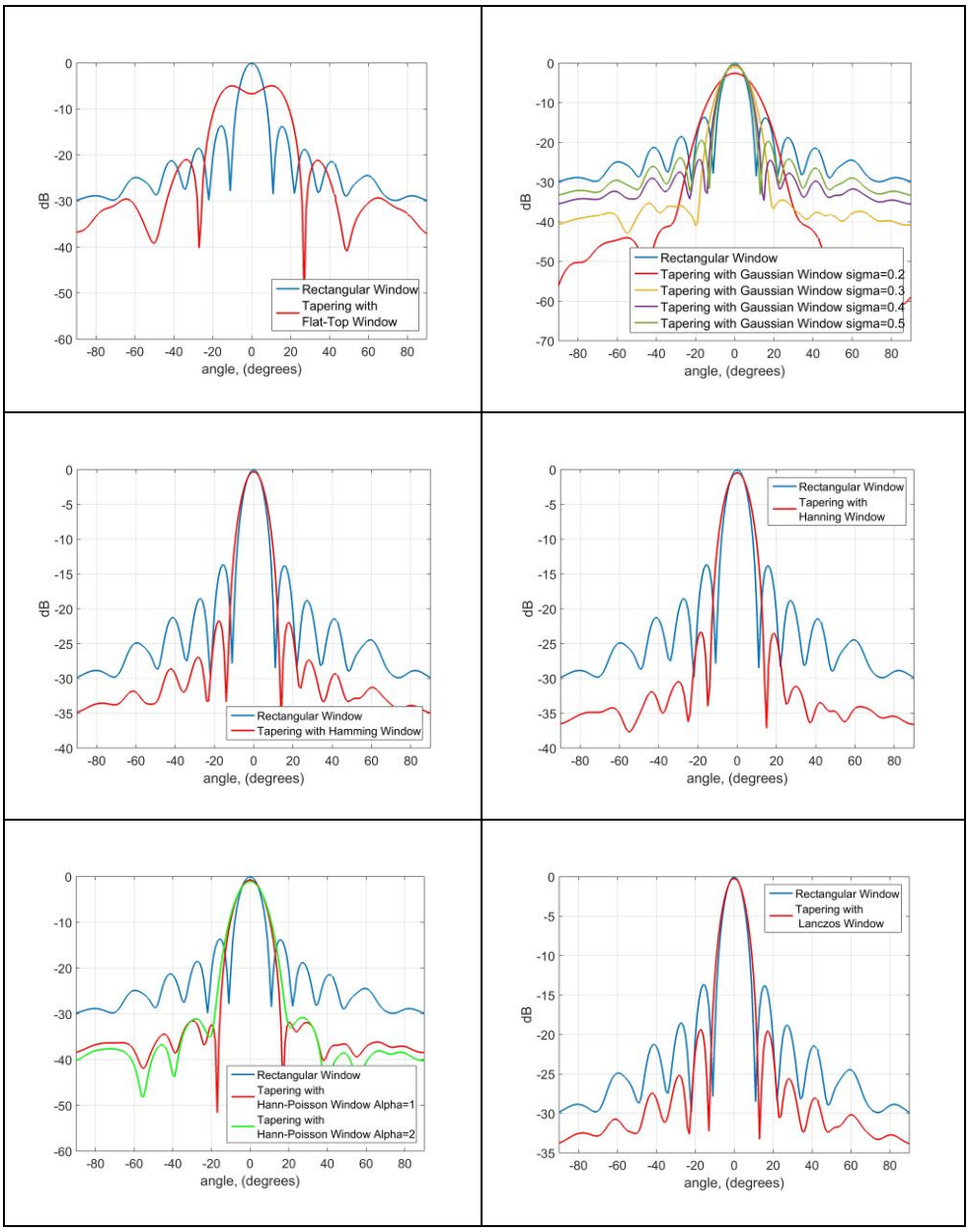
dB
angle, (degrees)
Rectangular Window
Tapering with
Flat-Top Window
Rectangular Window
Tapering with Gaussian Window sigma=0.2
Tapering with Gaussian Window sigma=0.3
Tapering with Gaussian Window sigma=0.4
Tapering with Gaussian Window sigma=0.5
Rectangular Window
Tapering with Hamming Window
Rectangular Window
Tapering with
Hanning Window
Rectangular Window
Tapering with
Hann-Poisson Window Alpha=1
Tapering with
Hann-Poisson Window Alpha=2
Rectangular Window
Tapering with
Lanczos Window

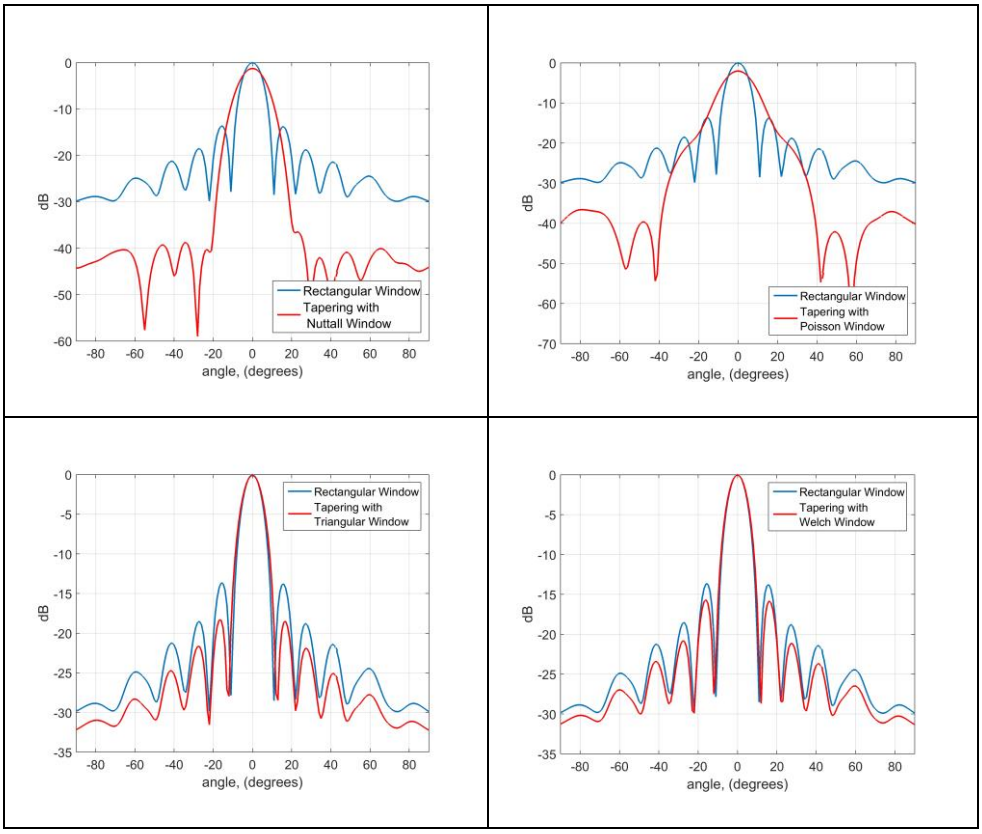

Figure 4.17 – Radiation pattern of an eight-horned antenna with the same amplitude at the eight ports or with tapering.

Due to the symmetry of the windowed amplitude distribution, only 4 different junctions are necessary to obtain the desired power levels at the output ports.

Figure 4.18 shows the layout of the feeding network structure with the different power divider types that will be analyzed in the next sections.

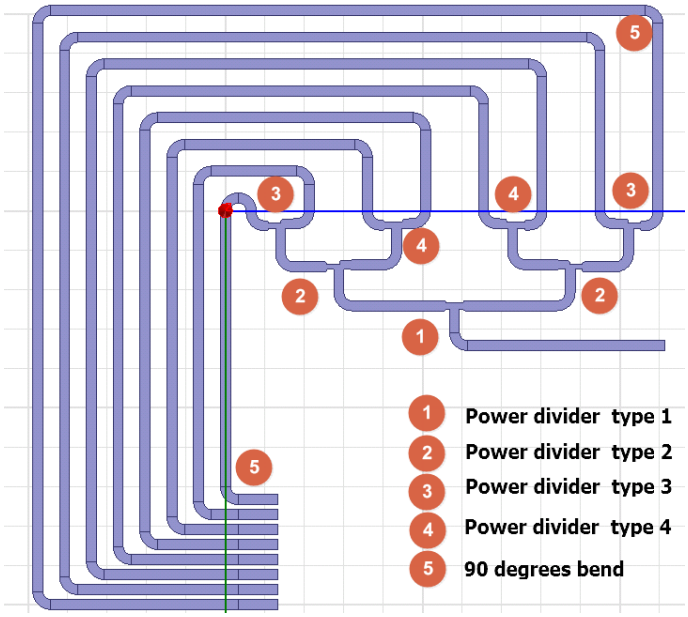

Figure 4.18 – Complete layout of the feeding network for the 8-horn antenna.

The feeding network is composed of sections of WR-10 waveguides (2.54x1.27 mm). The power dividers have been designed to have the desired output amplitude in each one of the output ports. The imbalance caused by conductor losses between the longest and the shortest paths is estimated in simulations employing a conductivity for the aluminium of $3.8 \cdot 10^7$ S/m to be less than 0.63 dB, not being an issue to the performance of the feeding network.

Even Power Divider

The even power divider splits the power by half. It is the same for all configurations. Once it has been optimized so as to be integrated in the complete structure, sections of straight waveguide have been added. For the complete structure it is called Power Divider 1, see Figs. 4.18 and 4.19.

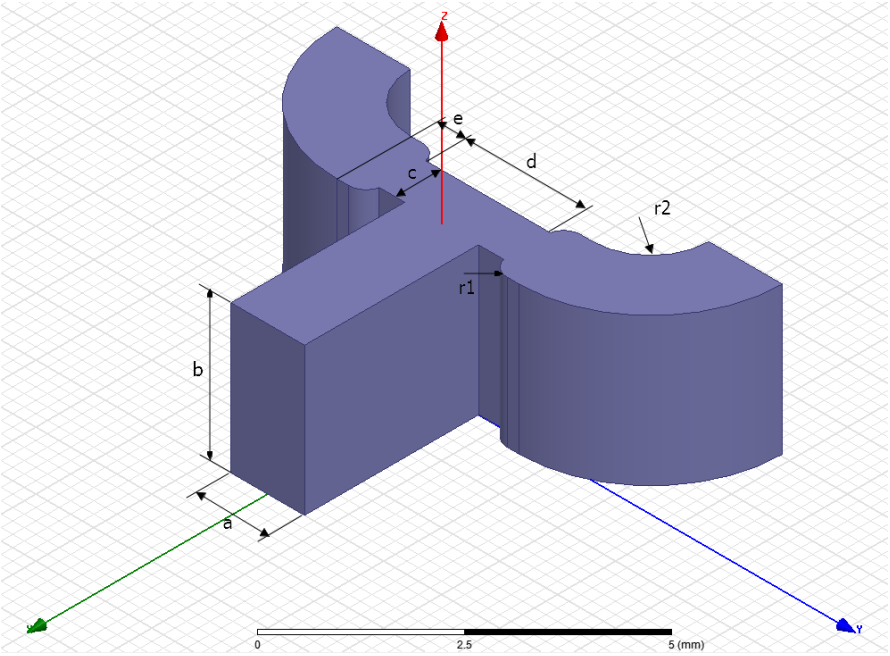

Figure 4.19 –Rectangular waveguide even power divider structure with the dimensional parameters that define the component.

Table 4.3 – Parameters for the even power divider.

Parameter	a	b	c	d	e	r1	r2
mm	1.27	2.54	0.8	2.15	0.5	0.3	1

Uneven Power Divider

The other three power dividers are no longer even so a different structure has been designed. The element is the same for all three types of power divider, and only certain dimensional parameters that control the resulting power split ratio are changed. The value of these dimensional parameters, for achieving the different amplitudes required by each window, are presented in the following tables, for each power splitter type.

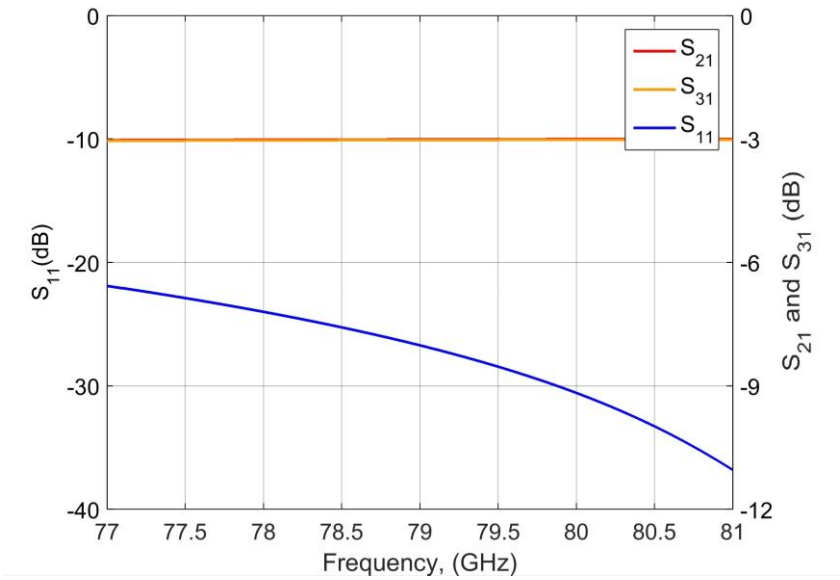

Figure 4.20 –S-parameters simulation for the 50-50 (even) power divider.

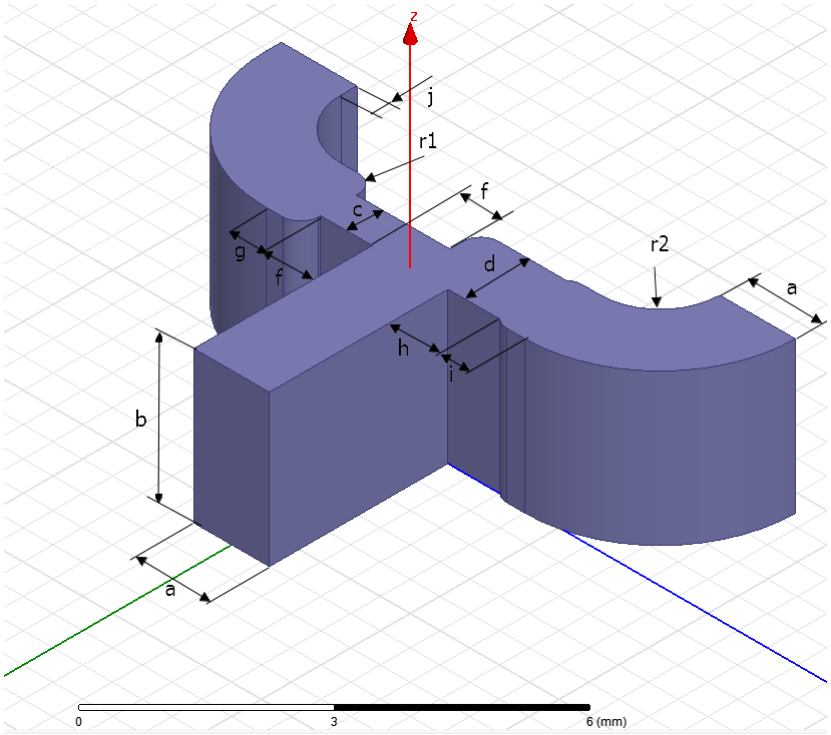

Figure 4.21 – Rectangular waveguide uneven power divider structure with the dimensional parameters that define the component.

Blackman Window

Power divider type 2

For the Blackman window, the split ratio of the type 2 power divider should be of -7.68dB and -0.81dB for the S_{21} and S_{31} parameters, respectively. The dimensional parameters required to achieve this splitting ratio are shown in table 4.4.

Table 4.4 – Parameters for the Blackman Window power divider 2 in mm.

a	b	c	d	e	f	g	h	i	j	r1	r2
1.27	2.54	0.5	1.1	0.59	0.87	0.58	0.87	0.5	0.3	0.3	1

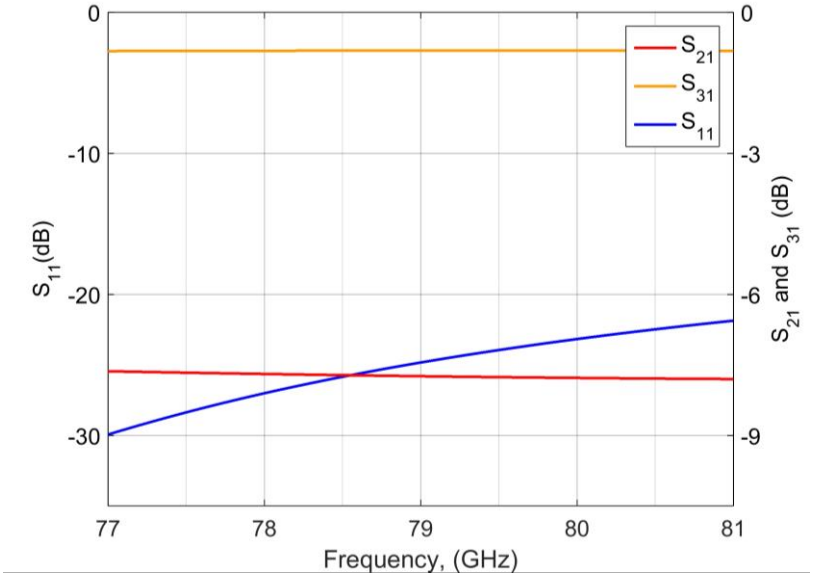

Figure 4.22 –S-parameters simulation for Blackman power divider 2.

Power divider type 3

For the Blackman window, the split ratio of the type 3 power divider should be of -7.44 dB and -0.86 dB for the S_{21} and S_{31}

parameters, respectively. The dimensional parameters required to achieve this splitting ratio are shown in table 4.5.

Table 4.5 – Parameters for the Blackman Window power divider 3.

a	b	c	d	e	f	g	h	i	j	r1	r2
1.27	2.54	0.5	1.13	0.68	0.87	0.62	0.87	0.5	0.315	0.3	1

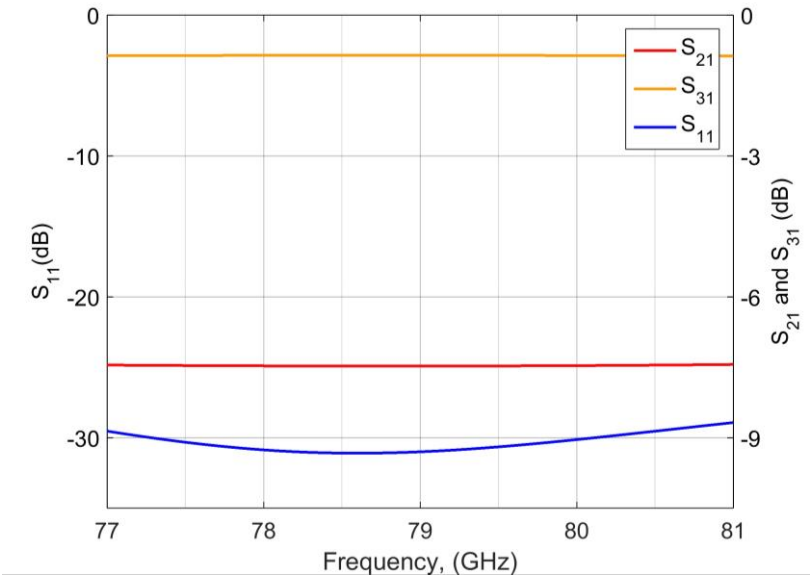

Figure 4.23 –S-parameters simulation for Blackman power divider 3.

Power divider type 4

The split ratio of the type 4 power divider should be of -3.97 dB and -2.22 dB for the S_{21} and S_{31} parameters, respectively. The dimensional parameters required to achieve this splitting ratio are shown in table 4.6.

Table 4.6 – Parameters for the Blackman Window power divider 4.

a	b	c	d	e	f	g	h	i	j	r1	r2
1.27	2.54	0.75	1.13	1.17	0.87	0.59	0.87	0.54	0.19	0.3	1

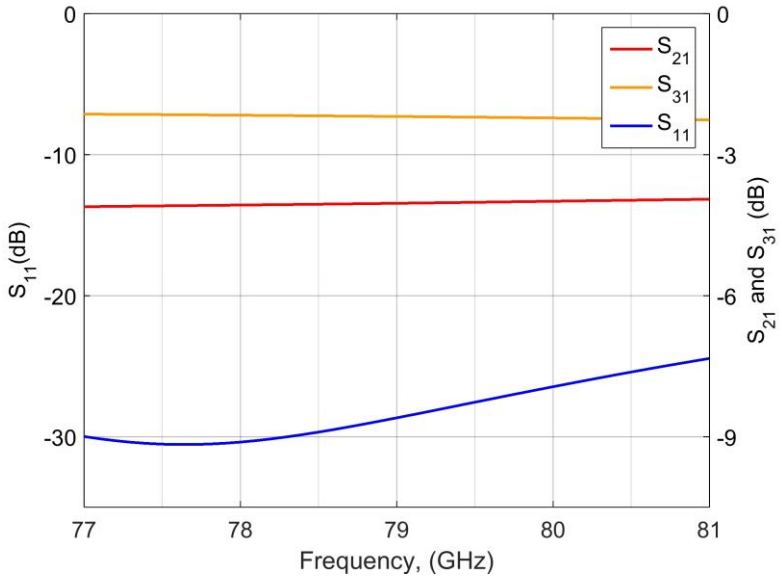

Figure 4.24 – S-parameters simulation for Blackman power divider 4.

Table 4.7 – S-Parameters for the Blackman Window power dividers.

	S_{21} at 79 GHz		S_{31} at 79 GHz	
	Theoretical	Simulated	Theoretical	Simulated
PD 2	-7.68	-7.74	-0.81	-0.81
PD 3	-7.44	-7.47	-0.86	-0.86
PD 4	-3.97	-4.03	-2.22	-2.19

Gaussian Window σ=0.3

Power divider type 2

For the Gaussian window, the split ratio of the type 2 power divider should be of -8.95 dB and -0.59 dB for the S_{21} and S_{31} parameters, respectively. The dimensional parameters required to achieve this splitting ratio are shown in table 4.8.

Table 4.8 –Parameters for the Gaussian Window power divider 2.

a	b	c	d	e	f	g	h	i	j	r1	r2
1.27	2.54	0.41	1.13	0.61	0.87	0.65	0.87	0.49	0.01	0.3	1

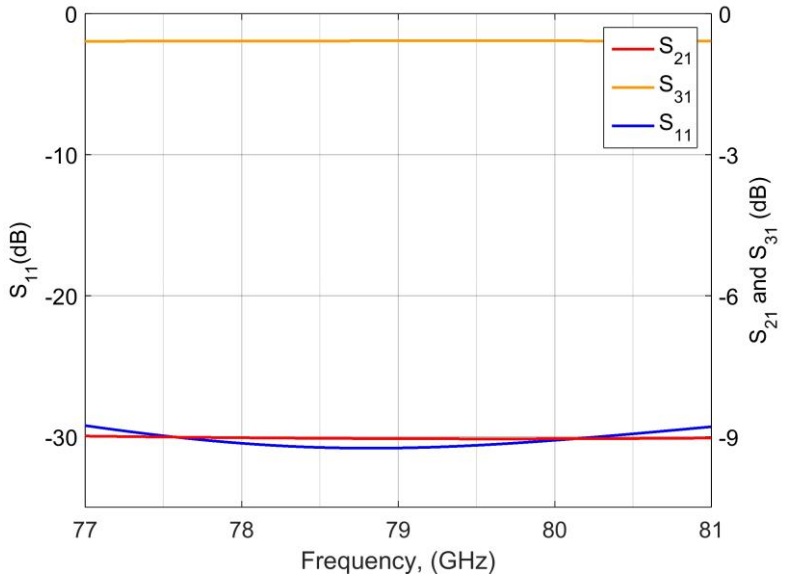

Figure 4.25 – S-parameters simulation for Gaussian power divider 2.

Power divider type 3

The split ratio of the type 3 power divider should be of -7.88 dB and -0.77 dB for the S_{21} and S_{31} parameters, respectively. The dimensional parameters required to achieve this splitting ratio are shown in table 4.9.

Table 4.9 –Parameters for the Gaussian Window power divider 3.

a	b	c	d	e	f	g	h	i	j	r1	r2
1.27	2.54	0.48	1.12	0.62	0.87	0.61	0.87	0.5	0.32	0.3	1

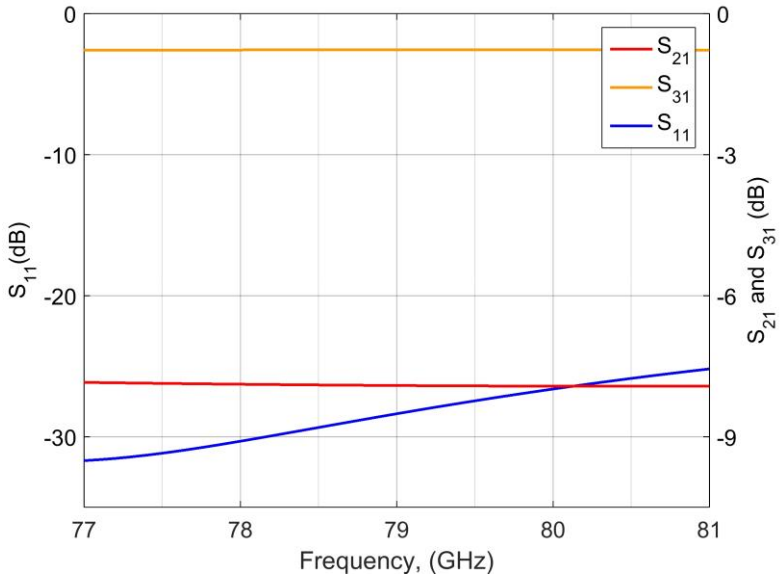

Figure 4.26 –S-parameters simulation for Gaussian power divider 3.

Power divider type 4

The split ratio of the type 4 power divider should be of -4.37 dB and -1.98 dB for the S_{21} and S_{31} parameters, respectively. The dimensional parameters required to achieve this splitting ratio are shown in table 4.10.

Table 4.10 – Parameters for the Gaussian Window power divider 4.

a	b	c	d	e	f	g	h	i	j	r1	r2
1.27	2.54	0.72	1.1	1.04	0.87	0.48	0.87	0.64	0.19	0.3	1

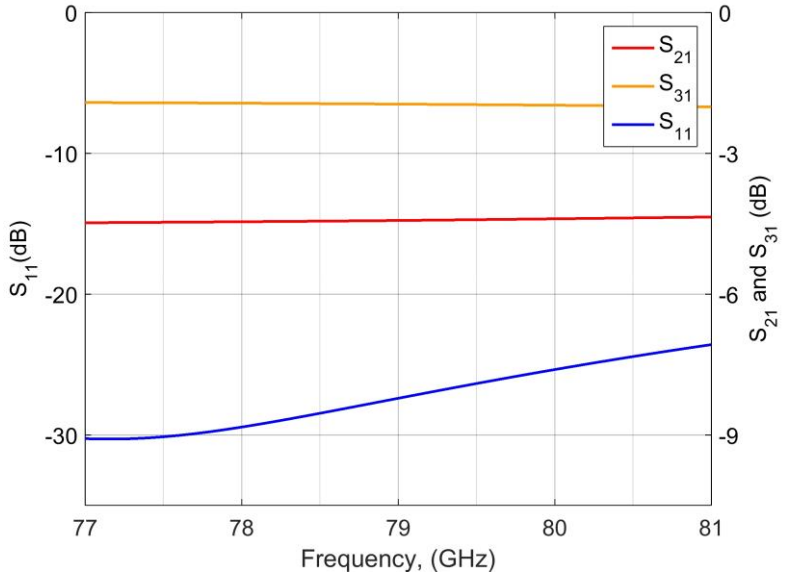

Figure 4.27 – S-parameters simulation for Gaussian power divider 4.

Table 4.11 – S-Parameters for the Gaussian Window power dividers.

	S_{21} at 79 GHz		S_{31} at 79 GHz	
	Theoretical	Simulated	Theoretical	Simulated
Power divider 2	-8.95	-9.04	-0.59	-0.58
Power divider 3	-7.88	-7.91	-0.77	-0.77
Power divider 4	-4.37	-4.43	-1.98	-1.95

Hanning Window

Power divider type 2

For the Hanning window, the split ratio of the type 2 power divider should be of -6.28 dB and -1.16 dB for the S_{21} and S_{31} parameters,

respectively. The dimensional parameters required to achieve this splitting ratio are shown in table 4.12.

Table 4.12 – Parameters for the Hanning Window power divider 2.

a	b	c	d	e	f	g	h	i	j	r1	r2
1.27	2.54	0.6	1.12	0.7	0.87	0.58	0.87	0.5	0.26	0.3	1

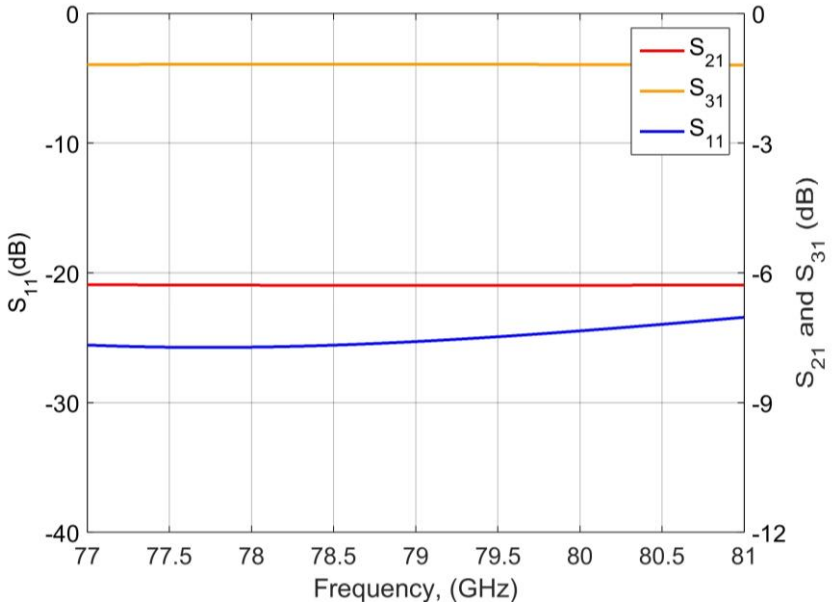

Figure 4.28 –S-parameters simulation for Hanning power divider 2.

Power divider type 3

The split ratio of the type 3 power divider should be of -6.46 dB and -1.11 dB for the S_{21} and S_{31} parameters, respectively. The dimensional parameters required to achieve this splitting ratio are shown in table 4.13.

Table 4.13 – Parameters for the Hanning Window power divider 3.

a	b	c	d	e	f	g	h	i	j	r1	r2
1.27	2.54	0.6	1.13	0.66	0.87	0.58	0.87	0.5	0.26	0.3	1

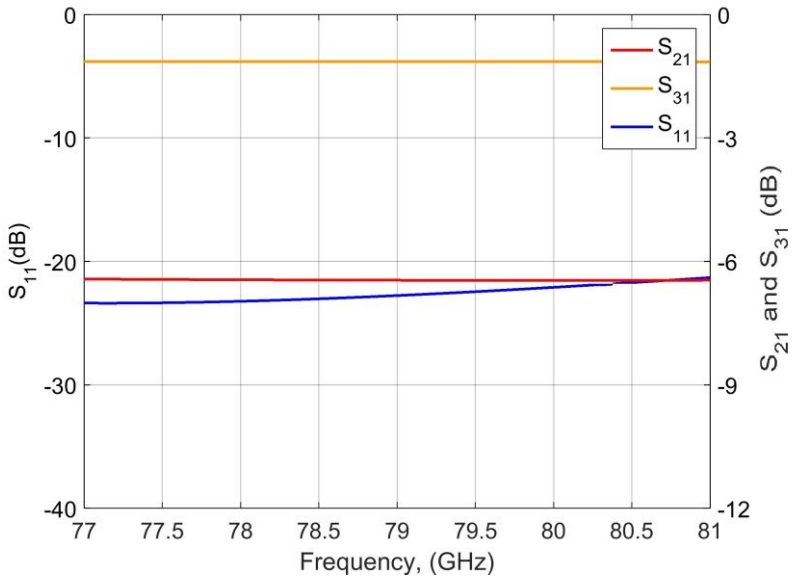

Figure 4.29 – S-parameters simulation for Hanning power divider 3.

Power divider type 4

The split ratio of the type 4 power divider should be of -3.6 dB and -2.48 dB for the S_{21} and S_{31} parameters, respectively. The dimensional parameters required to achieve this splitting ratio are shown in table 4.14.

Table 4.14 – Parameters for the Hanning Window power divider 4.

a	b	c	d	e	f	g	h	i	j	r1	r2
1.27	2.54	0.78	1.17	1.35	0.87	0.56	0.87	0.52	0.19	0.3	1

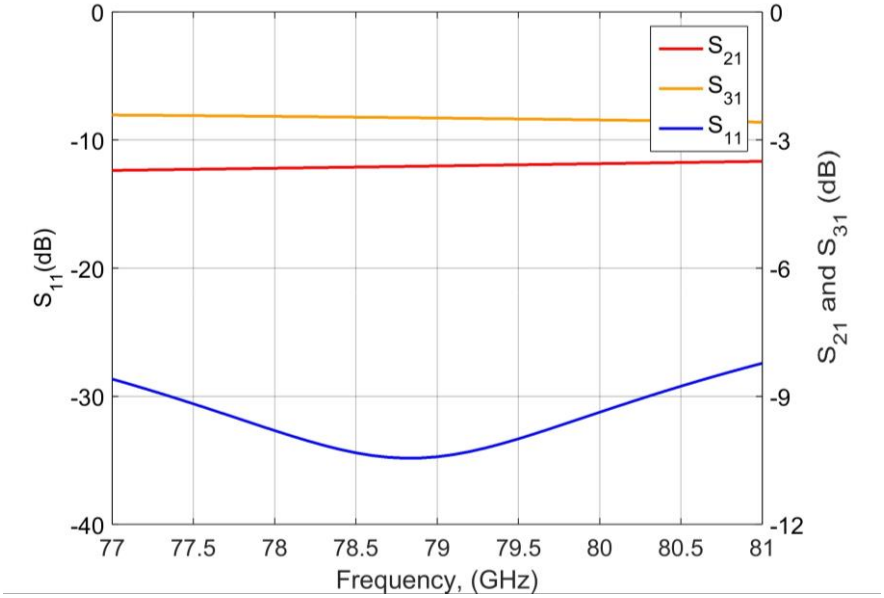

Figure 4.30 – S-parameters simulation for Hanning power divider 4.

Table 4.15 – S-Parameters for the Hanning Window power dividers.

	S_{21} at 79 GHz		S_{31} at 79 GHz	
	Theoretical	Simulated	Theoretical	Simulated
Power divider 2	-6.28	-6.25	-1.16	-1.19
Power divider 3	-6.46	-6.48	-1.11	-1.14
Power divider 4	-3.6	-3.62	-2.48	-2.48

Complete structure

The complete structure, with the power dividers adjusted for the values required by each of the three windows, has been simulated with Ansys HFSS [Hfs15], to validate the complete design of the

feeding network, and to verify that the required amplitudes are obtained at the output ports.

Blackman Window

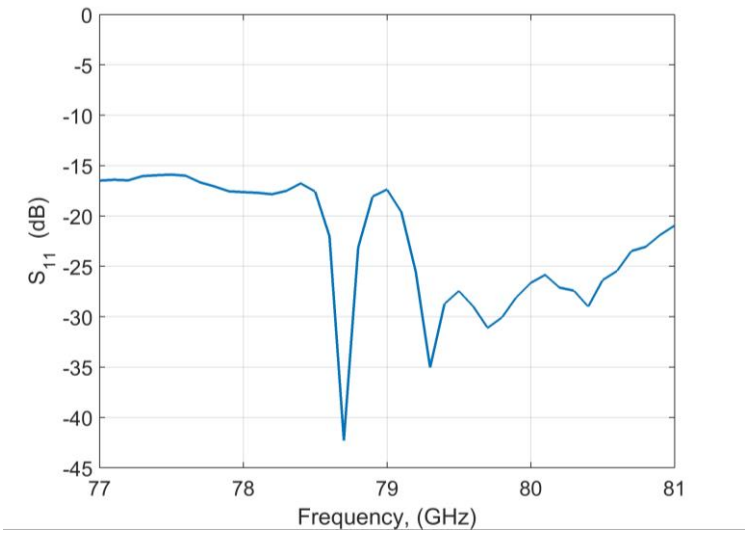

Figure 4.31 – S_{11} for the complete structure with Blackman Window.

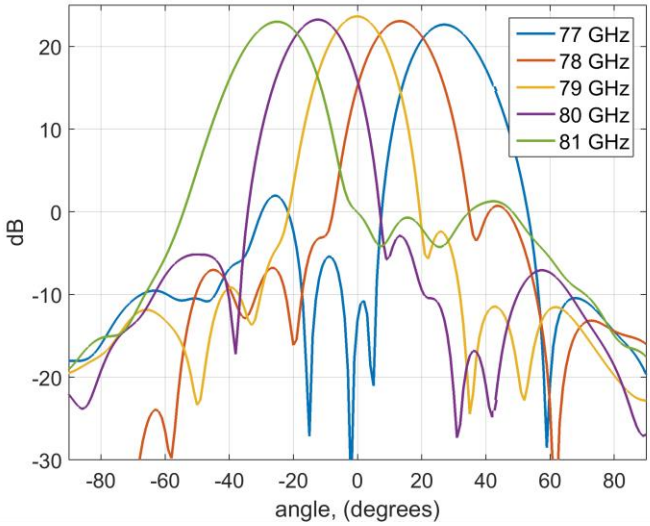

Figure 4.32 – E-plane radiation pattern for a 4 GHz beamwidth Blackman Window.

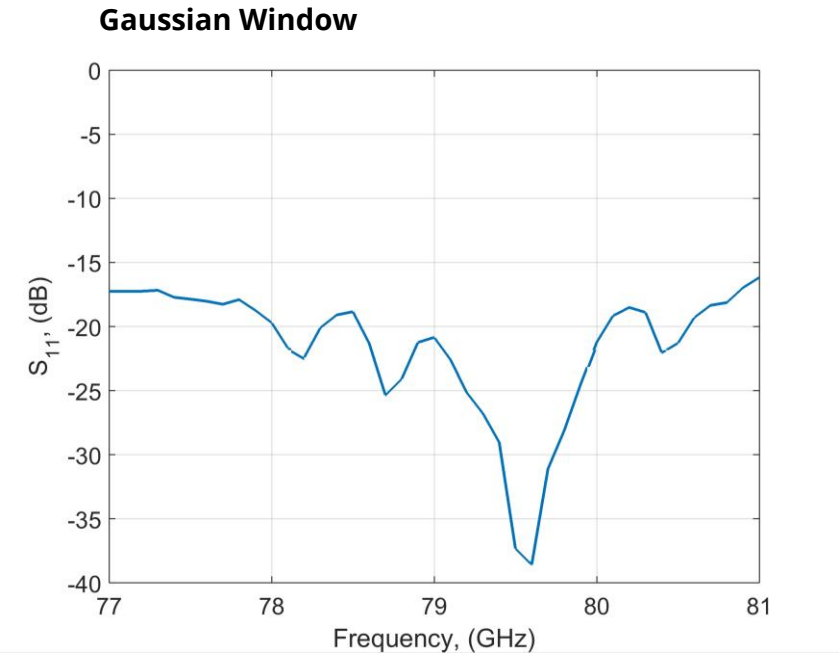

Figure 4.33 – S_{11} for the complete structure with Gaussian Window.

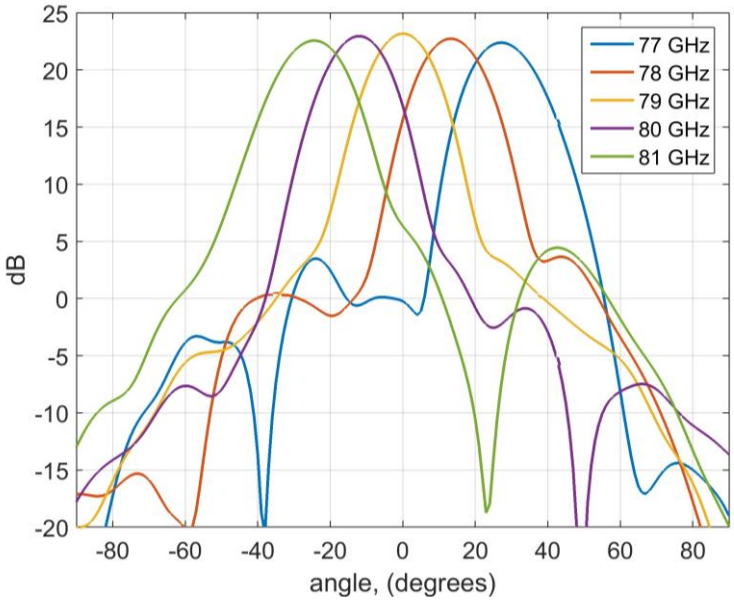

Figure 4.34 – E-plane radiation pattern for a 4 GHz beamwidth Gaussian Window.

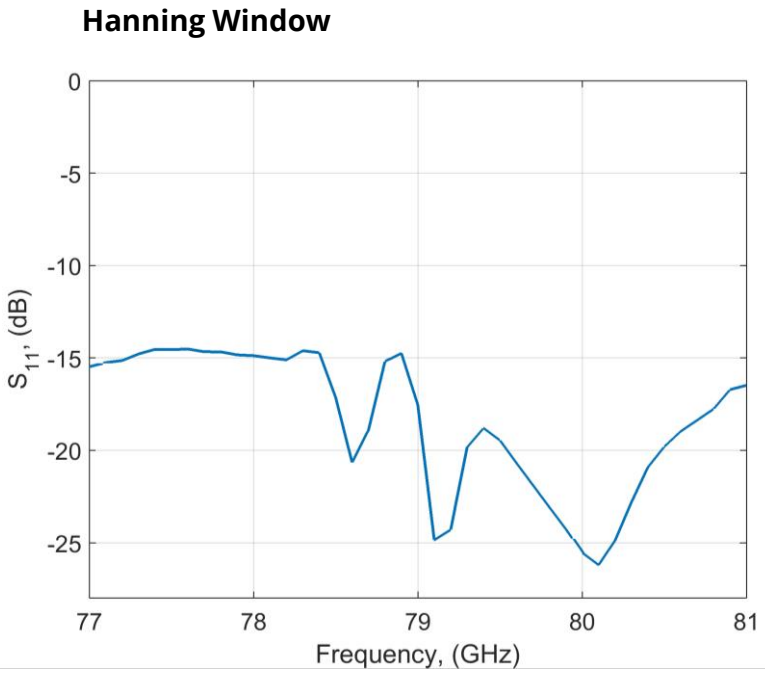

Figure 4.35 – S_{11} for the complete structure with Hanning Window.

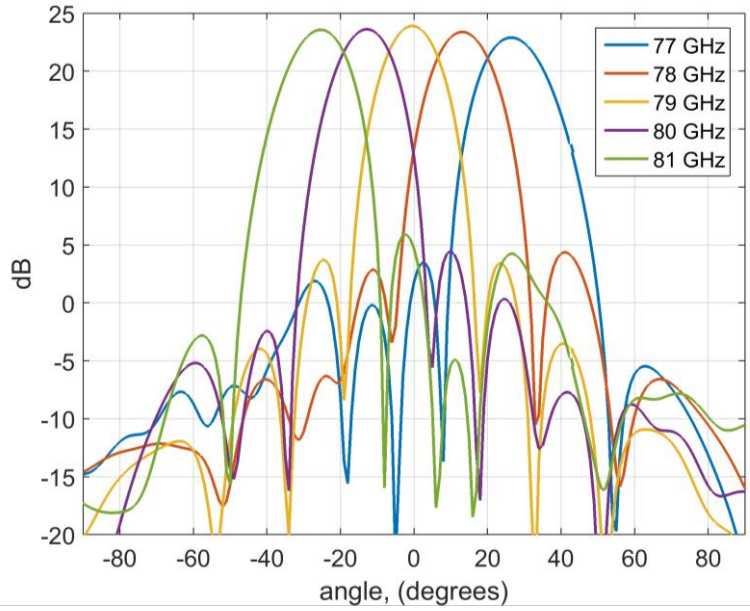

Figure 4.36 – E-plane radiation pattern for a 4 GHz beamwidth Hanning Window.

Table 4.16 – Maximum directivity for the whole band and the three windows.

	Maximum directivity (dB)		
Frequency (GHz)	Blackman	Gaussian	Hanning
77	22.64	22.39	22.89
78	23.06	22.73	23.38
79	23.63	23.18	23.89
80	23.24	23.24	23.62
81	22.98	22.56	23.57

Table 4.17 – Scan loss comparison study for the three windows.

	Scan loss (dB)		
Frequency (GHz)	Blackman	Gaussian	Hanning
77	1	0.79	1
78	0.58	0.45	0.51
79	0	0	0
80	0.39	0.22	0.27
81	0.65	0.62	0.32

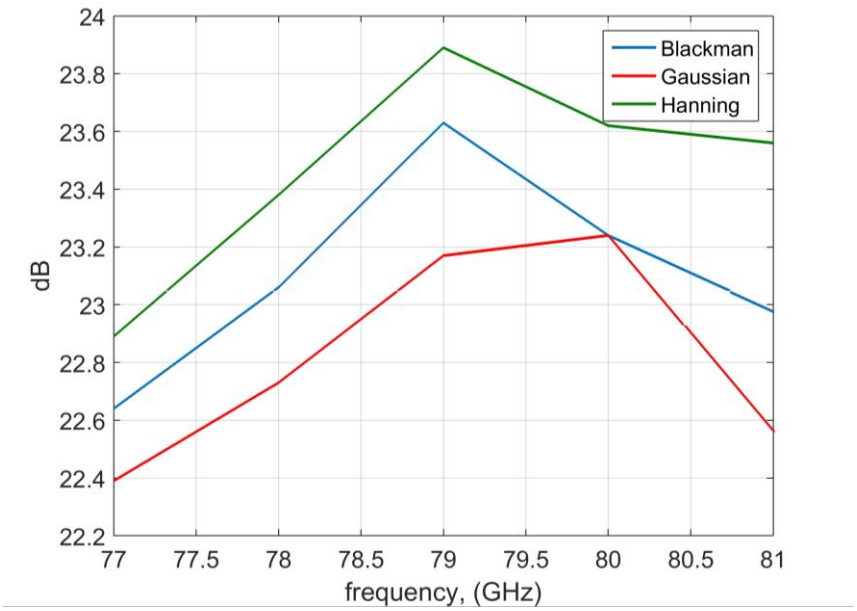

Figure 4.37 –Maximum value comparison for the three windows.

Table 4.18 – -3 dB and – 10dB beamwidth for the three windows.

Frequency (GHz)	BeamWidth					
	Blackman		Gaussian		Hanning	
	BW_{-3dB}	BW_{-10dB}	BW_{-3dB}	BW_{-10dB}	BW_{-3dB}	BW_{-10dB}
77	18	32	20	34	18	30
78	17	30	19	33	15	27
79	16	28	16	30	15	26
80	16	29	18	33	16	26
81	18	34	20	35	16	28

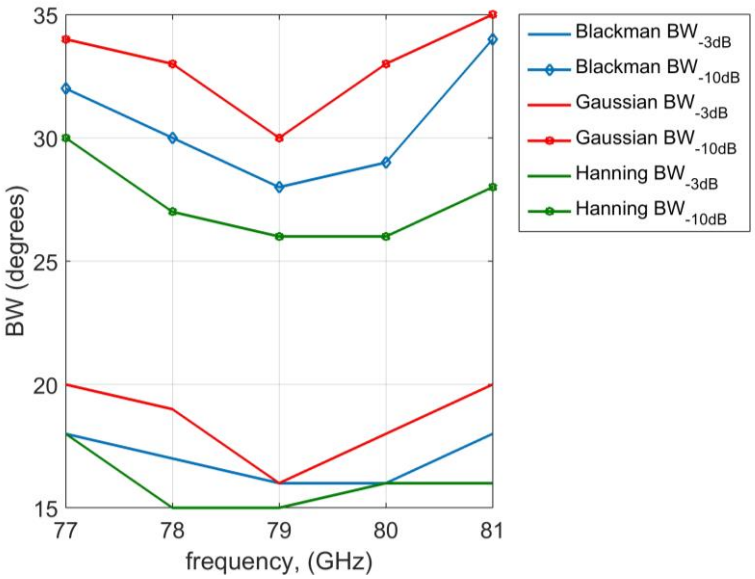

Figure 4.38 –Figure 4.38 – -3 dB and – 10dB beamwidth values for the three windows.

Table 4.19 – Side lobe level value with respect to main lobe value..

Frequency (GHz)	Side lobe level with respect to main lobe		
	Blackman	Gaussian	Hanning
77	20.71	18.89	20.01
78	22.02	21.7	19.24
79	25.98	n/a	19.74
80	26.23	23.88	19.36
81	21.73	18.28	17.87

After carefully considering all the results of the window study, it was decided that the Hanning window offered a good compromise between directivity, scan loss, and sidelobe level, being the candidate window for the second prototype of frequency scanning array.

4.2.1 Radiating elements.

The front-end 8-horn array antenna used in the previous chapter worked fine, so it was decided to keep it in this new design, only scaling it down for the new frequency configuration. Its main advantage is that it can be easily fabricated by means of available electro discharge machining (EDM). This antenna array has been designed to produce a narrow and symmetrical radiation pattern. The input aperture of each individual horn antenna is 2.54 x 1.27 mm^2 (WR-10 waveguide) and the output aperture is 27.5 x 15 mm^2 (27.5 x 1.7 mm^2 for each one of the pyramidal horns, so each horn is nearly an H-plane horn).

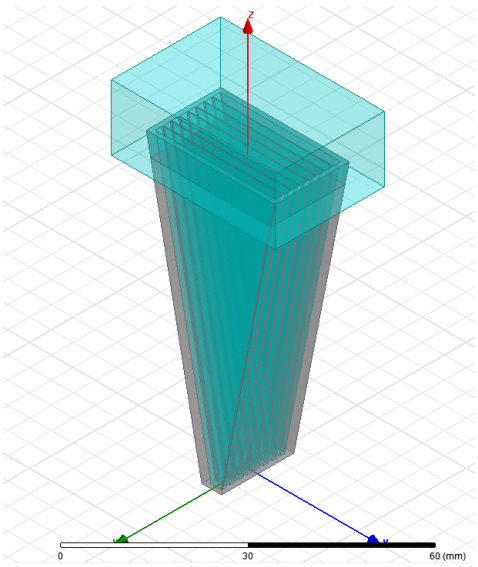

Figure 4.39 – 8-horn antenna array with 1.9 mm separation between elements.

4.2.1.1 Simulation

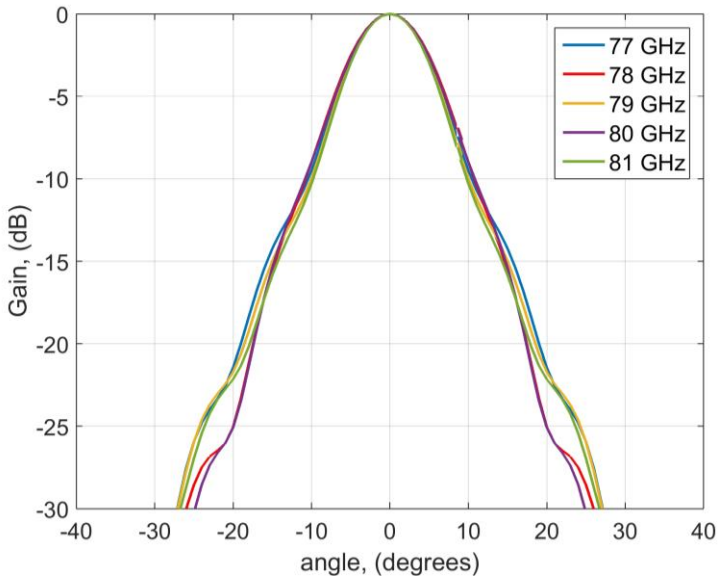

Figure 4.40 – H-plane radiation diagram of the eight horn antenna array.

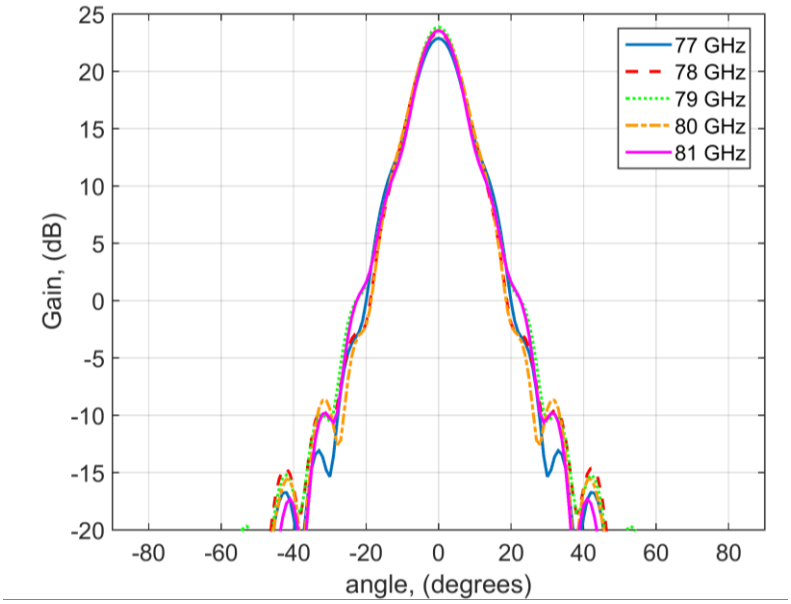

Figure 4.41 – H-plane radiation pattern for the complete structure.

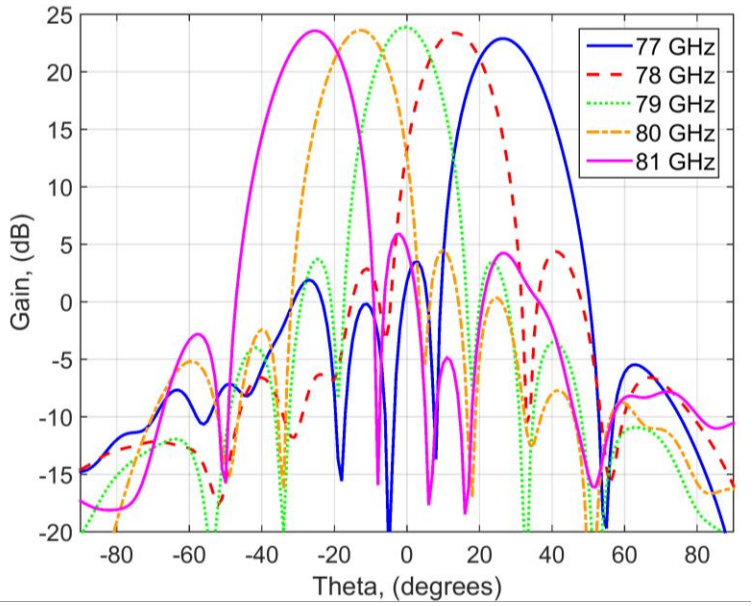

Figure 4.42 – E-plane radiation pattern for the complete structure and 4 GHz bandwidth.

4.2.2 Parabolic Reflector

As the aim of this work is to design a cost-effective imaging system, the use of a commercially available paraboloid reflector was desirable. According to the desired resolution level and the size of the horn array, it was convenient to choose a reflector with relatively high f/D ratio and diameter, D. However, low cost commercially available reflectors with large f/D relation have often a small diameter, not large enough for this application. After a thorough search, an Edmund Optics paraboloid reflector with f/D= 0.25 and diameter D=609.6 mm has been chosen to provide a fair trade-off between low cost and nice performance, (http://www.edmundoptics.es/optics/optical-mirrors/focusing-concave-mirrors/large-parabolic-reflectors/53876/).

Several simulations have been performed with the Ticra's GRASP software [Tic08] in order to determine the optimal reflector configuration. Finally, an offset configuration has been chosen, determining that the 50º of the total scan angle is translated into a linear sweep of approximately 20cm in the image plane placed at 0.5m from the reflector surface. This sweep is considered to be enough for demonstration purposes.

The Edmund Optics symmetrical parabolic reflector has been cut to obtain an offset reflector configuration, as can be seen in Fig. 4.43.

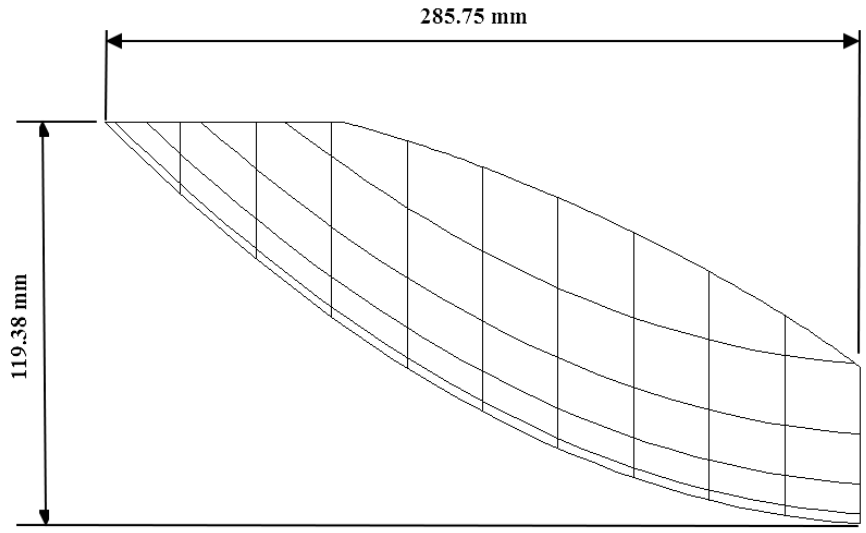

Figure 4.43 – Cut of the Edmun Optics reflector.

The cut process had to be performed very carefully to avoid generating any deformation in the mirror paraboloid shape. To guarantee that, a plaster cast of the mirror was done, in order to support the surface during the cutting process, as it can be seen in figure 4.44.

Figure 4.44 – Cut process of the Edmun Optics reflector.

4.2.3 Prototype fabrication and experimental results.

The array antenna has been fabricated in aluminium, using milling for the two E-plane split halves of the feeding network, and wire EDM machining for the single piece horn array.

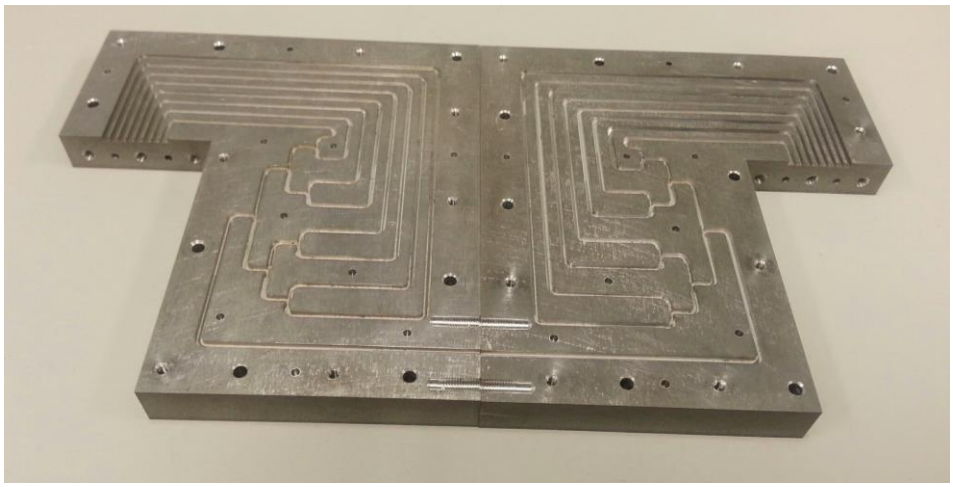

Figure 4.45 – Symmetrical halves of the feeding network structure.

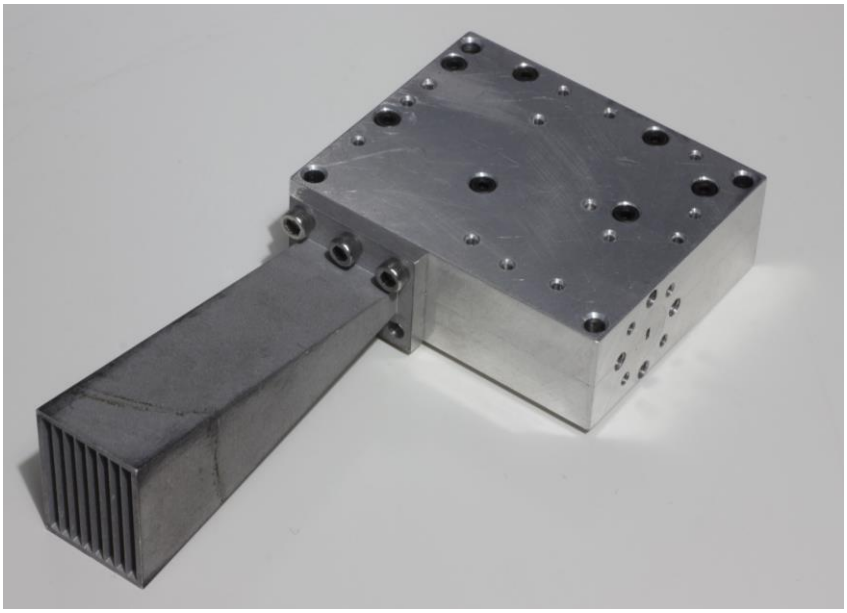

Figure 4.46 –Complete manufactured structure.

The system is completed with the reflector, and metallic profiles and 3D printed components for attachment and structural support. A conveyor belt is placed under the structure to move the targets through the system, simulating the operation of a real system. The following figures show the 3D models of the individual components of the system, and the complete assembly.

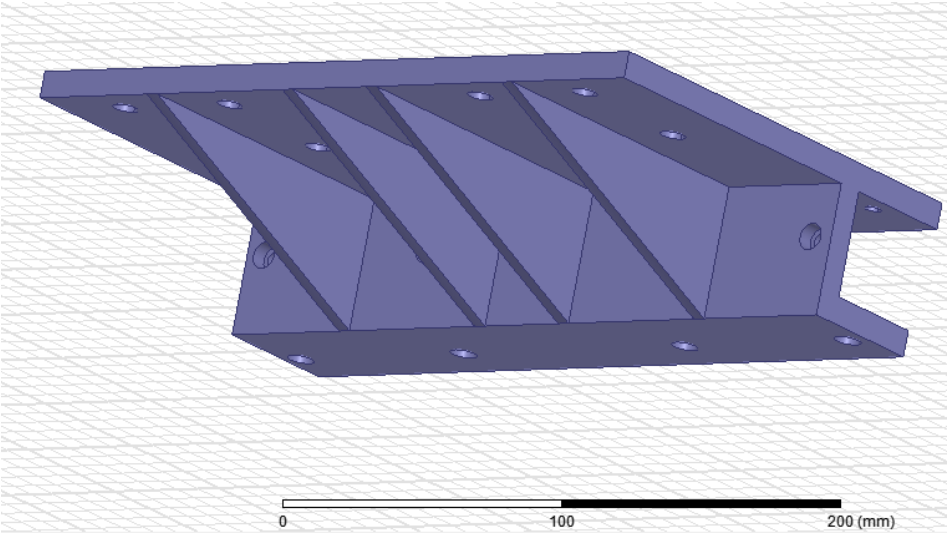

Figure 4.47 –Piece used to attach the VNA extender to the profile structure.

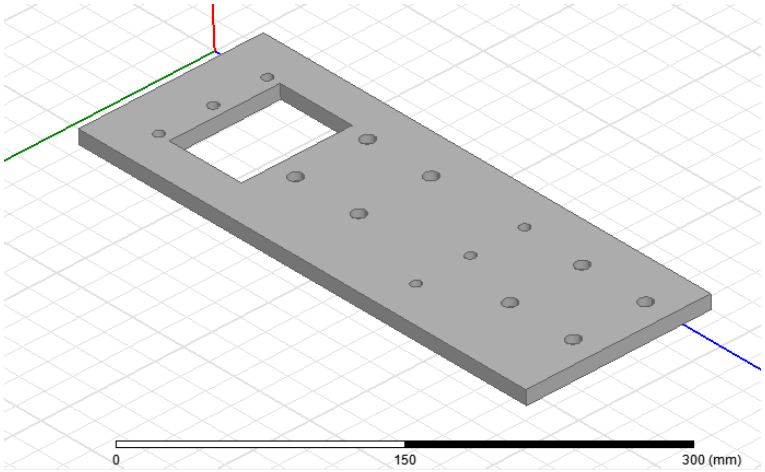

Figure 4.48 – Piece used to attach the VNA extender to the inclinometers.

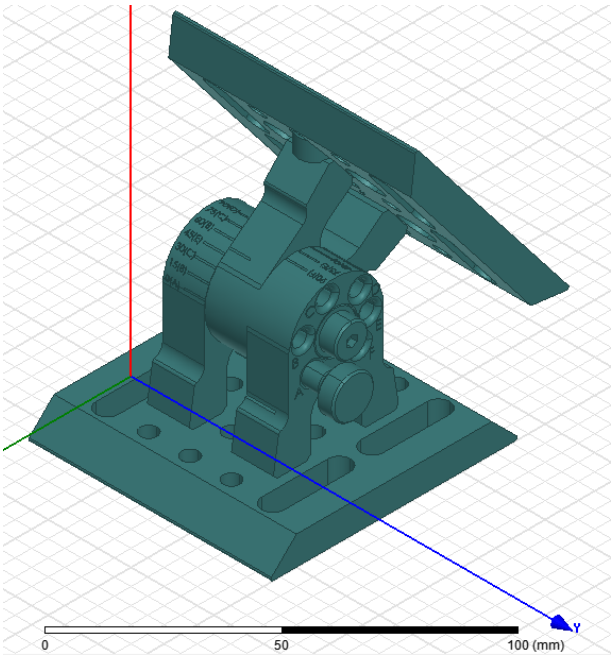

Figure 4.49 –Thorlabs articulating base AP180 used to achieve the desired inclination with the antenna.

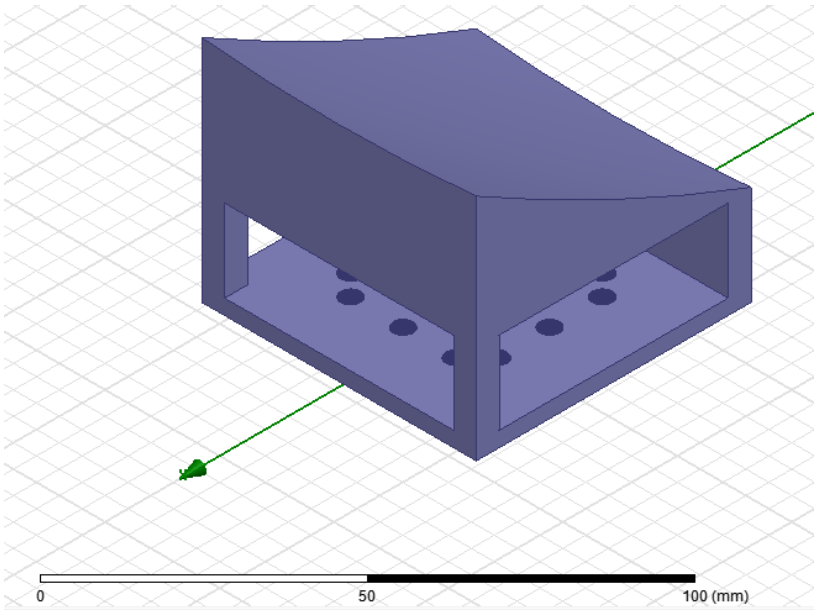

Figure 4.50 – 3-D printed piece to attach the mirror.

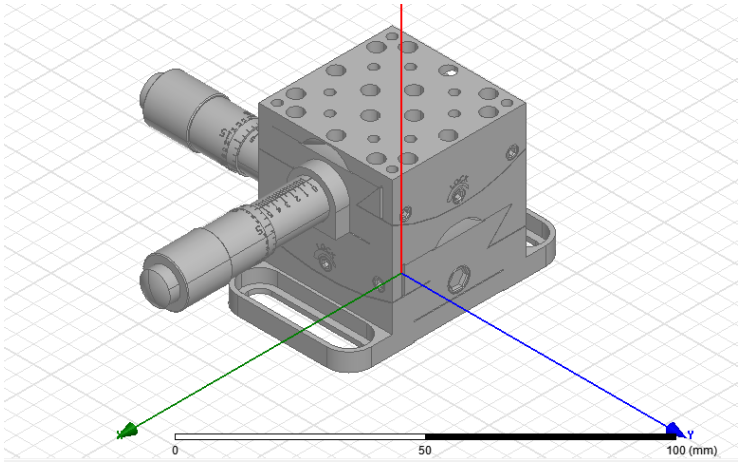

Figure 4.51 –Thorlabs Goniometer GNL20 used to align the mirror.

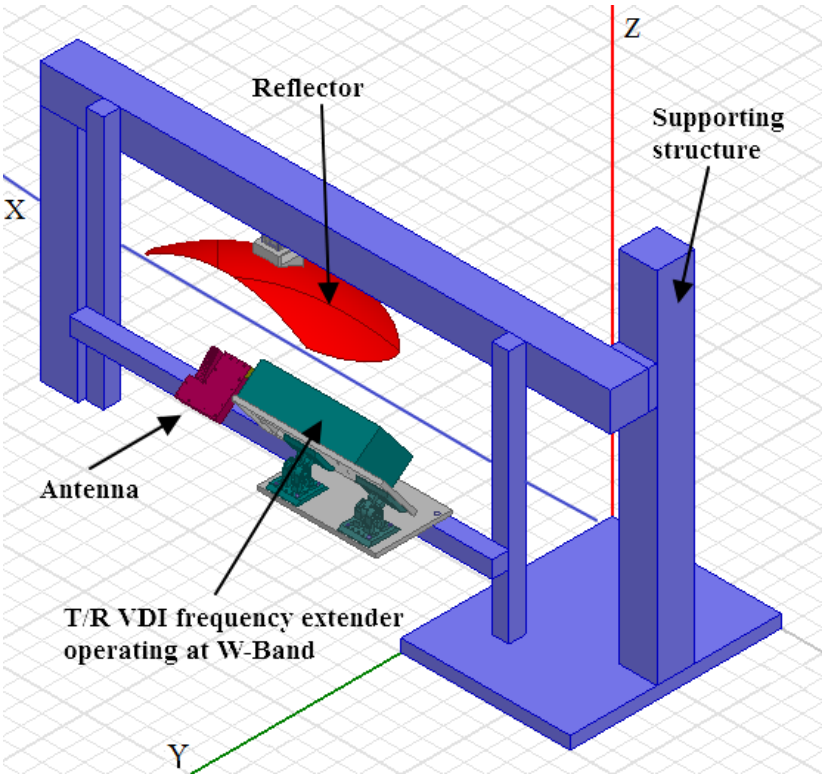

Figure 4.52 –Complete imaging system including the frequency scanning antenna and the mirror, no movable parts are needed in the RF chain, the image is formed by frequency scanning in the X axis and the conveyor belt movement in the Y axis.

The components include precision angle plates and goniometers for precise adjustment and control of the system, metallic plates and profiles, and 3D printed components that take advantage of the rapid prototyping approach brought by this new fabrication technology.

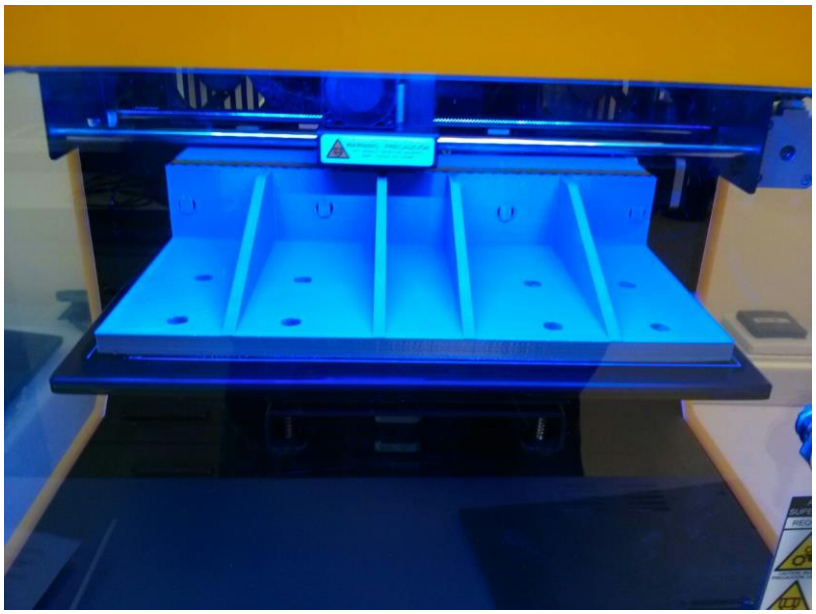

Figure 4.53 –3D printed prototype.

Measurements

The horn array antenna and the complete system have been measured in a planar near-field test setup, in order to verify agreement with the simulation results, and also to properly characterize the system for the image processing that will be done in the next section. The measurement methods were previously described in chapter 3 and the same procedures were followed in this case.

The measurement was performed with an Agilent PNA-X N5242A network analyzer equipped with two VDI (Virginia Diodes) millimeter wave frequency extenders operating in the W band.

Fig. 4.55 shows the measured E-plane radiation pattern of the horn array and the feeding network. A frequency shift of about 1 GHz can be observed due to the thigh manufacturing tolerances required by the incremental path length strategy used by the feeding network. Also, measured losses are around 2 dB, when compared to the simulations. The measured sidelobe level is higher than in the simulations due to imbalances in the fabricated power dividers, but it is below 12 dB compared to the main beam in the worst case, so it is still an important improvement compared with the previous prototype where the measured worst case sidelobe level was only 5 dB below the main beam. Fig. 4.56 and 4.57 show the measured beamspots at the image plane of the system that will be used for imaging results post-processing.

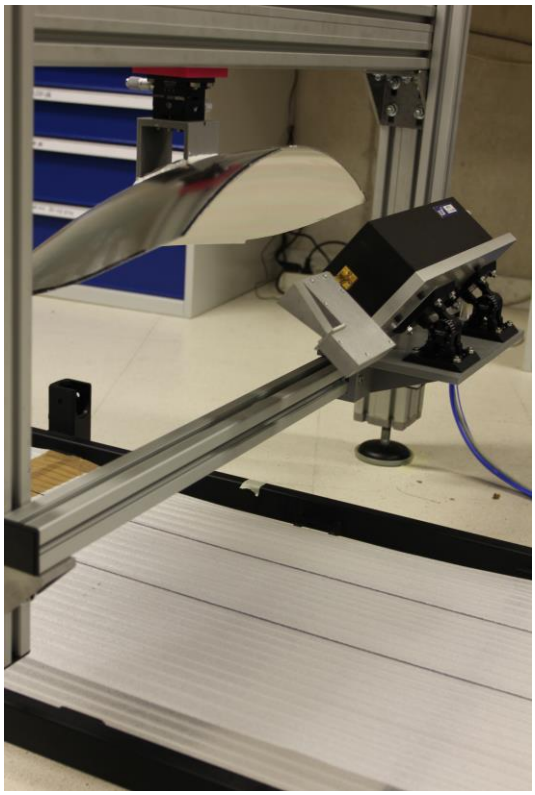

Figure 4.54 –Complete system with the conveyor belt placed under it.

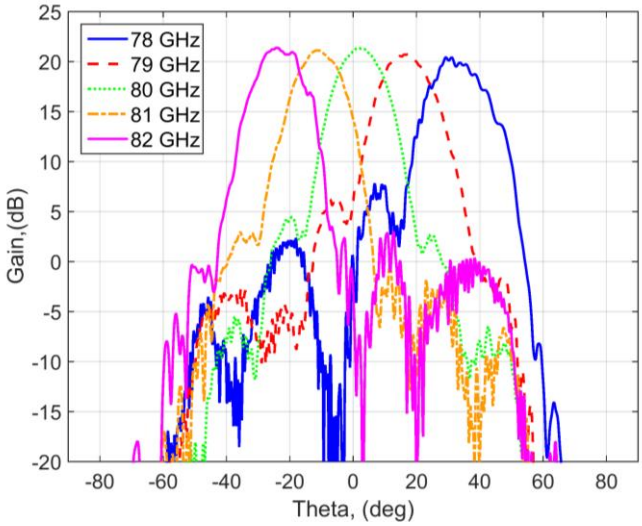

Figure 4.55 –Measured E-plane radiation pattern of the horn array.

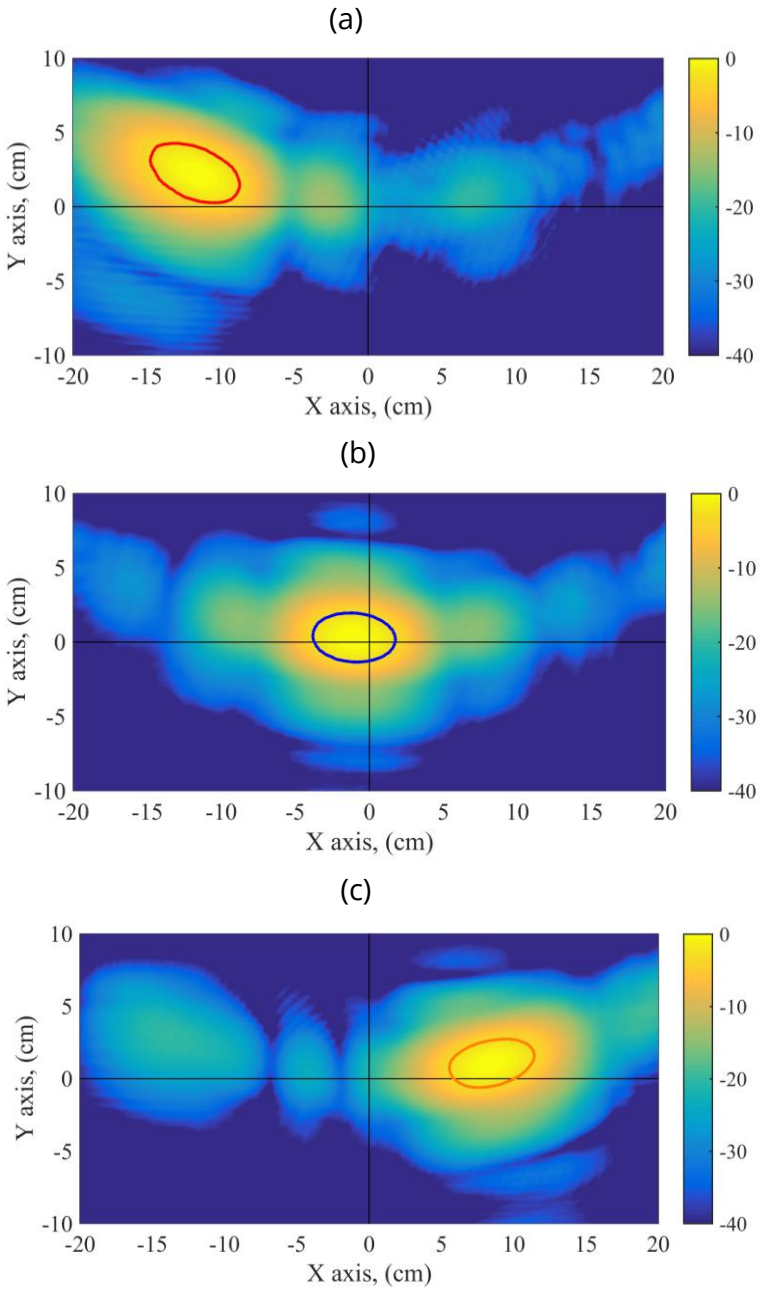

Figure 4.56 –Measured radiation pattern in the image plane 50 cm away from the mirror at (a) 78 GHz (b) 80GHz (c) 82 GHz.

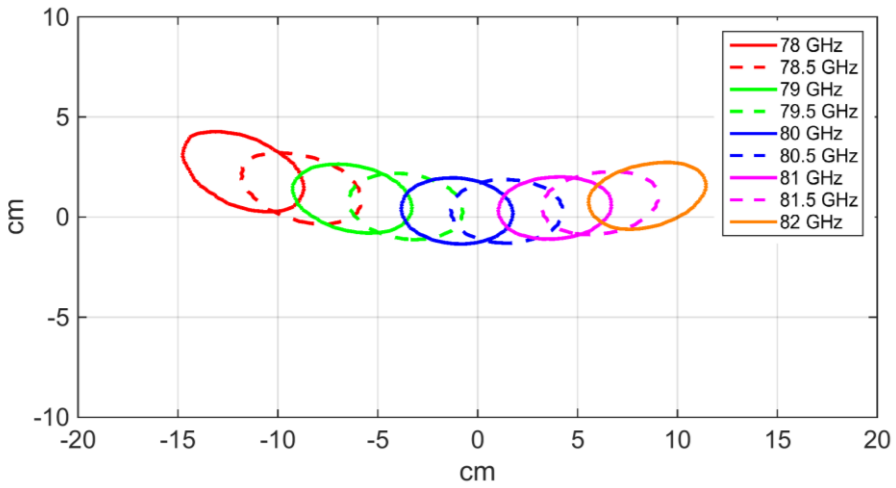

Figure 4.57 –Measured beamspots in the image plane.

4.3 Image Postprocessing

Although the radiation pattern of the presented frequency scanning antenna exhibits a significant improvement with respect to [Lar14], the spot size is still relatively large and, consequently, it will result in a distortion of the images. In this section, it is shown how the quality of images can be improved by applying an appropriate deconvolution. This postprocessing, requires a number of steps and approximations, to conveniently produce a two-dimensional image from the acquisition of the S_{11} parameter for multiple frequencies at a given time rate.

4.3.1 Radiation pattern deconvolution

The amplitude received by the frequency scanning antenna working as a monostatic radar is given by:

$$M(f,\Delta y) = \int_S |E(x,y,z_0)|^2 \, \Gamma_{obj}(x,y+\Delta y) ds \quad (4.18)$$

where Γ_{obj} is the reflectivity of the object, Δy is the displacement of the object due to the movement of the conveyor belt and E is the electric field at the plane of the object under test $z = z_0$. The square superscript is included in (4.18) due to the monostatic setup.

Since the field *E* can be measured in a calibration stage and *M* is the (known) measured signal, eq. (4.18) depicts a standard *inverse scattering* problem modeled by an *integral equation*. The solution of this kind of problems is usually based on discretizing the unknown variable to yield a matrix equation [Pas10]. Nevertheless, this approach is challenging as it entails dealing with poor conditioned systems of equations [Pas10]. Consequently, this technique is mainly useful for systems providing high signal to noise ratios and enhanced by an appropriate regularization scheme. Furthermore, the solution of these matrix problems is usually computationally expensive and, therefore, they are not convenient for a *real-time* imager.

In order to achieve a robust and efficient solution of (4.18), some simplifications will be applied. In particular, it will be assumed that the spot moves linearly along the *x*-axis.

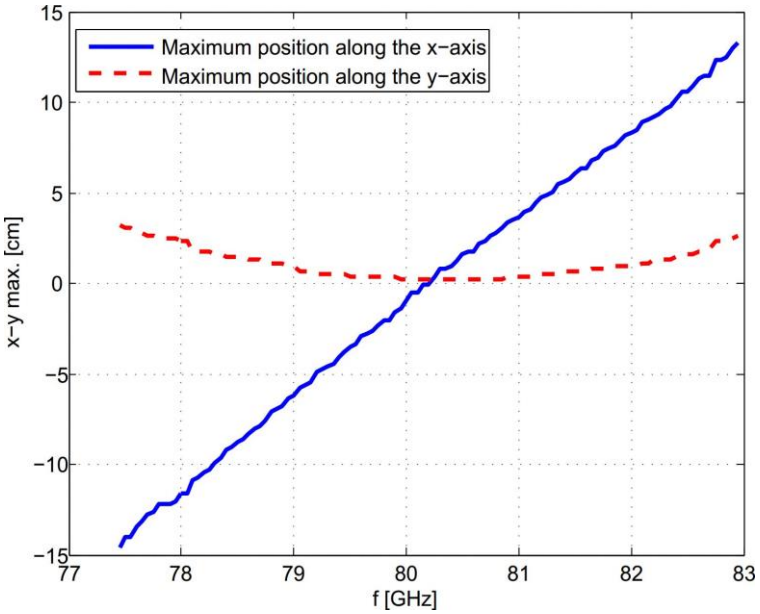

Figure 4.58 –Position of the maximum of the spot in the *x*- and *y*-axes versus frequency at *z* = 50cm.

Thus, the position of the spot can be described as a function of the frequency as:

$$\vec{r}_{spot} = a(f - f_c)\hat{x} \quad (4.19)$$

wherein a accounts for the spot movement rate and f_c is the center frequency. This simplification is supported by Figure 4.58 –. depicting the position of the maximum of the spot for an acquisition at *z* = 50cm. It is clearly seen that the position along the *x*-axis has a linear dependency. Applying a linear regression to the previous curve, it has been obtained that a = 4.93 cm/GHz. On the other hand, the position of the spot along the *y*-axis suffers only a moderate movement.

Next, it is also assumed that the spot shape does not depend on the frequency. Although the spot suffers some tilt when it moves along the XY plane (see Fig. 4.57), this effect is small along the center

frequency as the curve of the spot maximum is almost flat. Under the previous simplification, eq. (4.18) can be expressed as:

$$M(\Delta x, \Delta y) \approx \int_x \int_y PSF(x + \Delta x, y, z_0)\Gamma_{obj}(x, y + \Delta y)dxdy \quad (4.20)$$

where the displacement along x is related to the frequency by $\Delta x = a(f - f_c)$ and *PSF* is a point spread function (PSF) that is the responsible of the blurring of the image. This function is related to field of the antenna by:

$$PSF = E^2(x, y, z_0, f_c) \quad (4.21)$$

In order to achieve a flexible implementation, it is convenient to approximate the PSF by an analytic function so that the values can be easily tuned in the final implementation. After observing the electric field shown in Fig. 4.55, it has been observed that a Gaussian function provides a good fitting. Hence, the expression for the point spread function is approximated by:

$$PSF(x, y) \approx \frac{1}{2\pi\sigma_x\sigma_y} exp\left(-\frac{x^2}{2\sigma_x^2} - \frac{y^2}{2\sigma_y^2}\right) \quad (4.22)$$

where the values of σ_X= 2.3 cm and σ_Y= 1.34 cm are found to provide an accurate model as shown in Fig. 4.60.

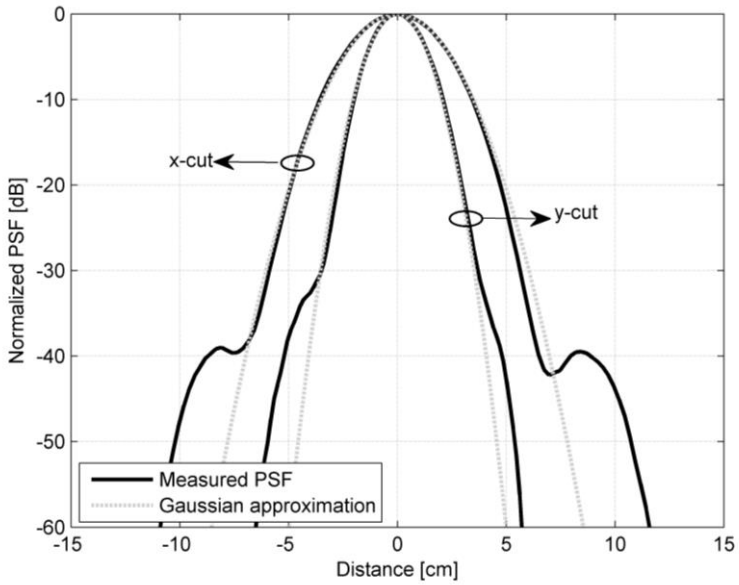

Figure 4.59 – Approximation of the point spread function by a Gaussian function with $\sigma_x = 2.3$cm and $\sigma_y = 1.34$cm. The point spread function has been measured at $f_c = 80.35$GHz.

Taking into account the symmetry of the point spread function, the integral equation described by (4.20) can be expressed as a convolution:

$$M(x,y) \approx PSF(x,y) * \Gamma_{obj}(x,y) \quad (4.23)$$

Thus, the solution of the integral equation described by (4.18) can be approximately solved by deconvoluting the measured signal with a known function. This kind of problem is well known in a number of fields including image processing or astronomy and, therefore, a large number of robust and efficient algorithms is available.

It is important to remark that these algorithms can partially remove the effect of the blurring introduced by the PSF. Nevertheless, the real image (or, in this case, the object reflectivity) is not completely recovered as the PSF performs a lowpass filtering and, consequently, high frequencies cannot be retrieved.

One of the most widespread deconvolution approaches for enhancing mm-wave images is the blind deconvolution [Spi12 and Fan14] which does not require the a priori knowledge of the PSF. Nevertheless, the radiation pattern of the antenna has been characterized in the proposed imager. Thus, it is more convenient to resort to deconvolution approaches that can take advantage of the knowledge of the PSF. In particular, the *Lucy-Richardson deconvolution* [Ric72, Luc74 and Zhe09] has been used in this work. This algorithm relies on an iterative refinement of the solution, which is given by the following expression:

$$\hat{\Gamma}_{obj}^{(t+1)}(x,y) = \hat{\Gamma}_{obj}^{(t)}(x,y)\left(\frac{|M(x,y)|}{\hat{\Gamma}_{obj}^{(t)}(x,y) * |PSF(x,y)|} * |PSF(x,y)|\right) \quad (4.24)$$

where the products and division are defined as element wise and $\hat{\Gamma}_{obj}^{(t)}$ is the estimation of the object reflectivity at iteration t.

Unless otherwise specified, the number of iterations is fixed to 10 in this work. The symmetry of the PSF has been used to further simplify the original expression [Ric72 and Luc74]. Although the phase of the measured signal would provide some additional information, which could improve the quality of the solution, it has been observed that this phase is very sensitive to any instability (e.g., vibrations of the conveyor belt). For this reason, amplitude-only data is used in (4.24).

Finally, it is also relevant to mention that the postprocessing includes a preliminary stage where the scattered field without any object is measured and, after that, it is subtracted to any measurement. In addition, a time gating is also applied. The purpose of both techniques is to mitigate the impact of unwanted reflections happening inside or outside the antenna.

4.3.2 Results for simulated data

In order to validate the performance of the proposed deconvolution to improve the quality of the imaging, let us firstly consider a simulated example. In this case, the object is an annulus with external radius of 5 cm and internal radius of 2 cm. The reflectivity is set to one for all the points inside the object. The simulated data is computed by introducing the electric field acquired as described in section II-E and the aforementioned reflectivity into (4.18).

Only the data from 77.45 GHz and 82.95 GHz is used yielding a total of 111 frequency points. The data is sampled along the *y*-axis with a spacing of 1.5 mm. Finally, white Gaussian noise is added to simulate a signal to noise ratio of 30 dB.

The simulated raw and postprocessed data are shown in Fig. 4.60. The raw image clearly resembles the real object but it lacks of some important details. On the other hand, the deconvoluted image reveals a clear improvement even if the real object is not perfectly retrieved due to the approximations and deconvolution limitations.

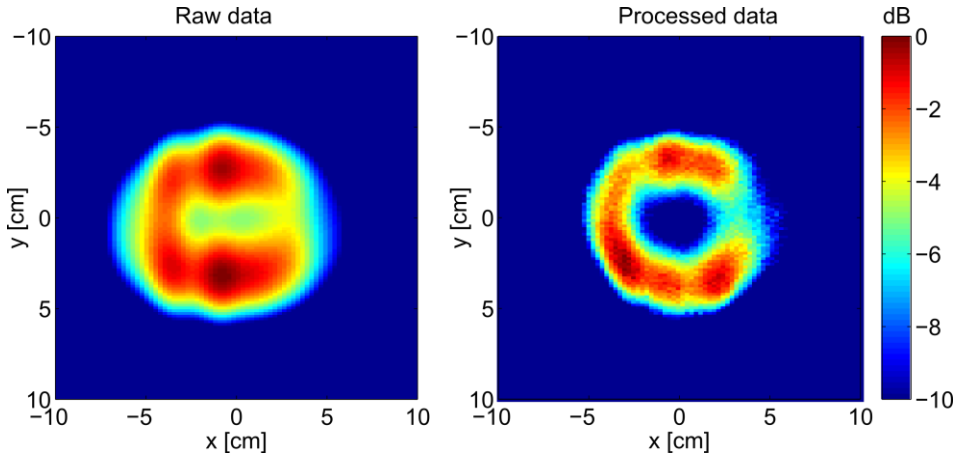

Figure 4.60 – Normalized images for a simulated object with ringshape.

4.3.3 Real time image results

In order to validate the performance the system, the frequency scanning antenna is connected to a vector network analyzer (VNA) which is set to sample 201 frequency points ranging from 75 GHz to 85 GHz. A time gating from 7.5 ns to 10 ns is used to filter undesired echoes from the floor as well as internal reflections in the antenna. The intermediate frequency (IF) filter bandwidth is set to 4 kHz resulting in a sweep time of 42.813 ms.

The objects that have been measured are a stick of aluminum foil with a diameter between 7 mm and 10 mm and length of 22 cm, a piece of glass with dimensions of approximately 7 mm x 11 mm, two aluminum foil balls with a diameter of approximately 3 mm and an hexagonal M4 nut (see Fig. 4.61).

The objects are placed on the conveyor belt (see Fig. 4.62) that is fed by DC source at 5 V resulting in a speed of approximately 4 cm/s. The obtained values for the modified time-gated S_{11} parameter for the raw and processed data are shown in Fig. 4.62. In these images, it is observed that the objects can be clearly detected by the system. Although the deconvolution cannot completely retrieve the objects and its impact is still visible, it significantly improves the resolution, especially along the *x*-axis, along which the PSF is wider.

(a)

(b)

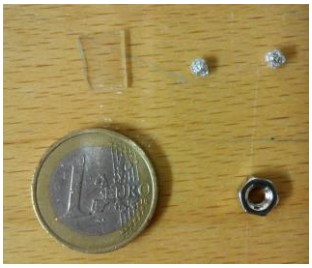

Figure 4.61 –Measured objects with enhanced imaging.

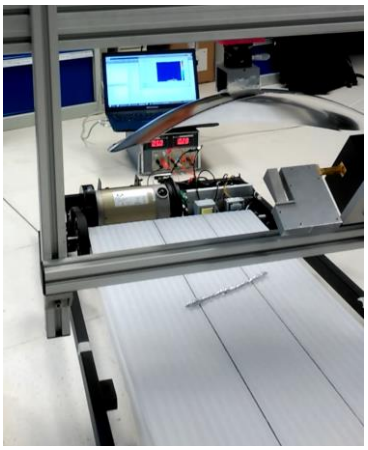

(a)

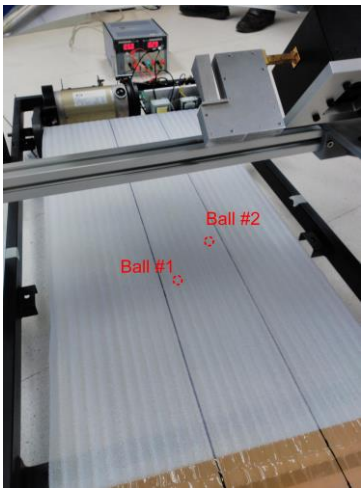

(b)

Figure 4.62 –Setup including objects: (a) aluminum foil stick with a tilt of approximately 45º; (b) aluminum foil balls with a separation of approximately 7 cm and 6 cm for the *x*- and *y*-axes respectively.

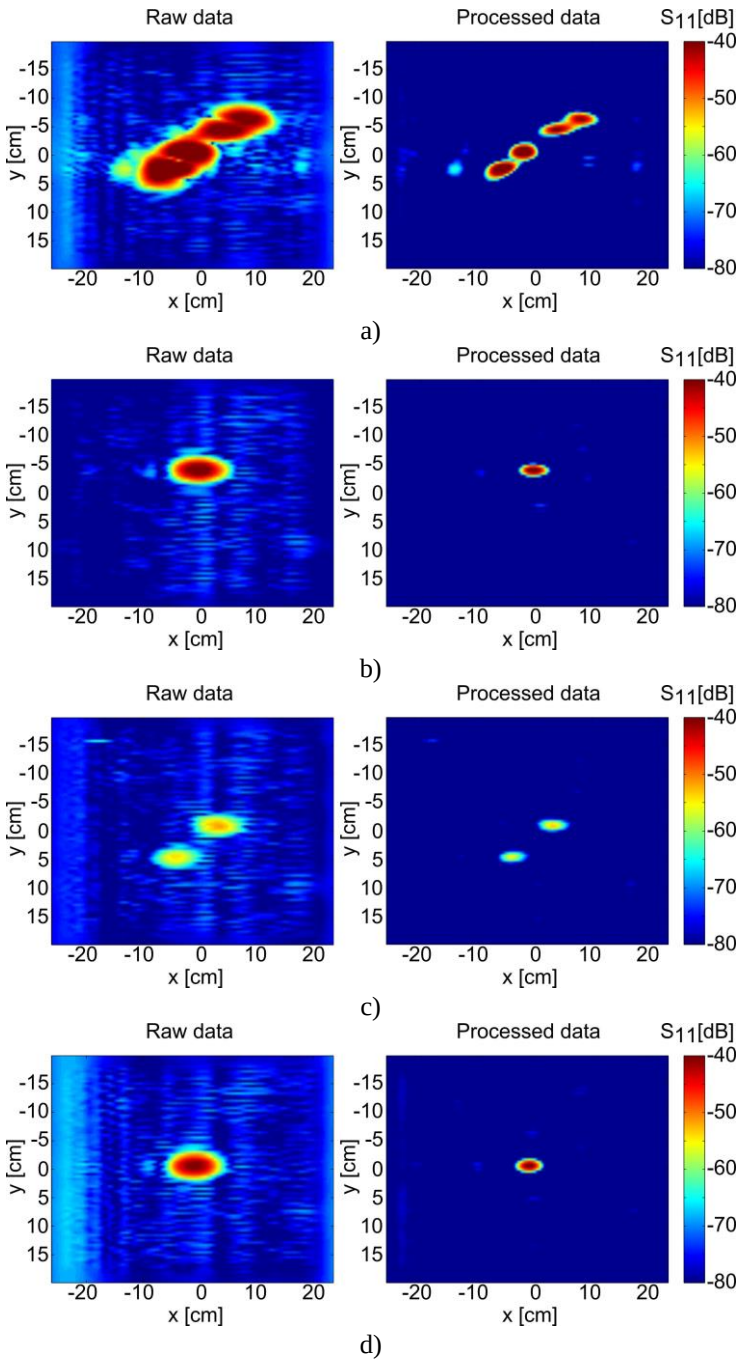

Figure 4.63 –Measured and processed S_{11} after the substraction of the value without object. Results are reported for: a) aluminium foil stick; b) piece of glass; c) aluminium foil balls; d) M4 nut.

4.4 Conclusions

The results presented in this chapter show the feasibility of an affordable scanning array imaging for conveyor belt setups working at 79 GHz. The system comprises a frequency scanning array with optimized field distribution at the aperture to reduce the side lobe level, an inexpensive reflector and a real-time postprocessing technique providing capabilities to detect very small objects (<3mm) on-the-fly.

The system has been validated by means of several targets including 2mm diameter metallic balls, and 0.5 mm side glass fragments with good image quality in all the cases giving an example of the potential industrial applications.

4.5 References

[Gru06] S. Gruszczynski, K. Wincza and K. Sachse, *"Reduced Sidelobe Four-Beam N-Element Antenna Arrays Fed by 4 x N Butler Matrices"*, IEEE Antennas and Wireless Propagation Letters, Vol. 5, pp. 430-434, 2006.

[Hfs15] (2015) Ansys HFSS 16.2 [Online]. Available: http://www.ansys.com/es_es/Productos/Flagship+Technology/ANSYS+HFSS

[Fan14] H. Fang, L. Yan, *"Parametric blind deconvolution for passive millimetre wave images with framelet regularization"*, International Journal for Light and Electron Optics, vol. 125, no. 3, pp. 1454-1460, Feb. 2014.

[Jai14] G. Jain, R. Kumar and Dr. J. Ghosh, "*Design of low sidelobe Microstrip antenna array"*, IOSR Journal of Electronics and Communication Engineering, Vol. 9, Issue3, pp. 57-60, 2014.

[Lar14] B. Larumbe-Gonzalo, A. Ibáñez-Loinaz, R. Gonzalo and J. Teniente, *"mm-Wave Imaging Results Based on a Frequency Scanning Delay Line Waveguide Horn Antenna Array"*, Microwave and Optical Technology Letters, vol.56, no. 12, Dec. 2014.

[Luc74] L. B. Lucy, *"An iterative technique for the rectification of observed distributions"*, Astronomical Journal, vol. 79, no. 6, pp. 745–754, 1974.

[Pas10] M. Pastorino, Ed., *Microwave imaging*. Hoboken, New Jersey (USA): John Wiley & Sons, 2010.

[Ric72]W. H. Richardson, *"Bayesian-based iterative method of image restoration"*, Journal of the Optical Society of America, vol. 62, no. 1, pp. 55–59, 1972.

[Spi12] L. Spinoulas, B. Amizic, M. Vega, R. Molina and A. K. Katsaggelos, *"Simultaneous Bayesian compressive sensing and blind deconvolution"*, In Proc. 20th European Signal Processing Conference (EUSIPCO), Bucharest, Hungary, pp. 1414-1418, 2012.

[Tic08] Grasp 9.8. Ticra [Online]. Available: http://www.ticra.com

[Zhe09] X. Zheng, J.-Y. Yang,-c. Li, *"Maximum likelihood frequency domain correction super-resolution algorithm for passive millimetre wave imaging"*, Acta Autom. Sin. Vol. 35, pp. 28-33, 2009.

[Zul13] F.Y. Zulkifli, T. Hidayat, Basari and E. T. Rahardjo, *"Sidelobe Level Suppression Using Unequal Four-Way Power Divider for Proximity Coupled Microstrip Antenna"*, in Proc. Asia-Pacific Microwave Conference Proceedings, 2013.

CHAPTER 5

DRIE FSA ARRAY AT WR2.2 BAND, DESIGN AND FABRICATION CONSIDERATIONS

5.1 Introduction

In the previous chapters, two different FSA imaging acquisition system prototypes have been presented, one of them working at the 79 GHz band and integrated in a conveyor belt lab setup. This frequency band was chosen because it is also the band proposed for

the next generation of automotive long range and high resolution radars, with recently available low-cost, of the shelf commercial components. This is one of the key elements that will make feasible the creation of a true low-cost complete FSA imaging system. However, from the frequency and resolution point of view, there could be certain applications where 79 GHz could be not enough, requiring an imaging system working at higher frequencies.

At the time this work was done, the RF measurement capabilities of the available equipment in the Antenna Group of the Public University of Navarra went up to 500 GHz using VDI WR2.2 frequency extension headers and a PNA-X N5242A Agilent network analyzer. For this reason, it was decided to design a high frequency proof-of-concept FSA array, with a central frequency of 440 GHz, with the objective of analyzing the feasibility of the concept at those high frequencies.

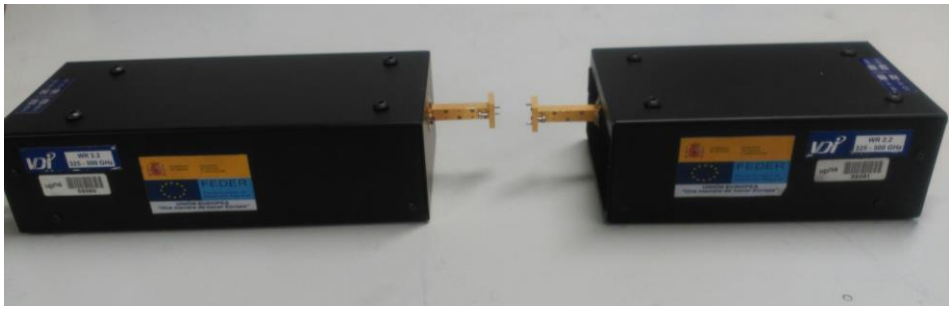

Figure 5.1 – VDI WR2.2 frequency extender headers.

At these frequencies, the required accuracies of the fabrication process are much higher than when working in the W-band, and although traditional milling techniques can still be used with very high precision milling machines like in [Bru08], very specialized equipment is required, and the resulting process has low repeatability, making the fabrication costs very high. However, there

is a very interesting alternative for fabrication at these frequency ranges, which is silicon micromachining by Deep Reactive Ion Etching or DRIE process. Since the Antenna Group has DRIE fabrication equipment available, and the DRIE process can lead to low cost fabrication at industrial levels, this would be the ideal technology to fabricate the designed high-frequency FSA array.

Figure 5.2 – Oxford Instruments DRIE equipment available.

5.2 DRIE FSA Array at WR2.2.

5.2.1 High Frequency Design Considerations and DRIE Process

As explained in the introduction of this chapter, working at higher frequencies requires higher fabrication accuracies, due to the smaller size of the geometrical features of the designs. For example, moving from 79 GHz to 440 GHz as the central frequency implies a size reduction factor of 5.57, so the tolerances have to be less than a fifth of the previous ones.

When using traditional milling fabrication, this size reduction has implications in the process that go far beyond the use of much more expensive and specialized equipment. For example, thigh environmental control is a must, since the tolerances are smaller than the deviations caused by thermal expansion of the components because of temperature changes in a non-controlled environment. Tool wear turns into a very important issue too, and the repeatability of the process lowers significantly. In practice, this means that the cost of fabricating a single unit increases, the rejection rate of the process increases too, and mass production of a single design doesn't cut the costs in the same degree as in the case where lower tolerances and accuracies are required.

An alternative to traditional milling could be metallic additive fabrication or 3D printing as it is widely known. Unfortunately, direct printing in metal doesn't have the required accuracy nor a good enough surface finishing to be a feasible technique at high frequencies. Nevertheless, it is possible that in a few years this additive manufacturing technology reaches an accuracy level high

enough for this kind of applications, turning into a real alternative to traditional milling or turning fabrication.

In recent years, an alternative fabrication technology is being used for high frequency components with very small geometrical features. This technology consists in silicon micromachining by a process known as Deep Reactive Ion Etching or DRIE. This process is a highly anisotropic etching process, capable of generating very deep and high aspect ratio features in silicon, and is specially well suited for the fabrication of rectangular waveguides and other passive waveguide components such as filters, and waveguides [Lea13, Lei14 and Rec14]. Once the silicon has been micromachined, metallization by sputtering or other chemical processes is done to provide the required electrical conductivity to the surfaces.

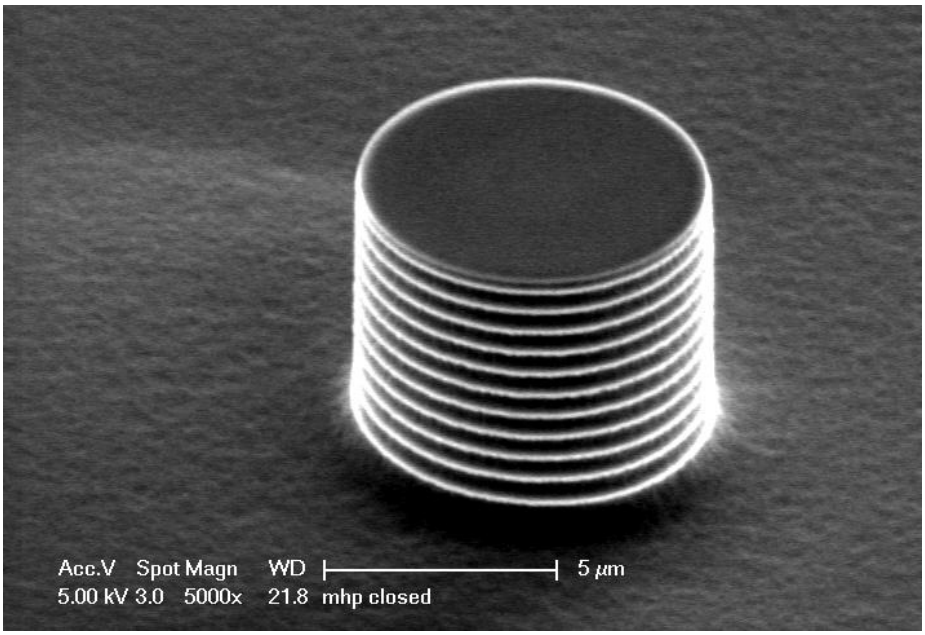

Figure 5.3 – Silicon micro pillar fabricated by a DRIE process

The process uses a combination of an isotropic ion plasma etching, alternated with some kind of passivation of the vertical

surfaces. The passivation can be achieved through two different processes, cryogenic process and Bosch process.

The cryogenic process works at a temperature of 163 K, slowing down the chemical reaction of the isotropic etching. However, since the horizontal surfaces are still exposed to the ion bombardment, vertical etching is achieved. The main drawback of this technique is the cracking of the wafers or the masks that can happen under the extremely low temperatures involved.

The Bosch process alternates the isotropic etching with isotropic deposition of a chemical passivation layer. This passivation layer protects the vertical surfaces, and is eliminated from the horizontal surfaces by the ion bombardment, leaving them unprotected from the etching. The alternation of these two processes generates vertical etching with small scallops, whose number and size depend on the number and duration of the alternating phases of the process. Smoother sidewalls can be achieved increasing the number of phases and decreasing their duration, but decreasing the vertical etching speed.

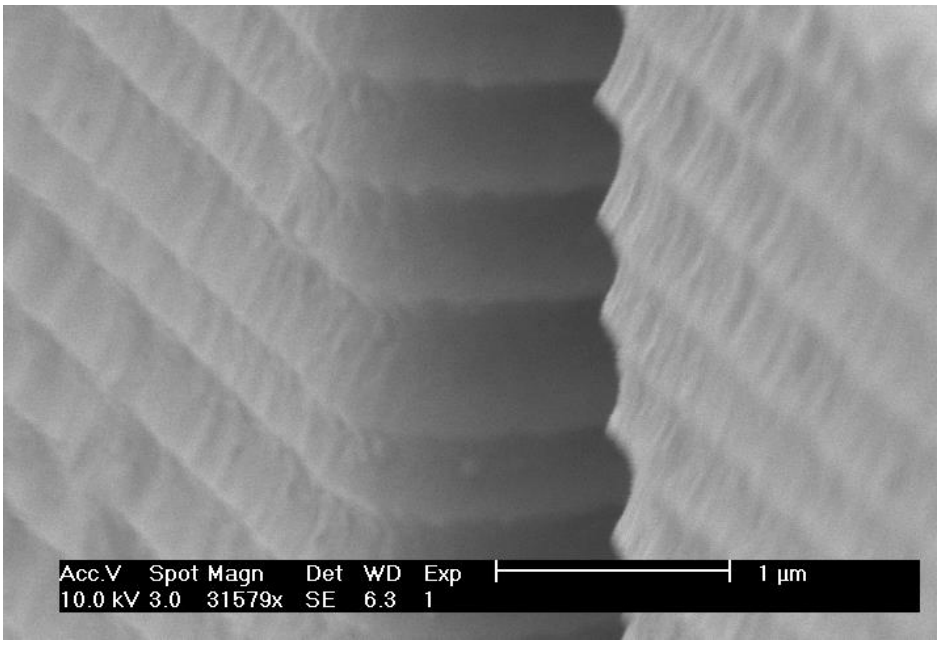

Figure 5.4 – Detail of the scallops in vertical wall etched with the Bosch process

A traditional photolithographic process can be used to control which areas of the silicon wafer are etched, with a very high degree of accuracy that basically depends on the optical resolution of the mask and transfer process. Additionally, playing with the mask materials their thicknesses or even better, their chemical orthogonality, , etchings of several depths can be achieved in different areas of the same silicon wafer, allowing the fabrication of complex multi-height structures.

All the described steps, including the final metallization process, are basically performed on a wafer level, and with a high degree of repeatability. Thus, it is expected that series fabrication at an industrial level could be done at a much lower cost than with traditional machining techniques.

5.2.2 440 GHz WR2.2 Feeding Network Design

Taking into account the good results that were obtained in the second version of the FSA array antenna prototype, working in W-Band, it was decided that the high frequency version would share the same enhancements. Similar uneven power splitters, that apply amplitude windowing to the output ports power, were used after scaling and re-optimizing them at 440 GHz with WR2.2 waveguide, with the goal of having low sidelobes. In this case, the small geometrical features of the components are not an issue, thanks to the high accuracy of the photolithography process used for the DRIE fabrication.

As it can be seen in the following figure, the design is very similar since to the W-Band FSA prototype. Scaling of the structure from WR10 to WR2.2 was done, and the path lengths were adjusted to the chosen 440 GHz central frequency, with an operating band of 20 GHz.

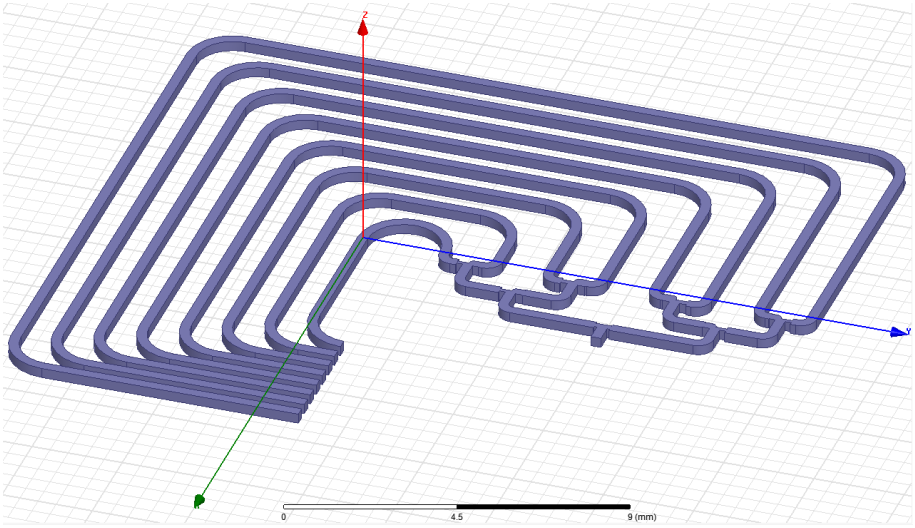

Figure 5.5 – HFSS model of the proposed feeding network working from 430 GHz to 450 GHz.

Different problems arise when dealing with the output antenna array that connects to the feeding network output ports at these frequencies. One of the main difficulties is achieving a good enough alignment between the feeding network output ports, and the input ports of the antenna array. In this case, the available mechanisms like alignment pins are the same as in the W-Band case, but the required accuracy is 5 times higher. On the other hand, fabricating the antenna array itself at high frequencies can be complicated without using expensive fabrication techniques like electroforming. Because of this, and for the purposes of this proof of concept, it was decided to use the output ports of the feeding network as open ended waveguide horn antennas, taking into account that this will limit the performance of the structure, especially in terms of return loss.

The HFSS simulation results of the structure are shown in the following figures. These simulations have been done with the output ports of the feeding network radiating as open-ended waveguides in an air filled radiation box.

It can be clearly seen that the return loss results are not very good over the entire working band. Especially in the lower half of the band, from 430 to 440 GHz, values of up to 6 dB of return loss are reached. This is due to the reflections produced at the output ports of the feeding network, which are open-ended waveguides, acting as antennas.

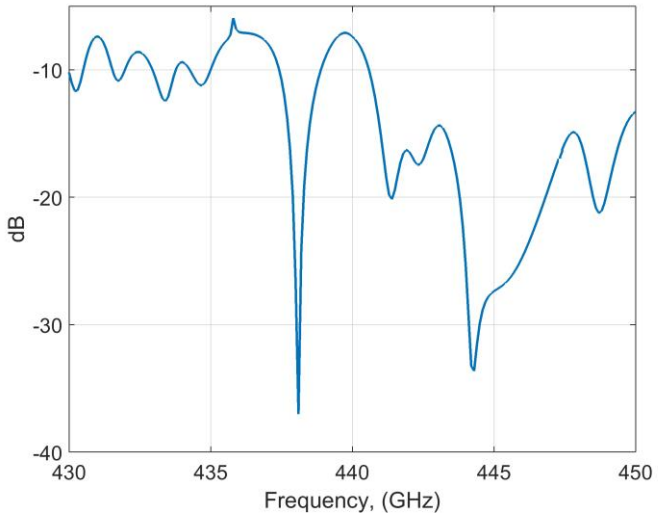

Figure 5.6 – S_{11} HFSS simulation results.

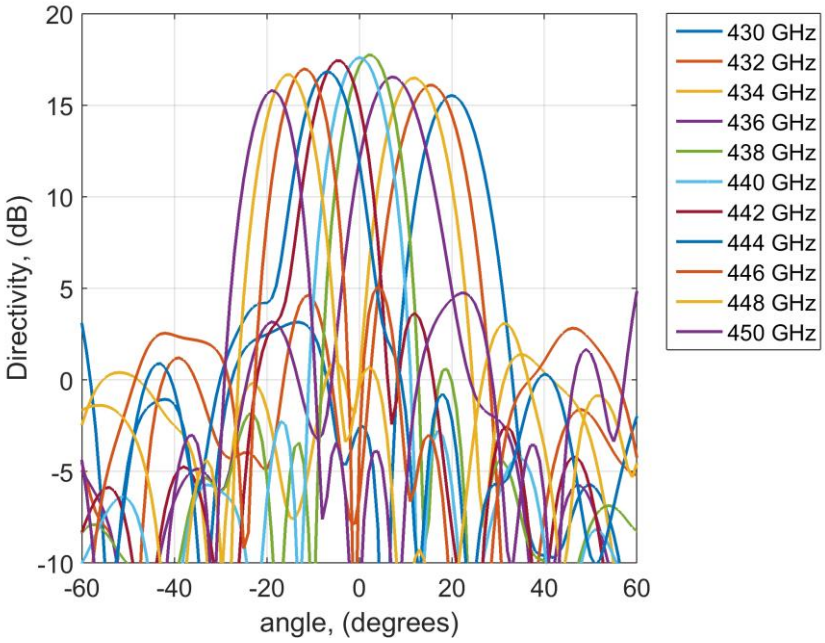

Figure 5.7 – Simulated radiation patterns of the prototype at several frequencies

The simulated radiation patterns show that the feeding network is working as expected, and frequency scanning can be observed. Almost 40 degrees of full scanning are obtained over the 20 GHz of bandwidth, with sidelobe levels of less than -15 dB compared to the maximum, at the worst case frequencies on the band extremes.

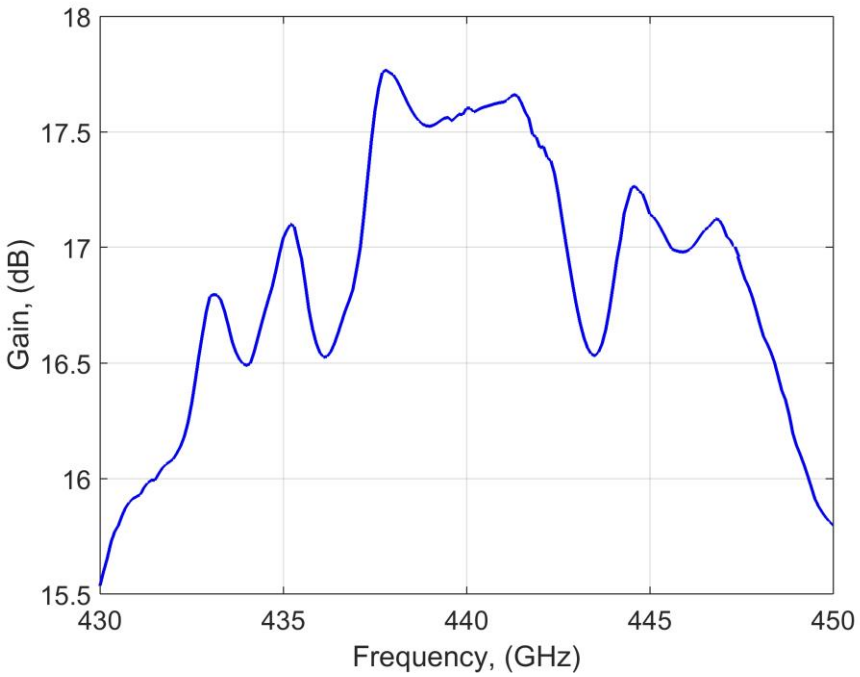

Figure 5.8 – Simulated gain results with HFSS.

The simulated gain is less stable with the frequency than in the other prototypes, probably due to resonances in the feeding network structure, caused by the reflections at the open-ended waveguides.

Regarding the DRIE fabrication, at the time of writing this dissertation, the multiple mask photolithography and multiple depth etching processes, and the gold metallization of the resulting components, are still being experimented with at the Antenna Group of Public University of Navarra, although some interesting results

have been already achieved. We hope that in the following months it will be possible to fabricate and measure the proposed design.

5.2.3 3D Printed encapsulation

The above proposed feeding network was designed to be fabricated in two halves, in a similar way to the other presented FSA array prototypes. To do that, two symmetrical layouts were printed on the photolithographic mask shown on the following figure.

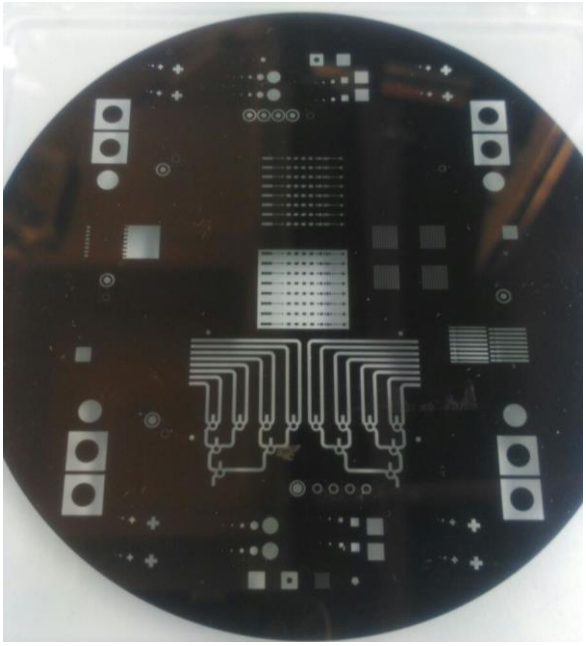

Figure 5.9 – Photolithographic mask containing the two symmetrical halves of the feeding network.

Once the circuit is fabricated in the silicon wafer, and after the cut and metallization processes, the fragile silicon pieces will have to be aligned, and fixed to an encapsulating casing that will give robustness and will provide a standard waveguide flange to the assembly. This casing can be fabricated using traditional machining or, having in mind again the low-cost goal, using 3D printing. In this

case, the dimensional tolerances are much lower than in the case of the assembly components that were fabricated for the conveyor belt prototype, so high precision photolithographic 3D printing on resin (SLA) has to be used, instead of the most widespread fused filament 3D printing technology that was used in the other components.

Two versions of the casing were designed, the first one with two symmetrical pieces to be fully fabricated by 3D printing or traditional machining. In the case of 3D printing, the resulting case should be metallized to provide electrical conductivity, at least in the flange area.

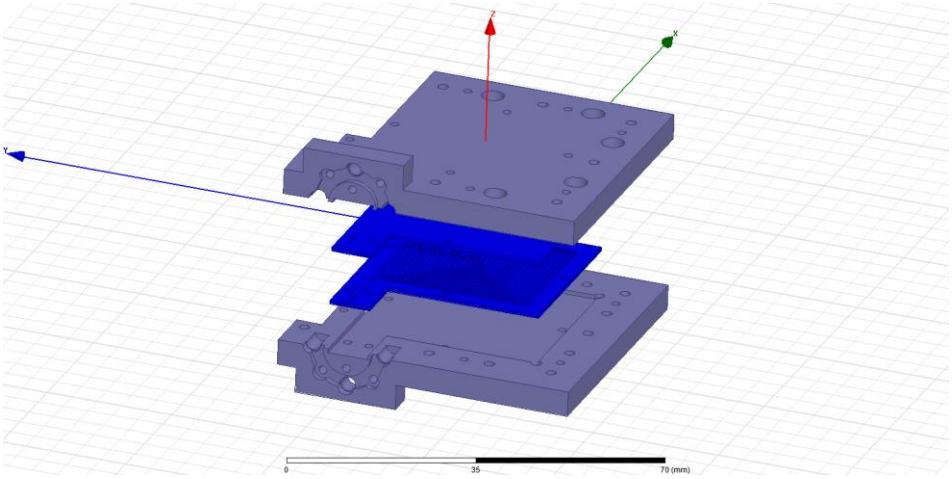

Figure 5.10 – 3D breakdown of the two silicon circuits with the top and botton halves of the casing.

The other version separates each casing half in two pieces, one to be fabricated in 3D printing, which only provides mechanical support and robustness, and the other corresponding to the waveguide flange, to be fabricated in metal by conventional machining. This version could be used in case 3D printing and metallization of the full structure doesn't work as expected.

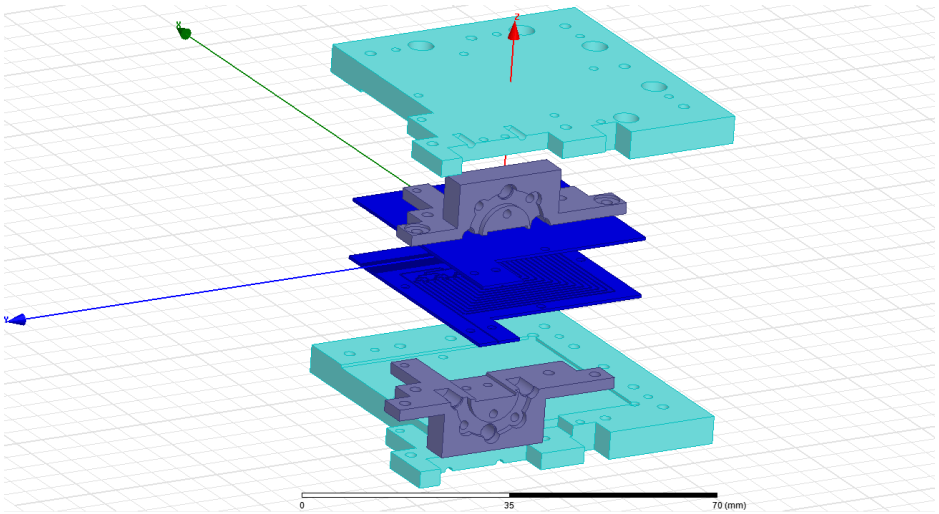

Figure 5.11 – 3D breakdown of the two silicon circuits with the top and bottom halves of the casing and separate flange pieces.

The first version of the casing was fabricated using the mentioned photolithographic 3D printing on resin process, with the resulting pieces shown in the following figure.

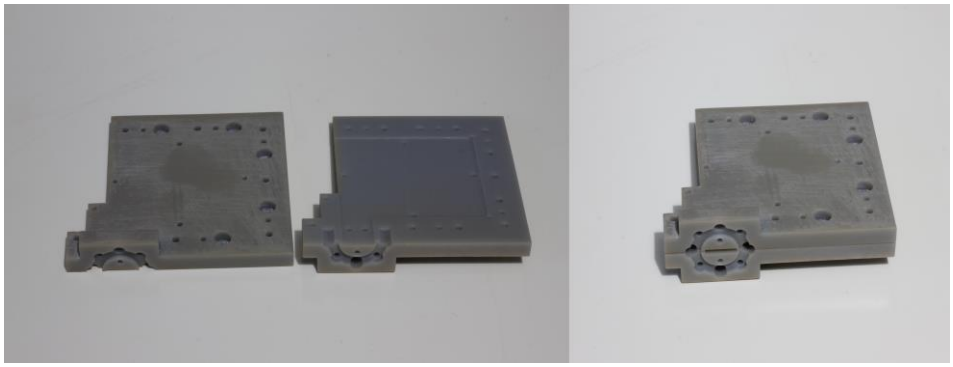

Figure 5.12 – 3D printed casing components and assembly result.

The casing pieces have very good aspect, and the results of the dimensional measurements are within the required tolerances. Only the metallization process remains for the casing to be fully ready to house the silicon circuits, as soon as they are fabricated.

5.3 References

[Bru08] P. J. Bruneau, H. D. Janzen and J.S. Ward, "*Machining of Terahertz Split-Block Waveguides with Micrometer Precision*", 33rd International Conference on Infrared, Millimeter and Terahertz Waves, 2008. IRMMW-THz 2008.

[Lea13] C. A. Leal-Sevillano, T. J. Reck, C. Jung-Kubiak, G. Chattopadhyay, J. A. Ruiz-Cruz, J. R. Montejo-Garai and J. M. Rebollar," *Silicon Micromachined Canonical E-Plane and H-Plane Bandpass Filters at the Terahertz Band*", IEEE Microwave and Wireless Components Letters, Vol. 23, No. 6, JUNE 2013.

[Lei14] D. Lei, S. Liu, Y. Zhang, J. Hu, L. Li, W. Zhao and R. Xu, "*A Micromachined 805 GHz Rectangular Waveguide Filter on silicon wafers*", IEEE International Conference on Communication Problem-Solving (ICCP), December 2014.

[Rec14] T. Reck, C. Jung-Kubiak, C. Leal-Sevillano and G. Chattopadhyay, "*Silicon Micromachined Waveguide Components at 0.75 to 1.1 THz*", 39th International Conference on Infrared, Millimeter and Terahertz waves (IRMMW-THz), September 2014.

CHAPTER 6

CONCLUSIONS AND GUIDELINES FOR FUTURE RESEARCH

6.1 Conclusions

In the previous chapters of this dissertation, several frequency scanning antenna arrays have been presented. Those prototypes were designed with the objective of obtaining a low cost THz imaging system, capable of scanning in one dimension by electronic means. Two of the designs have been fabricated and characterised as a proof of concept and one of them, combined with a customized mirror focusing system, has been integrated in a conveyor belt simulator. Real-time imaging with a single THz emitter/detector has been achieved with this prototype.

First of all, several approaches have been explored, in order to determine the optimal approach to the problem at hand. Leaky Wave Antenna technologies and Phased Arrays are the main two solutions that have been analyzed. The drawbacks of Leaky Wave Antennas for this particular application are the wide scanning angle required, the high losses at high frequencies, the difficulty to achieve a design with nice VSWR over a wide bandwidth, and the difficulty of properly control the amount of scanning angle for a certain bandwidth. On the other hand, phased arrays require active components like phase shifters that are expensive or even unfeasible at the desired frequency bands. Finally, a combination of the two technologies has been selected. It has been decided to use an array antenna, with a feeding network component devised to generate the required phases at its output ports, with the goal of producing a radiation pattern that can change its direction with the frequency of the input signal.

As a first proof of concept of the idea of using incremental length sections of waveguide to produce the required frequency dependent phase shift at the output ports of the feeding network, a FSA array has been designed in the 90-110 GHz frequency band. Several techniques to reduce the size of the feeding network have been tested, like waveguide stepped sections and hybrid rings. The simulated performance is good, and a prototype has been fabricated and measured, showing good agreement with the simulations, and proving the feasibility of the FSA approach. The radiation properties of the antenna are nice, with symmetrical beams, return losses below 10 dB, and less than 2 dB of scan losses. A first iteration of a focusing system has been made using a commercial TV satellite paraboloid reflector, and first imaging results have been obtained combining the system with a 1D positioner and several targets.

Despite the good results, several aspects with room for improvement have been detected, like the sidelobe level of the antenna, and the spatial resolution of the focusing system.

A second iteration of FSA array has been designed, changing the operating band to 79 GHz, with the idea of being able to use commercially available automotive radar components in the future, to create a cheap emitter/receiver for the imaging system. Windowing techniques have been applied to enhance the radiation properties of the antenna, like reducing the sidelobe level with the objective of obtaining better imaging results. Noticeable sidelobe level reduction has been obtained, proving that the windowing techniques chosen can be very useful for these kind of applications. A new mirror focusing system has been designed, based on the modification of a commercially available low-cost paraboloid mirror, and integrated into a conveyor belt simulator, creating a prototype capable of acquiring real-time imaging of a production line with a single RF sensor. The results obtained are good, with detection capabilities of objects of less than 3 millimeters with raw data without post processing.

Real-time post processing techniques have been applied, trying to deconvolute the radiation pattern of the antenna, with the goal to increase the resolution. For that, the near field beam at the target plane has been measured, with the results being incorporated into the post processing algorithm. The algorithm has been implemented for real-time operation, and included into the real-time image acquisition software, enhancing the resolution of the system, and extending the detection capabilities to objects of 0.5 millimeters of size.

Additionally, another FSA array working at the 440 GHz band has been designed and simulated, as a proof of concept for the FSA technology to be applied at higher frequencies. The design has been simulated, obtaining good results, and the possibilities of fabrication of the design have been analyzed, choosing to fabricate it by DRIE silicon micromachining. The feasibility of fabricating this by DRIE has been studied, and the photolithographic masks, as well as a 3D printed casing are ready for the fabrication of the system, as soon as the Antenna Group DRIE facilities can handle it. If this FSA array proof of concept working at high frequency works as expected when fabricated, it could open a lot of new possibilities in terms of applications that require higher resolutions or more compact systems, not achievable at lower frequencies.

Finally, the main conclusion that can be extracted from all the results of this work, is that FSA antennas are a valid approach to fulfill the requirements of electronic 1D scanning in real-time, and can be a very interesting alternative to develop the low-cost imaging systems that the industry is demanding for a multitude of applications in multiple fields.

6.2 Guidelines for future research

No research or scientific work is ever completed nor finished. It is woven in the very nature of science and technology to always have room for improvement, innovation, and new learning.

During the realization of the presented work, several tasks were identified, that could be the natural continuation of it. Future research works could deepen in these tasks in order to keep advancing in the direction of being able of providing cheap and reliable THz imaging systems for widespread industrial applications

like food safety. These are the identified ideas that could be further explored:

- Finish the DRIE prototype fabrication: The high frequency proof-of-concept prototype that was presented in the previous chapter, has not been fabricated yet because the DRIE fabrication facilities of the Antenna Group are not yet fully ready to handle the complete multilayer fabrication and metallization processes. Silicon DRIE fabrication of RF components is a field of study by itself, and good progress is being made in this aspect by the Group. As soon as the process is ready, the prototype can be fabricated and tested, and based on the results, improved versions can be developed, focusing in concrete applications that require higher frequency or resolution.
- Test the prototype in a real environment: The next step for determining if the approach is valid for real applications would be to test it in a relevant real environment. Imaging tests with real targets will give a lot of information and indicate which aspects of the system have to be further improved, like resolution, post-processing algorithms, acquisition speed, etc. Also, environmental factors that could impact the performance of the system, will be detected in the field.
- Develop a low-cost RF sensor: During the realization of this work, a network analyzer has been used as the transmitter and receiver RF sensor, when testing the different FSA antenna prototypes that have been developed. However, in a low-cost commercial system, using a VNA is not possible, and cheaper and more compact alternatives should be developed. One of the envisioned approaches could be the use of automotive

radar commercial components, available in W-band, to create the RF sensor. Also, since the FSA translates the spatial scanning into the frequency domain, the RF sensor must be capable of separate the different frequency channels that correspond to the different angles of radiation of the antenna. For doing that, several options should be analyzed and explored. For example, the following figures show the block diagrams of two different active systems that could be developed. The first one would be more simple, based on a tunable OL that would sweep the band of interest, detecting the received power in the different directions/frequencies, The second would be more complex, and would use a filter bank to detect the received power in all the directions/frequencies, simultaneously, noticeably reducing the acquisition time, something that can be critical in certain applications. All these factors and their implications in the resulting system, combined with the requirements of the intended applications will have to be further analyzed.

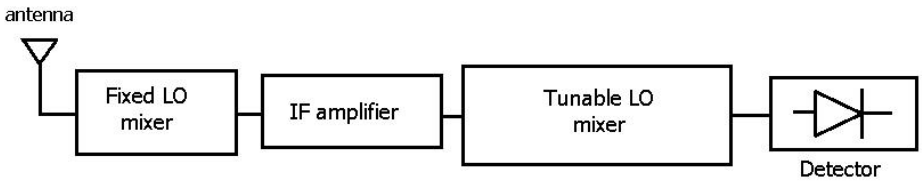

Figure 6.1 – Active imaging system with tunable OL.

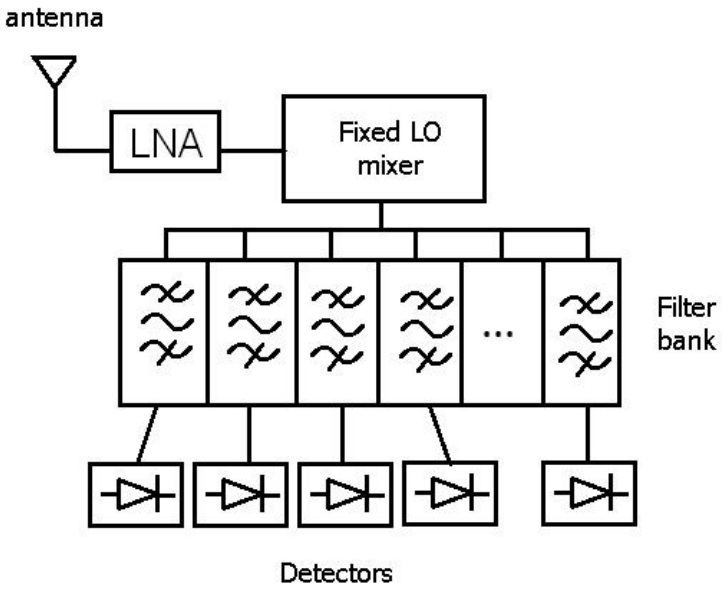

Figure 6.2 – Active imaging system with fixed LO and filter bank.

- Explore alternative illumination configurations: The two prototypes that have been tested during the realization of this work, have been based on a monostatic active configuration, and taking imaging of the power reflected by the targets. A single transmitter and receiver component was connected to the FSA antennas, emitting the RF signal, and receiving the power reflected by the targets in the image plane. However, alternative configurations could be tested, depending on the application requirements and the nature of the targets. For example, bistatic configurations could be considered, illuminating the targets more uniformly using a separate antenna and transmitter component, and receiving the reflected power with the FSA antenna connected to the receiver component. Also, transmissions setups like the one shown in the next figure, in which the antenna receives the power

transmitted through the target instead of the reflected one, should be analyzed and tested.

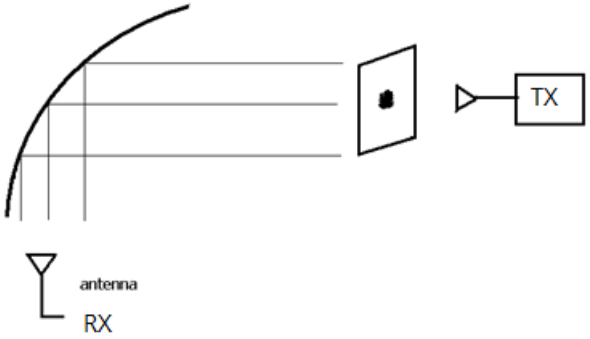

Figure 6.3 – Transmission imaging setup.

CHAPTER 7

LIST OF PUBLICATIONS

7.1 Journal Papers

1. **B. Larumbe**, J. Laviada, A. Ibáñez, J. Teniente, "Real-Time Imaging with Frequency Scanning Array Antenna for Industrial Inspection at W band", IEEE Transactions on Antennas and Propagation, Under Review, initial manuscript sent on October 2015.
2. J. Teniente, A. Martínez, **B. Larumbe**, A. Ibáñez, R. Gonzalo, "Design Guidelines of Horn Antennas That Combine Horizontal and Vertical Corrugations for Satellite Communications", IEEE Transactions on Antennas and Propagation, Vol. 63, No.4, April 2015.

3. **B. Larumbe-Gonzalo**, A. Ibáñez-Loinaz, R. Gonzalo, J. Teniente, "mm-Wave Imaging Results Based On A Frequency Scanning Delay Line Waveguide Horn Antenna Array", Microwave and Optical Technology Letters, Vol. 56, No. 12, December 2014.

7.2 International Conferences

1. J. Teniente, D. Valcázar, **B. Larumbe**, A. Martínez, A. Ibáñez and R. Gonzalo, "Feed Horn Antennas for Data Downlink and Uplink Spaceborne Communications", 10th European Conference on Antennas and Propagation (EuCAP), Davos, Switzerland, April 2016.
2. A. Rebollo, **B. Larumbe**, R. Gonzalo, I. Ederra, "Full W-Band Microstrip-to-Waveguide Inline Transition", 8th European Conference on Antennas and Propagation (EuCAP), The Hague, The Netherlands, April 2014.
3. **B. Larumbe-Gonzalo**, A. Ibáñez-Loinaz, A. Rebollo, R. Gonzalo, J. Teniente, "Image Acquisition at W-band Using a Frequency Scanning Antenna Array", 7th European Conference on Antennas and Propagation (EuCAP), Goteborg, Sweden, April 2013.
4. A. Rebollo, I. Maestrojuan, **B. Larumbe**, R. Gonzalo, I. Ederra, "Parametric Study of Pin Surface Used to Suppress Undesired Modes in a Packaged W-band Microstrip Receiver", 7th European Conference on Antennas and Propagation (EuCAP), Goteborg, Sweden, April 2013.
5. **B. Larumbe**, A. Rebollo, J. Teniente, "Coherently Fed Frequency Scanning Phased Array Structure for Imaging Applications", 6th European Conference on Antennas and Propagation (EuCAP), Prague, Czech Republic, April 2012.

6. A. Rebollo, I. Maestrojuan, **B. Larumbe**, R. Gonzalo, I. Ederra, “Design and Characterization of W-band components in Planar Technology”, 6th European Conference on Antennas and Propagation (EuCAP), Prague, Czech Republic, April 2012.

7.3 National Conferences

1. J. Teniente, D. Valcázar, **B. Larumbe**, A. Martínez, A. Ibáñez, R. Gonzalo, “Data Downlink and Uplink Feed Horn Antennas for spaceborne Communications”, URSI, Pamplona, Spain, September 2015.
2. **B. Larumbe**, A. Rebollo, A. Ibáñez, R. Gonzalo, J. Teniente, “Frequency scanning imaging results on mm-waves with delay line waveguide antenna”, URSI, Valencia, Spain, September 2014.
3. **B. Larumbe**, A. Rebollo, J. Teniente, “Frequency Scanning Phased Array Structure for Imaging Applications”, URSI, Elche, Spain, September 2012.